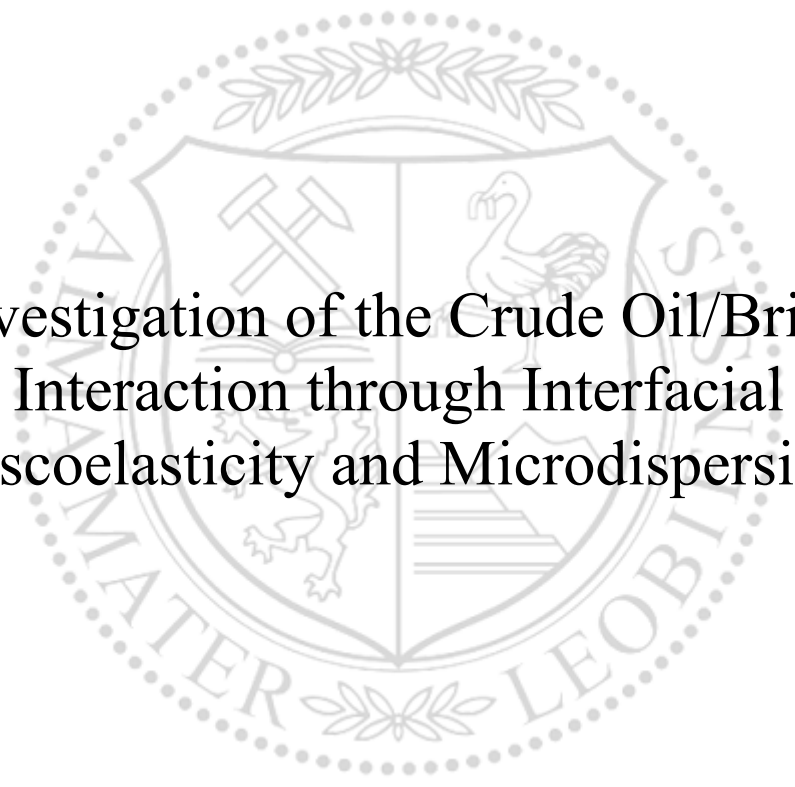




Chair of Reservoir Engineering

Master's Thesis



Investigation of the Crude Oil/Brine
Interaction through Interfacial
Viscoelasticity and Microdispersion

Peyman Nazifi

May 2021

Peyman Nazifi

Master Thesis 2021

Supervisor: Univ.-Prof. MSc. PhD Riyaz Kharrat

Investigation of the crude oil/brine interaction through interfacial viscoelasticity and microdispersion

Declaration

I hereby declare that except where specific reference is made to the work of others, the contents of this dissertation are original and have not been published elsewhere. This dissertation is the outcome of my own work using only cited literature.

Erklärung

Hiermit erkläre ich, dass der Inhalt dieser Dissertation, sofern nicht ausdrücklich auf die Arbeit Dritter Bezug genommen wird, ursprünglich ist und nicht an anderer Stelle veröffentlicht wurde. Diese Dissertation ist das Ergebnis meiner eigenen Arbeit mit nur zitierter Literatur.

P. Nazifi

Name, 27 May 2021

Abstract

Smart waterflooding in hydrocarbon reservoirs has been a topic of profound conjecture. Several recovery mechanisms have been proposed for the process, including wettability alteration toward water-wetness. On the other hand, less attention has been given to the fluid-fluid interactions. The long-held hypothesis that the Low Salinity Effect (LSE) depends mainly on rock and fluid interactions has led to occasional failures that fluid-fluid interactions can explain. Therefore, improving our knowledge about the microscopic interactions in the crude oil/brine/rock systems appears to be vital. In this study, the emphasis is on the two fluid/fluid mechanisms proposed recently, namely the interfacial viscoelasticity and microdispersion. Hence, interface viscoelasticity and formation of water in oil microdispersions are investigated experimentally and analytically. The impact of the aqueous phase ionic strength and ionic composition are examined on the viscoelastic properties of the crude oil/brine interfacial film by conducting interfacial dilatational rheological measurements under controlled water chemistry. Interfacial viscoelasticity measurements were conducted on three Austrian crude oils. In general, the viscoelastic properties of the interface have a reverse relationship with the brine salinity reduced no matter what type of ions are present in the brine. However, the rate of elasticity build-up depends upon specific ions present in the solution as well as crude oil properties. The interface viscoelasticity for NaCl solutions and crude oil increased continuously as the salt concentration decreased. However, it increased non-monotonically until a maximum in viscoelasticity was observed, at 10,000 ppm for a pure solution NaCl with 2.5% Na₂SO₄. The interfacial film response depends on the combined characteristics of crude oil and water and the aging time between two fluids. A good correlation was developed for the oil property, namely, the acidic component and the oil viscosity and interfacial mechanical moduli. This correlation might indicate that the adsorption of polar materials onto the interface can be considered a diffusion-like process. The analytical investigation of the available microdispersion data from the literature revealed the importance of crude oil acidic components as the main contributing factor in the formation of water in oil microdispersions. Furthermore, the total brine salinity was determined as the main factor regarding the brine properties with a negative correlation factor. Thus, the outcomes of the statistical investigation of the microdispersion ratio were in agreement with the observations done in the literature, whereby the oil acidic components were detected as the main crude oil fractions contributing to the microdispersion formation.

Zusammenfassung

Smartes Wasserfluten in Kohlenwasserstofflagerstätten ist aktuell Gegenstand intensiver Spekulationen. Mehrere Gewinnungsmechanismen für diesen Prozess sind bereits vorgeschlagen worden, einschließlich der Änderung der Benetzbarkeit in Richtung erhöhter Wasserbenetzbarkeit. Im Gegensatz dazu, steht die Rolle der Fluid-Fluid Interaktion noch im Hintergrund. Jene Hypothese, welche den Effekt der niedrigen Salinität (LSE) durch Gestein-Fluid Interaktionen beschreibt, hat sich lange gehalten, scheitert allerdings gelegentlich an Effekten, welche durch Fluid-Fluid basierende Interaktionen erklärt werden können. Daher ist ein tieferes Verständnis der mikroskopischen Interaktionen zwischen Rohöl, Wasser und Gestein von höchster Bedeutsamkeit. Diese Arbeit fokussiert sich auf die beiden Fluid-Fluid Mechanismen, welche erst kürzlich in der Branche publiziert wurden, nämlich die Viskoelastizität der Grenzflächen und die Mikrodispersion. Dabei wurden sowohl experimentell als auch analytisch beide Mechanismen im Rahmen dieser Arbeit abgedeckt. Die viskoelastischen Eigenschaften der Rohöl-Wasser Grenzfläche wurden mit rheologischen Messungen unter speziellen Bedingungen und drei verschiedenen Rohölen aus österreichischen Ölfeldern untersucht, um den Einfluss der Ionenstärke und Ionenkonzentration zu ermitteln. Allgemein gilt, dass die Viskoelastizität zunimmt mit abfallender Salinität des Wassers, unabhängig von den vorkommenden Ionen im Wasser. Die Rate des elastischen Wachstums und das Plateau jedoch, hängen von spezifischen Ionen in Lösung und im Rohöl ab. So nimmt die Viskoelastizität der Grenzfläche zwischen einer NaCl Lösung und Rohöl kontinuierlich zu, solange die Konzentration des Salzes abnimmt. Die nicht-monotone, kontinuierliche Zunahme findet allerdings nur bis zu einem maximalen Wert statt, welcher bei einer reinen Kochsalzlösung mit 2,5% Na_2SO_4 bei 10,000ppm liegt. Dieses Verhalten der Rohöl-Kochsalz Grenzfläche hängt von den Charakteristiken beider Fluide und der Verweilzeit derselbigen ab. Eine gute Korrelation konnte für die sauren Bestandteile des Rohöls, der Viskosität und des mechanischen Grenzflächen-Modules gefunden werden. Diese Korrelation könnte vorzeigen, wie die Adsorption polaren Materials an der Grenzfläche dem Prozess der Diffusion ähnelt. Saure Bestandteile des Rohöls weisen sich nach analytischer Untersuchung der verfügbaren Literatur über Mikrodispersion, als eine der Hauptantriebe für die Formung von Wasser-in-Öl Mikrodispersion aus. Im Bereich der Eigenschaften des Wassers, wird die Salinität als einer der Hauptfaktoren für Mikrodispersion betrachtet. Das Ergebnis der analytischen Arbeit der Mikrodispersion deckt sich daher mit den Beobachtungen der Literatur.

Table of Contents

Chapter 1.....	1
Introduction	1
1.1 Background and Context.....	2
1.2 Scope and Objectives.....	2
1.3 Achievements.....	2
1.4 Technical Issues.....	2
1.5 Overview of Dissertation	2
Chapter 2.....	3
State of the Art or Literature Review	3
Chapter 3.....	13
Theoretical explanation of the fluid/fluid mechanisms	13
3.1 Formation of water in oil microdispersions	13
3.2 Interfacial dilatational viscoelasticity	15
Chapter 4.....	27
Methodology.....	27
4.1 Statistical analysis of microdispersion data from the Literature.....	27
4.2 Experimental methodology.....	38
Chapter 5.....	49
Results and Discussion	49
5.1 Interfacial dilatational viscoelasticity	49
5.2 Microdispersion Ratio Modeling.....	64
Chapter 6.....	67
Conclusion.....	67
6.1 Summary.....	67
6.2 Future Work.....	68
Chapter 7.....	69
References	69
Appendix A.....	77
Microdispersion ratio data from the literature	77
Appendix B.....	85
The R code, written for the logistic modeling of the microdispersion ratio data.	85

List of Figures

Figure 1 – A magnified region of the micromodel which depicts the formation of dark spots (micro-dispersions) in the oil phase during low salinity water injection (Emadi & Sohrabi, 2013).	5
Figure 2 – A magnified image of the micromodel that depicts dark particles' formation (Emadi & Sohrabi, 2013).	5
Figure 3 – Two illustrations show the organization of indigenous surface-active materials of oil in; low salinity (right) and high salinity (left) (Mahzari et al., 2019).	6
Figure 4 – Saturation versus time plots. The blue line shows brine, black line oil, and the red line, the intermediate phase (micro-dispersion phase) (Bartels, et al., 2017).	7
Figure 5 – Different degrees of oil and water structure formation for different crude oils (Bartels et al., 2017).	7
Figure 6 – Different degrees of oil and water structure formation for different crude oils (Bartels et al., 2017).	8
Figure 7 – Microdispersion ratios of 30 different crude oils after contacting with high salinity (204 kppm) and low salinity (240 ppm) (Masalmeh et al., 2019).	9
Figure 8 – Fluid arrangement of oil ganglia as a result of coalescence between clusters (Rücker et al., 2015).	10
Figure 9 – The elasticity behavior of the interface based on different brine salinities with different sulfate concentrations (Barati et al., 2017).	11
Figure 10 – The schematic representation of the three environments (adsorbed film, monomer and, micelle or W/O micro-dispersions) in which surface-active components reside in the oil phase (Emadi et al. 2013).	14
Figure 11 – Schematic of the effect of microdispersion formation on oil swelling and possible detachment of crude oil from the rock surface (Fattahi Mehraban et al. 2020).	14
Figure 12 – Example of acquired surface tension (σ) and surface area (A) by the oscillating drop method (Ravera et al. 2010).	20
Figure 13 – The effects of ions on the electrostatic potential (ψ) as well as the Debye length (dashed line) at the oil/water (with variant salinity levels) interface (Chávez-Miyauchi et al. 2016).	21
Figure 14 – Top: CEF as a function of the salinity of brine for Na_2SO_4 aqueous solution. Bottom: Interface elasticity of the crude oil/brine interface versus aqueous phase salinity (Moradi et al. 2016).	22
Figure 15 – The schematic of the flow-focusing device for the snap-off experiment (Liu et al. 2019).	23
Figure 16 – The flow-focusing device for the snap-off experiment (Alvarado et al. 2014).	24
Figure 17 – The resulting oil droplet after snap-off (left) and after snap-off (right) for brines with different salinities (100% is equivalent to 95000 ppm Na_2SO_4 solution) (Alvarado et al. 2014).	24
Figure 18 – a) The effect of aging time on snap-off behavior. b) droplet area of the first five sequential droplets formed for various aging times (Morin, Yafei, & Alvarado, 2016).	25
Figure 19 – The papers and their contributions used for the statistical analysis.	28
Figure 20 – The boxplot of the data from each published paper, showing statistical fingerprints of each data set.	29
Figure 21 – The violin plot of the published data from each paper, including statistical characteristics of each data set.	29
Figure 22 – The boxplot of the reported temperature intervals of the reported data.	30
Figure 23 – The histogram and the boxplot of the microdispersion ratio data.	31
Figure 24 – The histogram and the boxplot of the asphaltene fractions.	31
Figure 25 – The histogram and the boxplot of the saturate fractions.	32
Figure 26 – The histogram and the boxplot of the aromatic fractions.	32

Figure 27 – The histogram and the boxplot of the resin fractions.	33
Figure 28 – The histogram and the boxplot of TAN.....	33
Figure 29 – The histogram and the boxplot of TBN.....	34
Figure 30 – The histogram and the boxplot of the CII index.....	34
Figure 31 – The histogram and the boxplot of the Asphaltene/Resin ratio.....	35
Figure 32 – The plot of the microdispersion ratio values Vs. Brine’s salinity in ppm.	36
Figure 33 – The example of a logistic model.....	37
Figure 34 – The example of having the illness vs. BMI with the cut value of 0.5, the red dots in the right plot: the predicted healthy, the blue dots in the right plot: the predicted sick.	38
Figure 35 – The Spinning Drop Device for the measurements of interfacial viscoelasticity (Arnold, 2018).....	40
Figure 36 – The capillary tube filled with the two immiscible fluids for viscoelasticity measurements (Arnold, 2018).....	40
Figure 37 – The signal of the interfacial tension and the surface area with a phase angle of 28.68 degrees for the experiment of crude oil 16th and distilled water.	42
Figure 38 – The example of the signal of the interfacial tension with the required parameters for calculating complex modulus for the experiment of crude oil 16th and distilled water.....	42
Figure 39 – The example of the signal of the surface area with the required parameters for calculating complex modulus for the experiment of crude oil 16th and distilled water.	43
Figure 40 – Complex Modulus vs. Time measured every 15 minutes for 3 hours for the experiment of crude oil 16th and distilled water.....	44
Figure 41 – Elastic Modulus vs. Time measured every 15 minutes for 3 hours for the experiment of crude oil 16th and distilled water.....	44
Figure 42 – Viscous Modulus vs. Time measured every 15 minutes for 3 hours for the experiment of crude oil 16th and distilled water.....	45
Figure 43 – Representation of the error bar of the measurements (Complex Modulus vs. Time measured every 15 minutes for 3 hours, for the experiment of crude oil 16th and distilled water).	45
Figure 44 – Representation of the error bar of the measurements (Elastic Modulus vs. Time measured every 15 minutes for 3 hours, for the experiment of crude oil 16th and distilled water).	46
Figure 45 – Representation of the error bar of the measurements (Viscous Modulus vs. Time measured every 15 minutes for 3 hours, for the experiment of crude oil 16th and distilled water).	46
Figure 46 – The representation of the micromodel chip and the chip holder (Schnöpf, 2019).	47
Figure 47 – Complex Modulus vs. Brine Salinity (ppm) for three crude oil samples and pure NaCl solutions.....	50
Figure 48 – Elastic Modulus vs. Brine Salinity (ppm) for three crude oil samples and pure NaCl solutions.	50
Figure 49 – Viscous Modulus vs. Brine Salinity (ppm) for three crude oil samples and pure NaCl solutions.....	51
Figure 50 – Complex Modulus vs. Brine salinity (ppm) for normal crude 16 th and de-asphalted crude 16 th with pure NaCl solutions.....	52
Figure 51 – Elastic Modulus vs. Brine salinity (ppm) for normal crude 16 th and de-asphalted crude 16 th with pure NaCl solutions.....	52
Figure 52 – Viscous Modulus vs. Brine salinity (ppm) for regular crude 16 th and de-asphalted crude 16 th with pure NaCl solutions.....	53
Figure 53 – Complex modulus vs. TAN/Viscosity for crude oil samples and distilled water.	54
Figure 54 – Elastic modulus vs. TAN/Viscosity for crude oil samples and distilled water.....	54
Figure 55 – Viscous modulus vs. TAN/Viscosity for crude oil samples and distilled water... ..	55
Figure 56 – Complex Modulus vs. Brine salinity (ppm) for crude 16 th and Flysch with pure NaCl and pure NaCl solution with 2.5% sodium sulfate solutions.....	55
Figure 57 – Elastic Modulus vs. Brine salinity (ppm) for crude 16 th and Flysch with pure NaCl and pure NaCl solution with 2.5% sodium sulfate solutions.	56

Figure 58 – Viscous Modulus vs. Brine salinity (ppm) for crude 16 th and Flysch with pure NaCl and pure NaCl solution with 2.5% sodium sulfate solutions.	56
Figure 59 – Complex, Elastic and Viscous moduli vs. Saturate content for crude oil and distilled water.....	57
Figure 60 – Complex, Elastic and Viscous moduli vs. Aromatic content for crude oil and distilled water.....	57
Figure 61 – Complex, Elastic and Viscous moduli vs. Resin content for crude oil and distilled water.....	57
Figure 62 – Complex, Elastic and Viscous moduli vs. Asphaltene content for crude oil and distilled water.....	58
Figure 63 – Complex, Elastic and Viscous moduli vs. CII for crude oil and distilled water... ..	58
Figure 64 – Complex, Elastic, and Viscous moduli vs. As/R ratio for crude oil and distilled water.....	58
Figure 65 – The imbibition experiment of a Gilderhauser sandstone (Rücker, et al., 2015)... ..	59
Figure 66 – The end state of the water flooding results: left: high injection rate, right: low injection rate.	61
Figure 67 – The location of different displacement regimes. The red and blue dots show the low and high rate experiments, respectively (Alzahid et al., 2017).....	62
Figure 68 – Cluster size distribution for crude oil. A): high and B): low flooding rates.	63
Figure 69 – The results of the prediction model Vs. Experimental data.....	65

List of Tables

Table 1 – The range of CII values for the collected data from the literature.	35
Table 2 – The range of As/R ratio values for the collected data from the literature.	36
Table 3 – The specification of the micromodel and its properties (Schnöpf, 2019)	47
Table 4 – Crude oil properties	49
Table 5 – Brine properties.....	49
Table 6 – The recovery results of the microfluidic experiments.	61
Table 7 – The coefficients of Equation 17.....	64
Table 8 – Data mismatch for low microdispersion ratio range (less than 4).	65
Table 9 – Data mismatch for high microdispersion ratio range (greater than 4).	65
Table 10 – Microdispersion ratio data from the literature	78

Nomenclature

m	mass	[kg]
r	radius	[m]
ν	frequency	[Hz]
D	diffusion coefficient	[m ² .s ⁻¹]
k_{β}	Boltzmann constant	[J.K ⁻¹]
T	absolute temperature	[K]
μ	viscosity	[Pa. s]
N_A	Avogadro number	
e	electro charge	[Coulomb, C]
I	ionic strength	[mol. Kg ⁻¹]
ϵ_r	dielectric constant	[F/m]
ϵ_0	Permittivity of free space	[F/m]
γ	interfacial tension	[N/m]

Abbreviations

LSE	Low Salinity Effect
TAN	Total Acid Number
LSWI	Low Salinity Water Injection
EOR	Enhanced Oil Recovery
CEC	Cation Exchange Capacity
PDI	Potential Determining Ions
CMC	Critical Micelle Concentration
NAs	Naphthenic Acids
SARA	Saturate, Aromatic, Resin, Asphaltene
IFT	Interfacial Tension
DFT	Discrete Fourier Transform
CEF	Critical Electric Field
ppm	Parts per Million
wt%	Weight Percent
TBN	Total Base Number
CII	Colloidal Instability Index
As/R	Asphaltene over Resin ratio
GOF	Goodness Of Fit
AIC	Akaike Information Criterion
BIC	Bayesian Information Criterion
MDR	Micro Dispersion Ratio
BMI	Body Mass Index
DCM	Dichloromethane
MPLC	Medium Pressure Liquid Chromatography
IFVE	Interfacial Viscoelasticity

Chapter 1

Introduction

Tuning the ionic content of water for water flooding can be beneficial for several reasons. Above all, due to lower cost and water availability, less investment is required for oil recovery than higher cost-demanding chemical and thermal methods. In general, tuning the ionic water content requires understanding the response mechanisms that include rock/fluid and fluid/fluid interactions. Wettability alteration of the system towards a more water-wet state is the main reason for the recovery gain. On the other hand, additional oil recovery is also reported from already water-wet systems and micro-fluidic experiments. This shows no general understanding of the underlying mechanisms responsible for the additional oil recovery due to smart water flooding. Although the rock and fluid interactions were investigated first by researchers, the effect of fluid/fluid interactions is overlooked. Tuning the ionic content of water can change the fluid/fluid properties considerably. Investigating the fluid/fluid interactions might answer the contradictory results in the literature and complete the gap in understanding underlying the mechanisms in the smart water processes.

Among the fluid/fluid interactions, the formation of water in oil micro-dispersions and the change in the viscoelastic properties of oil and brine interface are proposed recently in the literature. When oil comes in contact with brine with different salinities, generally, its water content increases. This water content increase depends on different parameters, such as oil, water, and thermodynamic properties.

The other recent purely fluid/fluid mechanism is the change in the oil and water interface's viscoelastic properties. The more elastic the interface is, the more it can resist deformations. These deformations are exerted by water on the oil droplets. Droplets with higher elasticity can withstand these applied forces. Therefore, stay intact; otherwise, they shrink in volume, leading to mobility reduction and oil trapping.

1.1 Background and Context

In this work, the focus is on the fluid/fluid interactions during smart water processes. Two fluid/fluid mechanisms are investigated: water formation in oil micro-dispersions and the interfacial dilatational viscoelasticity of oil and water. All available data from the literature is collected to model the increased water content of the oil as a result of contacting brines with different salinities.

With respect to the second mechanism, i.e., the interfacial dilatational viscoelasticity of the oil and water, experimental work is conducted to see the effect of lowering the ionic content of the brine and the addition of sulfate ions to the water.

1.2 Scope and Objectives

The study analyzes two fluid/fluid mechanisms during smart water processes: microdispersion ratio and elasticity. The main objectives are predicting microdispersion ratio probability based on the available data and investigating the interfacial dilatational viscoelasticity at the oil and water interface.

1.3 Achievements

The significance of the formation of water in oil microdispersions is modeled, and the derived model can predict the available data in the literature with reasonably fair accuracy. Also, an insight into the viscoelasticity of the oil/water interface based on the experimental measurement and its impact on the fluid redistribution inside porous media was obtained.

1.4 Technical Issues

The spinning drop device showed relatively high measurement errors for the dilatational interfacial viscoelasticity measurements. Since the measurements are based on image processing, higher quality images of the droplet with better accuracy can lead to more accurate measurements.

1.5 Overview of Dissertation

The first part of this work contains the modeling of water in oil micro-dispersions.

In the second part, the effect of lowering the ionic content of brine and the addition of sulfate ions on the dilatational elasticity coefficient of the oil and water interface is analyzed.

Chapter 2

State of the Art or Literature Review

Low salinity water injection (LSWI) has become the topic of research recently, being recognized as an economic Enhanced Oil Recovery (EOR) method (Morrow & Buckley, 2011). There is a consensus about using brine with low salinity for sandstone reservoirs, during which reducing salinity to less than 5000 ppm results in low salinity water effect (LSE) (Lager et al., 2008; McGuire et al. 2005; Nasralla et al. 2011). Contrarily, several studies show the negligible effect of LSWI in carbonate reservoirs, meaning this EOR method is only beneficial in sandstone reservoirs with high clay content (Fathi et al., 2010).

Early studies have investigated the role of clay minerals during LSWI, through which clay swelling and incremental pressure drop were reported as the primary mechanisms. Cation exchange capacity (CEC) was reported as the most important oil recovery factor by low salinity water. Clay minerals mainly manage the increase in recovery. The more the CEC, the more their impact will be. The highest CEC is reported to belong to Kaolinite, followed by Chlorite and Smectite. (Jackson et al. 2016; Austad et al. 2010).

Due to the role of Kaolinite on wettability, detailed pore-scale studies have been conducted, and the beneficial effect was reported for sandstone (Hassenkam, et al., 2012; Lebedeva & Fogden, 2011). It was stated that the addition of Kaolinite as the clay type in pure quartz sand packs significantly affects the recovery during LSWI (Lebedeva & Fogden, 2011). High coverage of the surface by clay (in this case, kaolinites) was suggested to affect the surface properties, such as influencing the crude oil-solid interactions toward less oil-wet or more water-wet state, depending on the adsorption mechanisms. The studies showed that not only the type of clay but also the polar components of crude oil and the presence of the ions in injection water as well as connate water would affect the performance of LSWI (Sanyal et al. 2017; Sanyal et al. 2019).

Nevertheless, the increase in recovery has been reported not only for rocks containing other clay minerals such as chlorite and muscovite. (Cissokho et al. 2010) but also for clay-free sandstone rocks (Pu et al. 2010; Lebedeva et al. 2009; Pu et al. 2008; Hassenkam et al. 2011).

Although these incremental oil recovery in sandstone rocks being owed to clay minerals, no possible implementation for the process was considered for carbonate reservoirs.

In 2010 Yousef et al. first reported additional oil recovery due to low salinity water injection in carbonates reservoirs (Yousef et al. 2010). This study was conducted when many researchers could not agree with applying low salinity water injection in carbonate rocks (Fathi et al., 2010; Zahid et al. 2012; Austad et al. 2012). They observed that seawater injection increased recovery and highlighted the impact of potential determining ions (PDIs) on changing the wettability of the system in favor of oil recovery (Strand et al., 2006; Zhang et al., 2007). Austad et al. (2011) tried to justify the observations in the experiments done by Yousef et al. in 2010 by highlighting the role of sulfate ions (Austad et al., 2011). They proposed that the dissolution of anhydrite was the reason for improved oil recovery observed by Yousef, leading to the in-situ generation of SO_4^{2-} ions. Contrary to previous studies, Zahid et al. (2012) reported additional oil recovery for carbonate rocks using diluted seawater injection without dolomite and anhydrite minerals.

All of the discrepancies regarding the main mechanism of LSWI led to a new mechanism, so-called electrical double layer expansion (Ligthelm, et al., 2009). Based on the double-layer expansion theory, reducing the ionic content of the displacing phase, i.e., water, induces more negative charges at the interfaces, resulting in wettability alteration (Mahani, et al., 2015).

Up until 2013, all the suggested mechanisms for LSWI were lacking consistency and were case-dependent. Some studies worked with specific rock and specific conditions such as initial wettability, pH, initial salinity. The effect of fluid-fluid interactions (crude oil and brine) during low salinity water injection in sandstone and carbonate reservoirs was underestimated until microdispersion formation was introduced as a possible mechanism for low salinity water injection (Emadi & Sohrabi, 2013).

These microdispersions have been observed as dark particles within the oil phase during microfluidic experiments when crude oil contacted brine with lower salinity (Emadi & Sohrabi, 2013). A magnified region of the micromodel given in Figure 1 and Figure 2 depicts the formation of dark spots (micro-dispersions) in the oil phase during low salinity water injection. The red arrows show locations where the segregation of dark particles is more apparent.

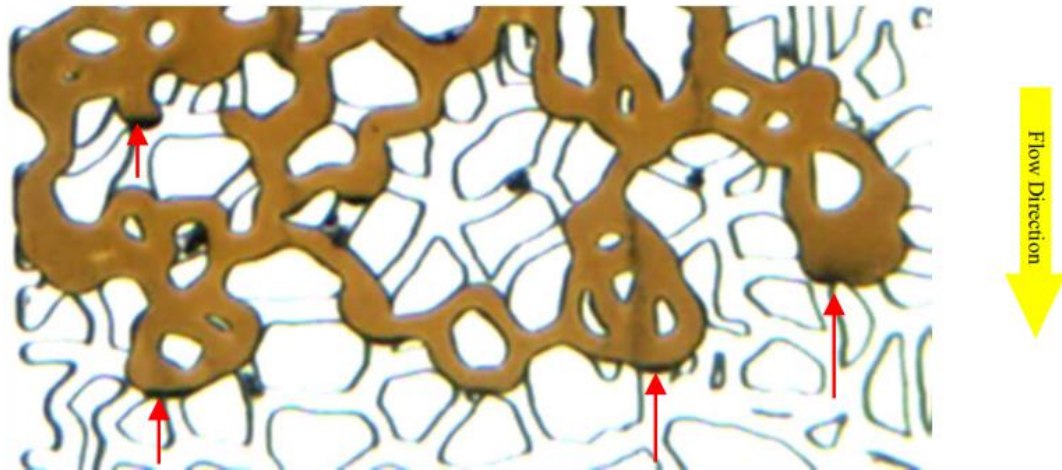


Figure 1 – A magnified region of the micromodel which depicts the formation of dark spots (microdispersions) in the oil phase during low salinity water injection (Emadi & Sohrabi, 2013).

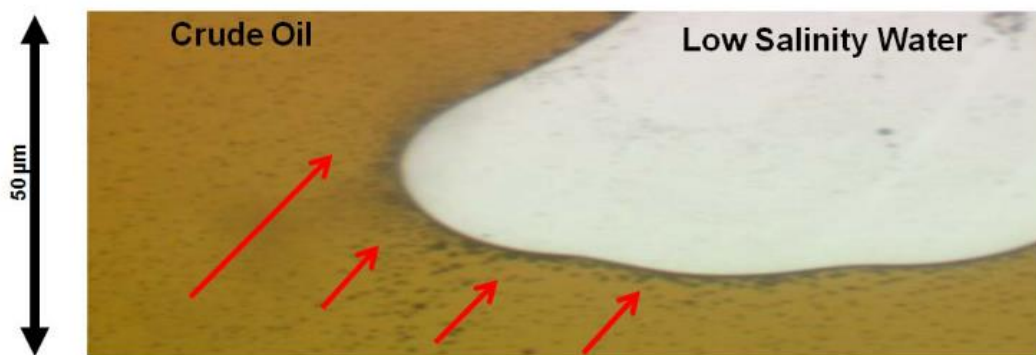


Figure 2 – A magnified image of the micromodel that depicts dark particles' formation (Emadi & Sohrabi, 2013).

The microdispersion formation theory could justify the additional oil recovery during LSWI, regardless of rock type and wettability (Sohrabi et al., 2017; AlHammadi, Mahzari, & Sohrabi, 2018). The microdispersions were clusters of water surrounded with oil surface-active materials that could assist the detachment of surface-active materials from the rock surface leading to wettability alteration toward a more water-wet state (Mahzari et al. 2018; Mahzari & Sohrabi, 2014; Facanha et al. 2017). Two illustrations presented in figure 3 show the organization of indigenous surface-active oil materials in low salinity (right) and high salinity (left). In a high salinity environment (left), surface-active agents adhere to the rock surface, creating oil-wet conditions. However, when water with low salinity comes in contact with oil, the formation of water-in-oil microdispersions takes place, and natural surface-active components of the oil phase migrate from the rock to the fluid/fluid interface surrounding the micro-dispersions (Mahzari et al., 2018).

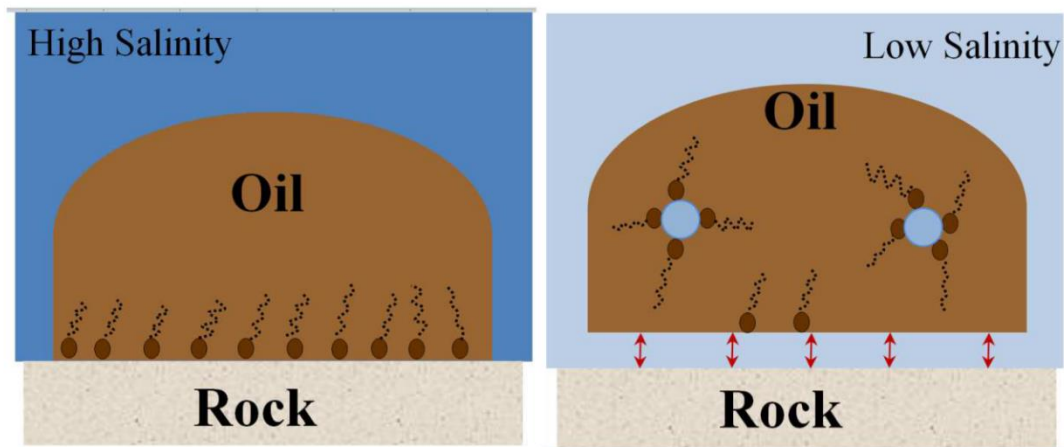


Figure 3 – Two illustrations show the organization of indigenous surface-active materials of oil in; low salinity (right) and high salinity (left) (Mahzari et al., 2019).

In addition to the studies mentioned above, the formation of an intermediate phase was also observed by other researchers (Bartels, et al., 2016; Bartels, et al., 2017).

The fluid-fluid and fluid-rock interaction were studied for carbonate reservoirs (Bartels, et al., 2017). Figure 4 shows the saturation versus time plots for sandstone and carbonate. The blue line represents brine, black line oil, and the red line, the intermediate phase (microdispersion phase) (Bartels, et al., 2017). Formation of an intermediate phase with higher density than brine and less density than oil is observed, which shows the emulsion formation when oil contacts brine. This happened in both sandstone and carbonate rock types, highlighting the importance of fluid/fluid interactions during water flooding. Different degrees of oil and water structure formation for different crude oils are given in Figure 5.

The right-hand side depicts a micro-CT scan of the interface between a crude oil with a high potency of forming micro-dispersions. The encircled portion of the image shows droplets below the imaging resolution (Bartels, et al., 2017).

Depending on the crude oil properties, mainly its surface-active components and its viscosity, water molecules can diffuse into the oil phase, creating water dispersions within the oil phase.

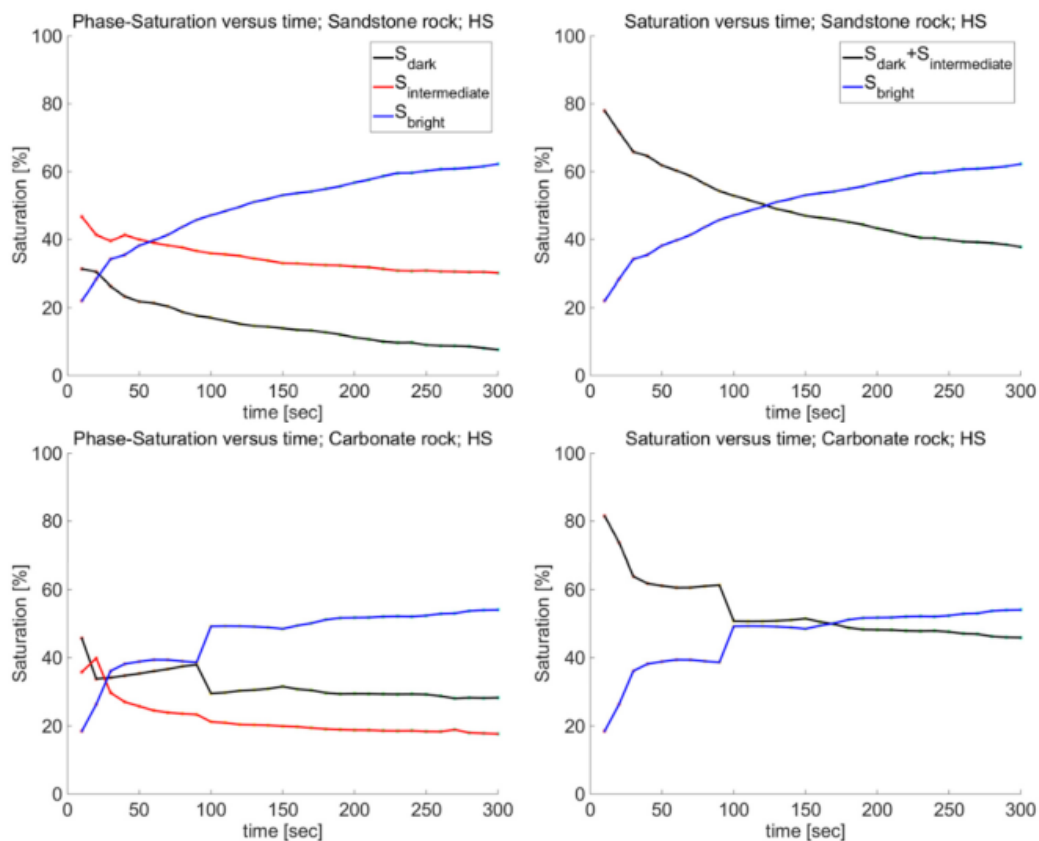


Figure 4 – Saturation versus time plots. The blue line shows brine, black line oil, and the red line, the intermediate phase (micro-dispersion phase) (Bartels, et al., 2017).

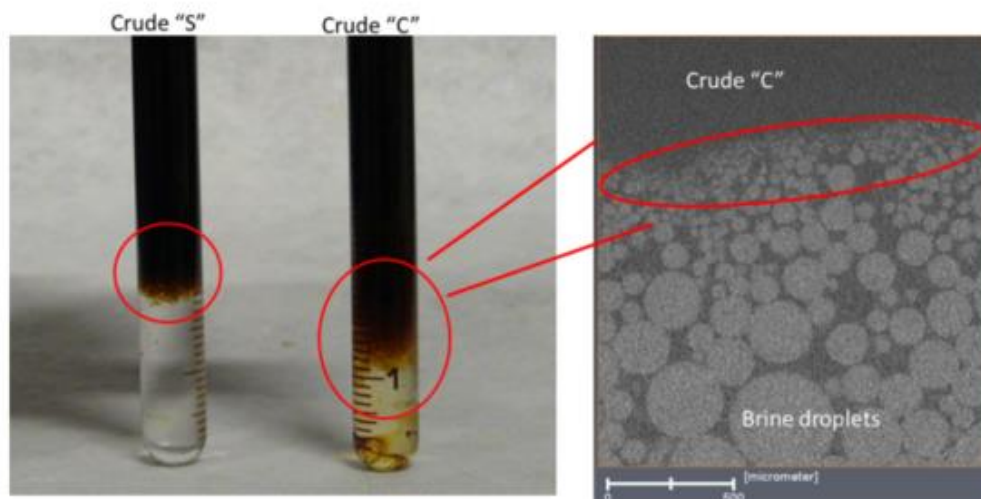


Figure 5 – Different degrees of oil and water structure formation for different crude oils (Bartels et al., 2017).

An experimental procedure was reported by Fattahi et al. (2020) for the fluid-fluid interaction, with the aim was to evaluate the potency of crude oils based on their ability to form micro

dispersions. The observation of water in oil microdispersions when oil comes in contact with brine with different salinities is shown in Figure 6. First, oil and brine were brought in contact; the interface is saturated with monomers of surface-active components. Then the oil and brine kept in contact for a period of time. Finally, after draining the aqueous phase, the sampling is done from the oil/water interface for the water content measurements (Fattahi Mehraban et al. 2020).

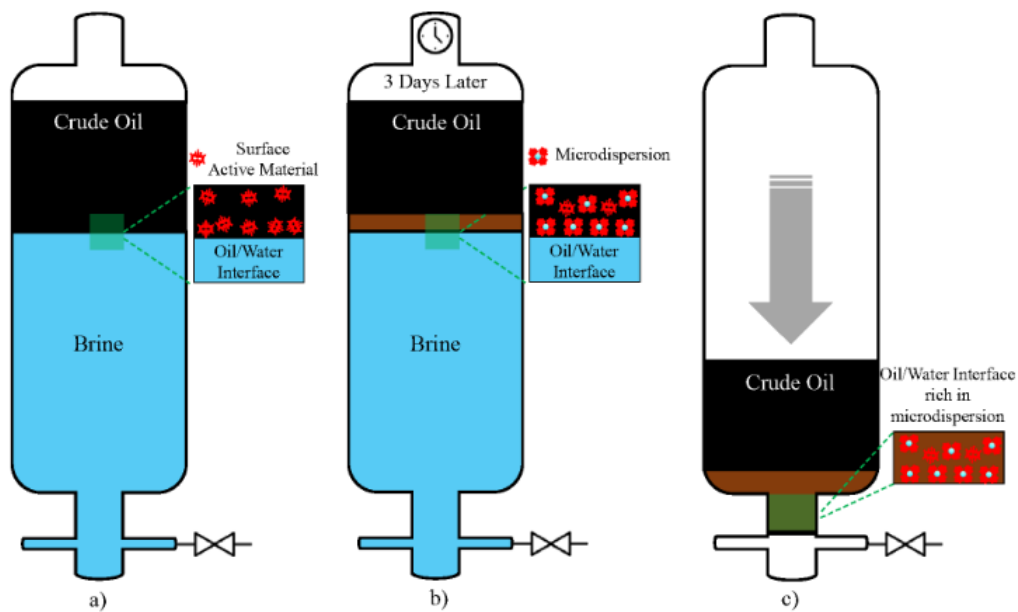


Figure 6 – Different degrees of oil and water structure formation for different crude oils (Bartels et al., 2017).

With microdispersions ratio having the definition based on the following formulation:

$$\text{Microdispersion Ratio} = \frac{\text{Water content of crude oil after contacting with brine}}{\text{Original water content of crude oil} - \text{Bond water}}$$

The feasibility study of LSWI for the carbonated reservoir was recently studied based on the microdispersion ratio (Masalmeh et al., 2019). The microdispersion ratio for 30 different crude oils after contacting with low salinity is shown in Figure 7. The reported microdispersion ratio values range from almost 1 to 10, with most data in the middle range and a few around the higher limit of 10 value. An excellent correlation was observed between the significance of the

microdispersion ratio data and the core flooding recoveries. It was reported that crude oils with microdispersion ratios of more than 4 were positive and led to high core flooding recoveries.

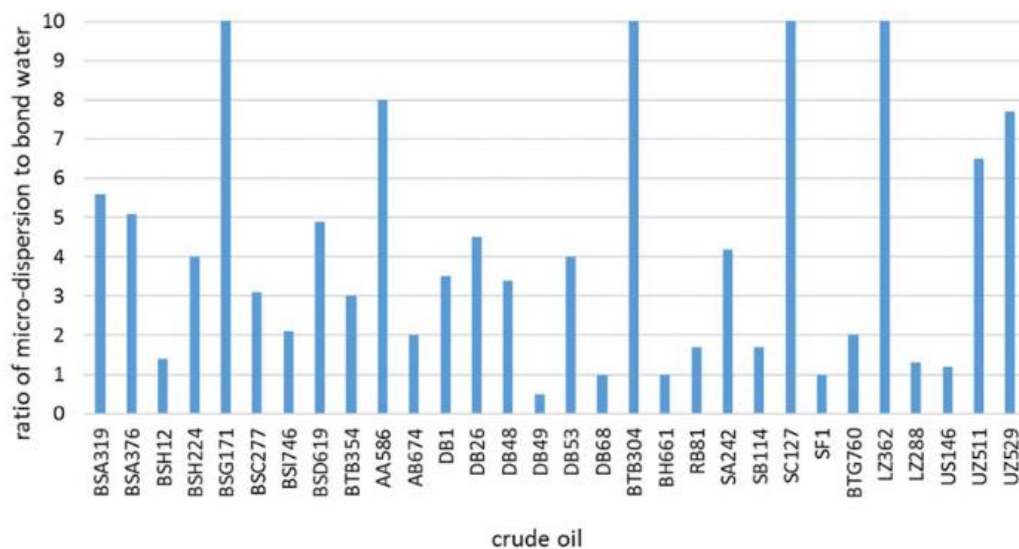


Figure 7 – Microdispersion ratios of 30 different crude oils after contacting with high salinity (204 kppm) and low salinity (240 ppm) (Masalmeh et al., 2019).

Based on recent studies, acidic compounds are mainly responsible for the formation of water in oil microdispersions after analyzing the oil and water interface through FT-IR spectroscopy (Fattahi Mehraban et al. 2020). Six different crude oil samples were contacted with brine of 500 ppm total dissolved solids (including NaCl, KCl, MgCl₂, CaCl₂, Na₂SO₄, and NaHCO₃) for the microdispersion ratio measurements. The FT-IR spectroscopy results for microdispersions revealed that they are highly composed of O-H, C=O, and C≡C bonds. This highlights the effect of acidic materials (C=O functional groups).

In addition to the spontaneous formation of water in oil microdispersions, other mechanisms were also introduced during LSWI in the area of fluid-fluid interaction, such as interracial viscoelasticity (Alvarado et al. 2014) and osmotic effects (Fredriksen et al. 2016).

Displacement of oil by water is a step-wise process rather than a continuous movement of phases. The applied viscous force is accumulated in the interface until it reaches a maximum of its full elasticity (Berg, et al., 2013). The oil cluster then experiences jumps which cause local acceleration of oil clusters. As a result, the more elastic the interface is, the higher the acceleration will be. With a higher degree of meniscus acceleration, the rate of coalescence of droplets increases. This leads to higher local oil saturation and higher oil mobilities.

Based on Berg et al. (2013), an experimental approach was taken to show the elasticity rule. As shown in tomography images, fluid redistribution of oil as a result of coalescence between clusters is illustrated in Figure 8. While applying a tension gradient on oil droplets during water injection, a film of water swells around the grains. This exerts tension on oil clusters and finally leads to snap-off events and cluster break up. Depending on the elasticity of the oil and water interface, the oil meniscus experiences some acceleration, leading to the coalescence of droplets. Therefore, the higher the elastic components of the viscoelasticity of the interface, the higher the rate coalescence of droplets should be. This is how interface viscoelasticity can affect fluid distribution inside porous media. The interface between crude oil and low salinity brine is reported to have higher elasticity than high salinity brine (Alvarado et al., 2014). Time-dependency is a crucial aspect of forming this elastic film, highlighting the effect of the aging of the core in the presence of the two fluids in place on ultimate recovery.

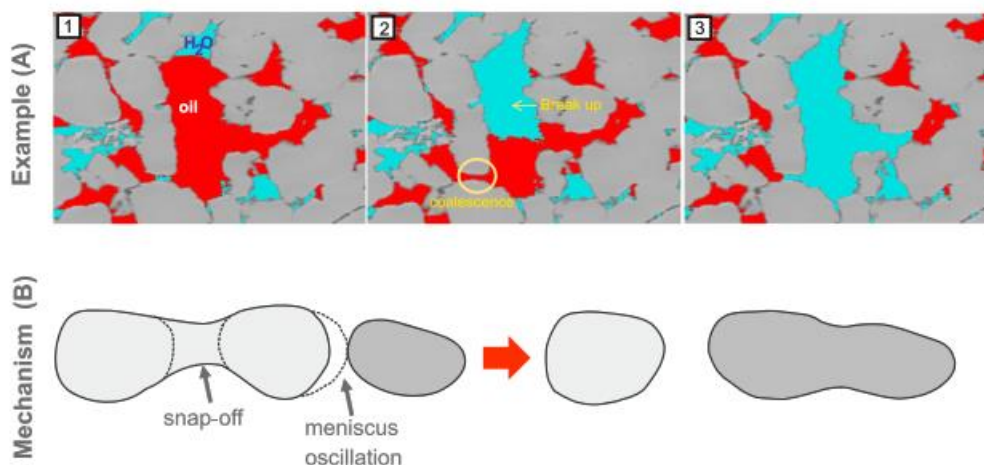


Figure 8 – Fluid arrangement of oil ganglia as a result of coalescence between clusters (Rücker et al., 2015).

The elasticity was reported to be affected by some ion addition. It was reported that brines with a concentration of sulfate and calcium ions successfully enhanced recovery (Zahid et al., 2012). The addition of the concentration of sulfate ions or reducing the salinity of injected water was reported to cause additional oil recovery by increasing the oil and water interface's viscoelasticity (Garcia-Olvera & Alvarado, 2017). Also, Barati et al. (2017) reported that the elastic component of the viscoelasticity of the interface could change non-monotonically when increasing the concentration of sulfate ions, as shown in Figure 9 (Barati et al. 2017).

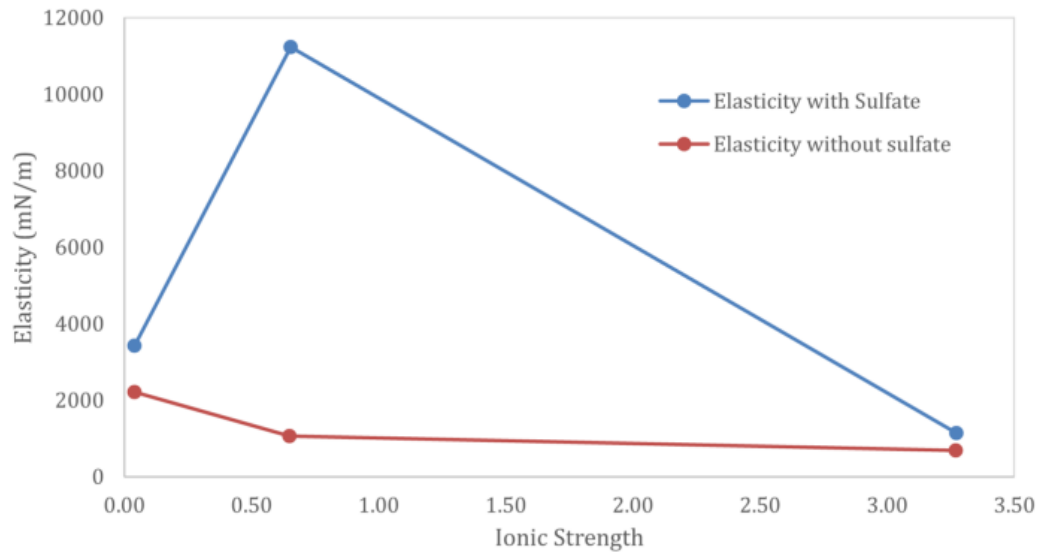


Figure 9 – The elasticity behavior of the interface based on different brine salinities with different sulfate concentrations (Barati et al., 2017).

Although many efforts have been made recently to investigate the fluid/fluid based-mechanisms, the formation of microdispersions after contacting the oil and low salinity brine has not been justified. Therefore, it is also the purpose of this study to investigate statistically the functional compounds of crude oil, mainly responsible for water in oil microdispersion and LSE.

Furthermore, we aim to derive a prediction model of the microdispersion ratio based on the critical crude oil and brine properties by collecting all available data from the literature.

Moreover, the additional scope of this study is to investigate the link between microdispersion formation and interface viscoelasticity. Microfluidic data will be interpreted to elucidate the impact of interface viscoelasticity on fluid distribution in porous media. This is the first time such an approach is exploited to investigate the impact of the viscoelastic response of interface in displacement processes.

Chapter 3

Theoretical explanation of the fluid/fluid mechanisms

This chapter discusses the theoretical explanation of the two mentioned mechanisms concerning fluid/fluid interactions.

3.1 Formation of water in oil microdispersions

The impact of fluid/fluid interactions during low salinity water injection had been underestimated until micro-dispersion formation was introduced as one of the main responsible mechanisms of LSWI (Mahzari et al., 2014). The micro-dispersion formation hypothesis could justify the increased recovery during low salinity water injection irrespective of rock mineralogy. Microdispersions are reverse micelles of water molecules surrounded by oil indigenous materials. Hence, when the concentration of acidic components at the interface increases, the formation of micro-dispersions of water in the oil phase occurs, as shown in Figure 10.

Crude oils react differently with the contrasting brines and exhibit different propensities toward low salinity and high salinity brines in terms of microdispersion formation. The different abilities of oil samples for micro-dispersion formation originates in the physicochemical characteristics such as asphaltene molecules and total acidic components. It worth mentioning that microdispersion formation cannot occur outside the interface area. This is a pure fluid-fluid interplay taking place at the interface. However, the microdispersion phase can span over relatively long distances from the interface as well.

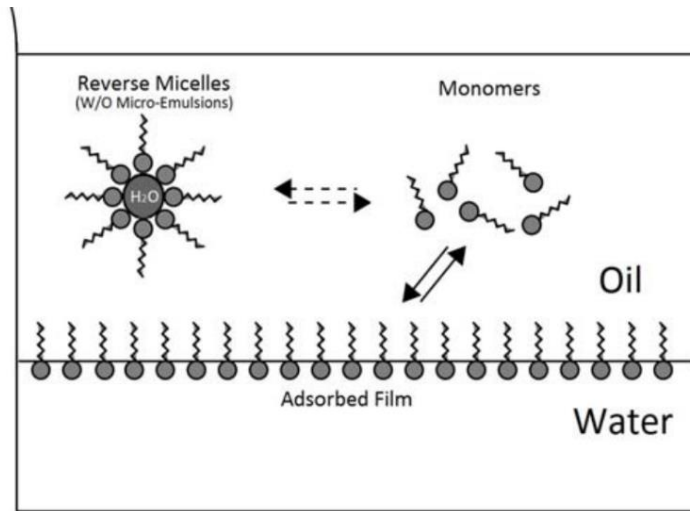


Figure 10 – The schematic representation of the three environments (adsorbed film, monomer and, micelle or W/O micro-dispersions) in which surface-active components reside in the oil phase (Emadi et al. 2013).

When LSW is introduced into the porous media, the polar components of crude oil have a preference to interact with water molecules rather than the rock surface. Consequently, these surface-active components are adsorbed into the oil/LSW interface and form microdispersions. This can result in oil swelling and wettability alteration, as shown in Figure 11. As a result, the swelled oil ganglia restrict the injection water flow and change it toward unswept regions. Additionally, oil swelling increases the hydraulic discontinuity in injection water flow, and consequently, the pressure drop across the porous media would increase, and the microscopic sweeping efficiency improves.

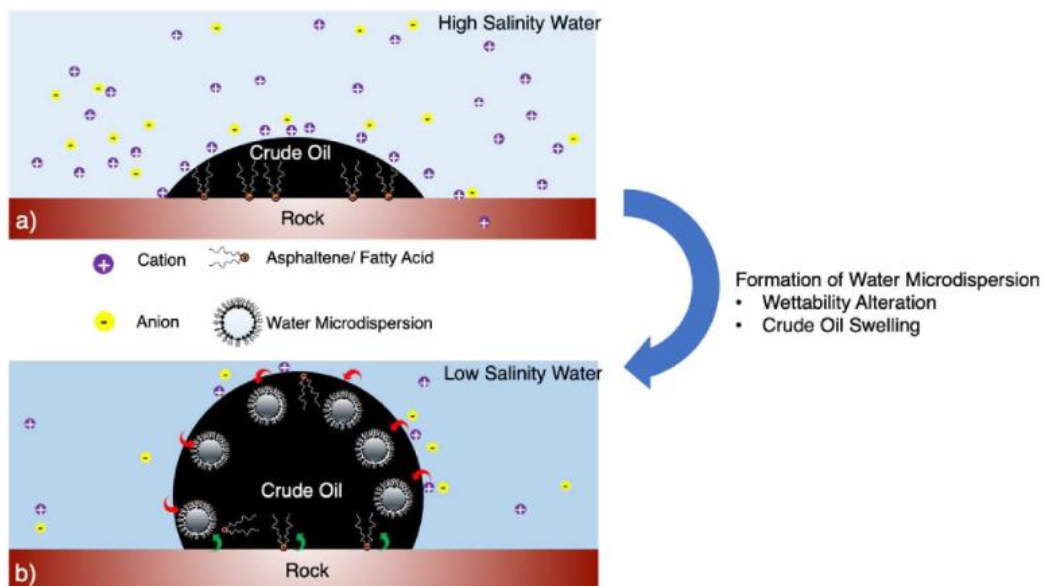


Figure 11 – Schematic of the effect of microdispersion formation on oil swelling and possible detachment of crude oil from the rock surface (Fattahi Mehraban et al. 2020).

3.2 Interfacial dilatational viscoelasticity

The interfacial rheological properties of crude oil and brine interfaces have been of interest for many years (Kumar et al., 2001; Varadaraj et al., 2012). This research topic has been investigated by the need to understand the mechanisms that control the stability of the emulsions formed during oil production (Kilpatrick, 2012; Moran et al., 2006). Efforts to characterize the material of the interfacial film led to the introduction of natural constituents of crude oil such as asphaltene molecules and naphthenic acids. (Varadaraj et al., 2007). Asphaltenes are a class of crude oil components soluble in aromatics, e.g., toluene, but insoluble in low-molecular-weight alkanes such as n-pentane or n-heptane. Naphthenic Acids (NAs) are another fraction of crude oil, which comprises all alkyl-substituted cyclic and carboxylic acids present in the crude oil with the general formula of R-COOH. NAs are somewhat hydrophilic; thus, they tend to accumulate at the brine/crude oil interface. In addition, they can partition and dissociate in the aqueous phase forming naphthenate salts, which are also amphiphilic molecules that can also accumulate at the crude oil/brine interface.

It is often in the literature, the so-called model oil, i.e., a mixture of asphaltene molecules that are precipitated from crude oil, heptane, and toluene has been used for experimental investigations. In model oils, structures of asphaltene molecules might differ significantly from their native state in crude oil. When crude oil is used instead of model oil, in addition to asphaltenes, NAs and their salts tend to occupy the interface as well. Therefore, competitive adsorption of both asphaltene and naphthenic molecules controls the mechanical properties of the interface. As a result, the interfacial response is a combined effect of the adsorption of both asphaltene and naphthenic components (Moradi et al., 2016).

The number of different classes of components in crude oil as given by SARA analysis does not explicitly describe the ability of crude oil components to cover the interface (Aske et al., 2002). In addition to the amount of potentially interfacial active components, their physical and/or chemical properties probably determine their adsorption behavior.

The formation of organized molecular structures at the fluid/fluid interfaces increases the viscoelastic property of the interface. For example, in the human body, surfactants give the tissue of our lungs adequate elasticity to expand and contract during each breathing cycle (Lalchev et al., 2008). Surfactants may also increase the elasticity of the eye drops in the eye, forming tear films to prevent them from dewetting and maintaining the eyes' humectant (Rosenfeld et al., 2012). In both examples, the viscoelasticity of the interface increases the thin film stability.

Interfacial rheology relies upon surface modifications that are induced by mechanical forces, like shear or dilatational stresses. Interfacial studies generally include two types of measurements: static analysis, which focuses on the determination of equilibrium interfacial tension (IFT), and dynamic analysis, which measures mechanical interfacial moduli under non-equilibrium or transient states. The latter provides information about the changes of dynamic IFT as well as interfacial viscoelastic properties and can be determined through dilatational or shear rheology experiments. Several researchers have dedicated efforts to elucidate the mechanisms about the formation of the interfacial film (Yang et al., 2007; Sheu et al., 1992). Two different phenomena are involved in interfacial film formation. The first is diffusion from the bulk phase to the interface, and the second is molecular rearrangement or interfacial diffusion. Therefore, at least two kinetics control the formation of the interfacial film: bulk diffusion and molecular rearrangement or interfacial diffusion at the interface (Moran et al., 2007).

In reality, we cannot separate different diffusional processes or interfacial re-arrangements for experiments; hence, our analysis is rather low-level estimations. However, to simplify the problem, we assume that diffusion of the interfacial-active material from the bulk of the oil phase is similar to the diffusion of spherical particles and obeys the Stokes-Einstein equation as follows:

$$D = \frac{k_{\beta}T}{6\pi\mu r} \quad \text{Eq. 1}$$

Where D is the diffusion coefficient, k_{β} is the Boltzmann constant, T is the absolute temperature, μ is the viscosity of the bulk phase, and r is the diffusing particle's radius. Suppose we assume that all of the interfacial-active components have the same size. In that case, the formation rate of the interfacial film should be related to D , which is equivalent to proportional to the ratio between the absolute temperature and viscosity.

Several devices and measuring probes have been used to evaluate the rheological properties of the interface. In general, rheological measurements can be performed by applying either shear or dilatational deformation (Fan et al., 2010; Spiecker et al., 2004; Lucassen et al., 1972; Ravera et al. 2010). The primary difference between the two methods is that, in the second one, i.e., dilatational deformation, the interfacial area changes in contrast to shear deformation. In other words, in shear rheology, the concentration of the interfacial material is not affected by the deformation.

Dilatational rheology is of great significance for systems containing surfactants or, generally, for composite interfacial layers where the interfacial tension changes due to diffusion or surface

relaxation processes (Ravera et al., 2010). For these systems, a viscoelastic modulus, or dilatational viscoelasticity, can be attributed to the interface properties to characterize its dynamic response to expansions or compressions. Moreover, the close link between the adsorption mechanisms and the interfacial layers' dynamic properties makes dilatational rheology a crucial tool to investigate the characteristic properties of the transport and the kinetics of processes determinant for the adsorption re-equilibration and the physicochemical properties of the system.

The dilatational viscoelasticity or complex modulus is a quantity that expresses the relationship between the surface modifications of an interfacial layer and the related dilatational stresses. Due to the connection with the dynamic properties of the interfacial layers, the complex modulus is crucial, more importantly, because of its functionality with the frequency of the area oscillation signal.

The dilatational stress of an interfacial film is the change of the interfacial tension from its initial state γ^0 to a general value at the time t , i.e., $\Delta\gamma = \gamma(t) - \gamma^0$ while the related surface variation is the expansion and/or contraction of the surface area A . For a purely elastic dilatational behavior, the surface stress is proportional to the relative area variation as:

$$\alpha = \frac{\Delta A}{A^0} = \frac{(A(t) - A^0)}{A^0} \quad \text{Eq. 2}$$

However, the interfacial layer may have a viscous characteristic due to the occurring of relaxation phenomena. Thus, in general, the dilatational stress can be written as the sum of the two terms: one purely elastic proportional to α (relative area variation) and the second as a viscous contribution, proportional to the rate of the surface deformation (the derivative of the relative area variation concerning time), $\dot{\alpha} = d\alpha/dt$.

Therefore, the general expression for the dilatational stress is then:

$$\Delta\gamma = E_0\alpha + \eta\dot{\alpha} \quad \text{Eq. 3}$$

The above equation leads to a definition of the complex dilatational viscoelastic modulus or the dilatational viscoelasticity. For a low amplitude harmonic perturbation of frequency, the area perturbation can be expressed as $\Delta A = \tilde{A}e^{i2\pi\nu t}$, which by introducing it in the above equation gives:

$$E = E_0 + i2\pi\nu\eta \quad \text{Eq. 4}$$

The real part is called dilatational elasticity and represents elastic energy storage, while the imaginary part is called dilatational viscosity and is attributed to the dissipation of viscous energy.

The complex modulus involves elastic, viscous, and transport properties. In addition to interfacial effects, diffusional exchange between the interface and bulk solution during perturbations will occur. This will cause some degree of short-circuiting of the tension gradients, leading to an apparent lower interfacial elasticity or storage modulus. In addition, interfacial relaxation processes will accompany this transport effect. None of these last two effects are instantaneous as the elasticity but will lag the perturbations of the interfacial area. This creates the viscous effect and a phase angle that can be measured between the dilatational strain (change in the area) and the stress (change in interfacial tension).

The two viscosity effects cannot be easily distinguished from each other, but they are generally dependent on the frequency of the oscillations. The effect of diffusion is less critical in experiments with high oscillation frequencies due to the fact that the time for diffusion will be shorter in such cases. On the other hand, interfacial relaxation processes are considered very fast in most cases compared to bulk diffusion. This means that such effects might not be seen in experiments with low oscillation frequencies. Any deviation from equilibrium initiates various relaxation processes at the interface as well as in the adjacent bulk solution. Therefore, the interfacial tension oscillates having the same frequency as the oscillations of the area variation. For a small-amplitude harmonic oscillation of the surface area, the magnitude and the phase shift of the variation of the interfacial tension are directly related to the dilatational viscoelasticity based on Equation 4.

In addition, the mechanical interfacial moduli can be representative of the physical state of the interfacial film, i.e., a higher elastic modulus corresponds to a more rigid film, and a higher viscous modulus is linked to a more liquid-like film.

Several theoretical studies exist in literature correlating the $E(\nu)$ to diffusional exchange, surface re-organizations, and other kinetic processes happening at the interfacial layer (Lucassen et al. 1972; Fainerman et al. 2002; Fainerman et al., 2004; Kovalchuk et al. 2005; Kovalchuk et al. 2004). These theoretical approaches provide expressions of $E(\nu)$ in terms of the principal parameters related to the kinetics of the adsorption layers and thermodynamics.

In order to get the frequency trend of the complex modulus, the oscillating drop experiments are usually done by applying periodical oscillations to the surface area A . Thus, for each frequency ν we have:

$$A = A^0 + \tilde{A} \sin(2\pi vt) \quad \text{Eq. 5}$$

Where A^0 and \tilde{A} being the median and the amplitude of the signal of the area perturbation.

The harmonic variation of the interfacial tension γ will be:

$$\gamma = \gamma_0 + \tilde{\gamma} \sin(2\pi vt + \phi) \quad \text{Eq. 6}$$

where γ_0 is the equilibrium surface tension and $\tilde{\gamma}$ the amplitude of the surface tension oscillations. The angle Φ is the phase shift between the area variation and the interfacial tension.

In fact, according to Equation 4, we can write the complex modulus based on the parameters, which can be experimentally measured, i.e., the amplitudes of the signal of the interfacial tension and area and the median of the signal of the oscillating surface area, as in the form of Equation 7:

$$E = \frac{\tilde{\gamma}}{\tilde{A}/A_0} \text{EXP}(i\phi) \quad \text{Eq. 7}$$

The above equation expresses E in terms of quantities that can be experimentally determined as frequency functions either directly or using an appropriate calculation procedure depending on the utilized tensiometer.

When the oscillating drop/bubble method is applied, interfacial tension against time is directly measured while a controlled harmonic perturbation is applied to the surface area.

The experimental signals extract the amplitudes and the phase angle via DFT (Discrete Fourier Transform) algorithms. At each frequency, the complex dilatational modulus is then calculated according to 7. As an example, acquired data during a surface perturbation are shown in Figure 12.

Finally, the extracted theoretical quantities are utilized to calculate the complex dilatational viscoelasticity from the acquired data.

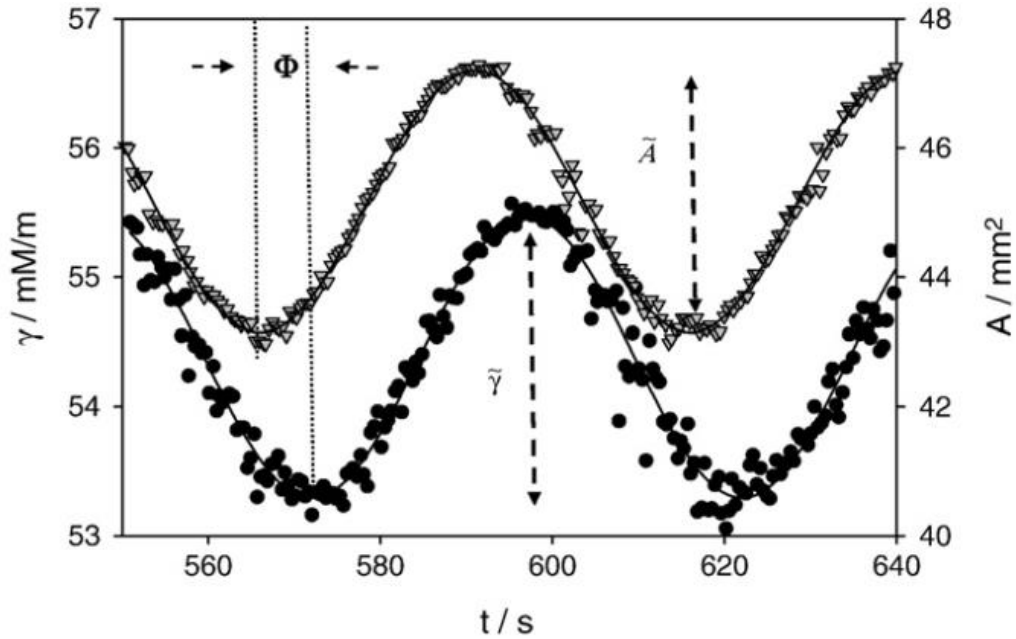


Figure 12 – Example of acquired surface tension (O) and surface area (∇) by the oscillating drop method (Ravera et al. 2010).

Pendant drop and spinning drop techniques are the systems most often used to perform dilatational rheology. By applying periodic perturbations of interfacial area, these techniques allow the acquisition of the interfacial tension's response for the low-frequency range, i.e., 10^{-5} - 10^{-1} Hz. At faster oscillations, a threshold for frequency appears when the interface is no longer in mechanical equilibrium. When increasing the frequency of the area oscillation, a threshold may be overcome where the interface is no longer at mechanical equilibrium since shape distortions occur by viscous forces leading to triggering of drop/bubble normal oscillation modes. Regarding this threshold for frequency, studies showed that for the amplitude of the area variations less than 10%, the droplet is considered mechanically at equilibrium for frequencies less than 0.1 Hz for viscous fluids (Liao et al. 2004; Freer et al. 2005; Leser et al. 2005).

Based on the interfacial rheological characterizations, interfacial viscoelasticity generally increases as brine salinity is reduced, regardless of cations and anions present (Alvarado et al., 2014). However, the build-up rate of the elasticity and the plateau value depends on the solution's specific ions. The impact of low salinity on the viscoelasticity of the interface can be explained in terms of the electrostatic interactions at the interface. The electrical double-layer expansion, which was used to explain the effect of the low salinity on the rock/fluid interactions, might be the reason for the high amount of surface-active components of oil at the fluid/fluid interface. Ions are adsorbed to the electrically negatively charged crude oil/brine interface to form a diffuse ionic layer at the vicinity of the interface. This diffuse layer of ions screens all

the interactions with the bulk of the solution. The effective thickness of this diffuse layer is related to the Debye length, κ^{-1} , expressed as:

$$\kappa^{-1} = \left(\frac{\epsilon_r \epsilon_0 k_B T}{2 N_A e^2 I} \right)^{1/2} \quad \text{Eq. 8}$$

where the nominator involves the product of the dielectric constant, the free space's permittivity, Boltzmann constant, and temperature, respectively. Whereby and denominator consists of the Avogadro number, the electron charge, and I the ionic strength, which is defined as follows:

$$I = \frac{1}{2} \sum_{i=1}^n c_i z_i^2 \quad \text{Eq. 9}$$

In the above equation, c and z are the concentration and the valence of each component in the system. As shown in Figure 13, in the absence of salts, oil polar and interfacial-active components may be adsorbed to the crude oil/brine interface. At low concentrations, the Debye length is high, and the diffuse layer is extensive. Therefore, the screening should be stronger, and the polar components of the oil are organized and adsorbed to the crude oil/brine interface by attractions of electrostatic forces. At the high ionic content of the brine, the Debye length is shorter, which reduces the screening of the charges causing a reduction of the attraction of the polar components to the interface.

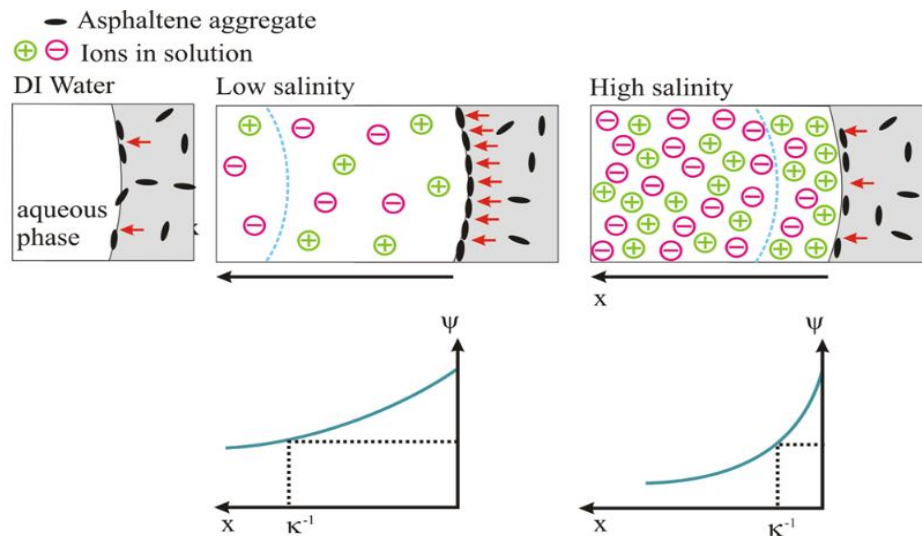


Figure 13 – The effects of ions on the electrostatic potential (ψ) as well as the Debye length (dashed line) at the oil/water (with variant salinity levels) interface (Chávez-Miyauchi et al. 2016).

Another essential aspect that has been the subject of intense research is the relationship between dilatational rheology and the properties of liquid films and/or dispersed systems like emulsions and foams (Kovalchuk et al., 2009; Santini et al., 2007). The response of the interfacial layer to dilatational stresses expresses its capability of damping the external areal disturbances.

Therefore, the $E(\nu)$ feature can be relevant for stability conditions of liquid films subjected to dynamic disturbances and consequently for the drop/bubble coalescence in emulsions and foams. Correlations between dilatational rheology of the single liquid/liquid interfaces and emulsion stability are discussed on the basis of viscoelasticity data obtained for emulsions (Santini et al. 2007; Kalogianni et al., 2010). Several authors studied crude oil/brine interfacial rheology in relation to the stability of water-in-oil emulsions (Spiecker et al., 2004; Quintero et al., 2009). They related the elasticity of the fluid/fluid interface to the strength of emulsions due to the formation of structured arrangements of amphiphilic molecules in crude oil regarding the salt concentration of the aqueous phase. In Figure 14, the upper part shows the Critical Electric Field (CEF) at which current percolation occurs through water in oil emulsions as a function of brine salinity for Na_2SO_4 aqueous solutions. The higher CEF corresponds to the more stable emulsion. In the lower part of Figure 14, the measured elasticity of the interface versus aqueous phase salinity (pure sodium sulfate solution) is depicted. As can be seen, the CEF and interface elastic modulus are in reasonably fair agreement as they both experience an increase as the salinity of the aqueous solution reduces and has a maximum at about 950 ppm salinity of the sodium sulfate solution.

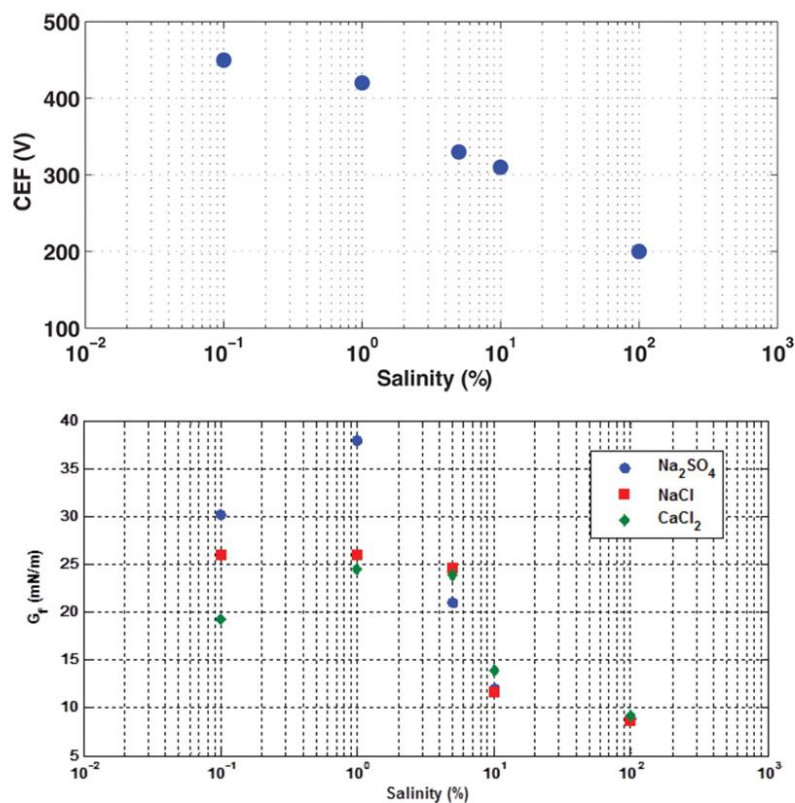


Figure 14 – Top: CEF as a function of the salinity of brine for Na_2SO_4 aqueous solution. Bottom: Interface elasticity of the crude oil/brine interface versus aqueous phase salinity (Moradi et al. 2016).

Alvarado et al. (2014) reported an increase in storage modulus as the salinity is reduced and observed a maximum of 38 mN/m for the Na_2SO_4 concentration of 6.724 mM (0.09 wt% or 950 ppm). By using the low salinity brine in a water injection test in rock samples, they reported an increase in oil recovery of 20% in water injection compared to high salinity water injection (0.6724 M or 9 wt%) (Alvarado et al. 2014). The increase in oil recovery is anticipated due to the high elasticity of the oil/brine interface. The elasticity is suggested to hinder the snap-off of the oil clusters into small droplets, leading to a more continuous phase that can be swept more easily. It is believed that interfacial active molecules lower the interfacial tension at the interface between two fluids. However, they may also decrease or increase the viscoelastic property of the oil and brine interface. Therefore, the interface's viscoelasticity may increase recovery rather than changing thermodynamic properties such as the interfacial tension.

Specially designed injectors to investigate snap-off processes highlighted the role of viscoelasticity on the suppression of clusters break up (Liu et al., 2019). Figure 15 shows the image of the designed flow-focusing device to investigate the crude oil/brine interface elasticity and its impact on the snap-off of the crude oil.

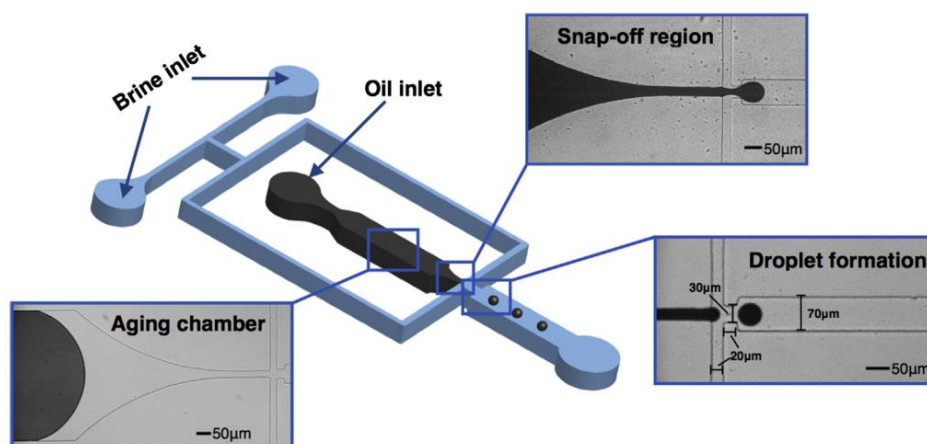


Figure 15 – The schematic of the flow-focusing device for the snap-off experiment (Liu et al. 2019).

Furthermore, the ionic content and concentration of brine is an essential parameter for the cluster volume in the case of snap-off. The lower the brine salinity, the larger the oil droplets should be. Figure 16 shows the micrograph of the flow-focusing device used in the snap-off experiments. As the oil enters the device, after having 1 hour of aging time between crude oil and the brine, the oil is pushed through up the channel for the snap-off experiment.

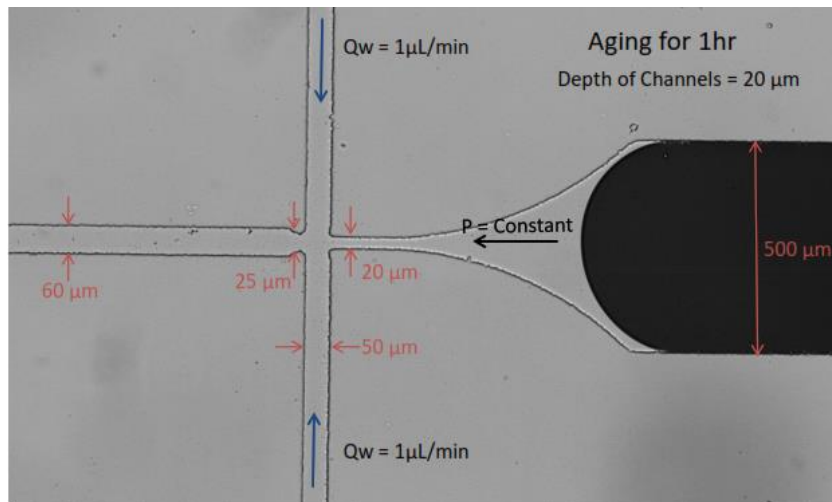


Figure 16 – The flow-focusing device for the snap-off experiment (Alvarado et al. 2014).

Figure 17 shows the resulting oil droplet after snap-off. The oil droplet after the break-up is substantially more prominent with the low salinity brine (1%, 950 ppm Na_2SO_4 solution) compared to the high salinity brine (100%, equivalent to 95000 ppm Na_2SO_4 solution). The crude oil and aqueous solution were the same as Moradi et al. (2016) which their elasticity is shown in Figure 14.

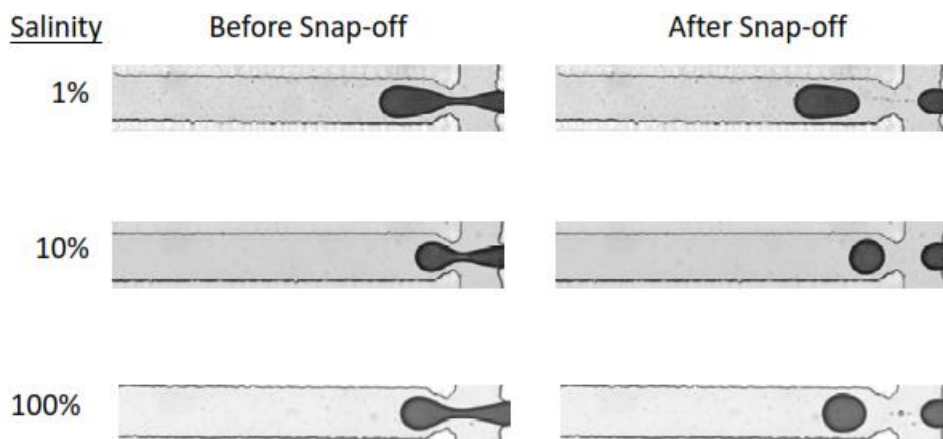


Figure 17 – The resulting oil droplet after snap-off (left) and after snap-off (right) for brines with different salinities (100% is equivalent to 95000 ppm Na_2SO_4 solution) (Alvarado et al. 2014).

In addition, elastic film formation is a time-dependent phenomenon. The viscoelastic characteristics of the brine and crude oil interface are sensitive to aging time (the time the two fluids are in contact) because of different kinetics, such as diffusion, adsorption, and rearrangement of interfacial-active components, control the rate of film development (Fan et al. 2010). Figure 18a demonstrates the effect of the aging time of crude oil and aqueous brine solution with 950 ppm Na_2SO_4 solution (which had the highest elastic modulus) normalized to the corresponding mineral oil (synthetic oil) drop area, which was set to a baseline value of zero. The difference of drop area with the one using mineral oil was utilized to identify a

threshold of the aging time. Aging crude oil with 95000 ppm sodium sulfate solution resulted in similar behavior with synthetic oil having approximately the same droplet area. Similar to short aging times of less than half an hour between crude oil and brine of low salinity (950 ppm). Higher aging times resulted in increased droplets which can be attributed to the fact that the interface viscoelasticity builds up to suppress snap-off. Aging for times greater than 1 hour resulted in even more dramatic snap-off suppression, characterized by very large resulting oil droplets (formed drop areas in excess of $1200 \mu\text{m}^2$). Therefore, suppression of snap-off requires enough contact time between the two fluids, which corresponds to the build-up of interfacial elastic properties. Figure 18b illustrates the impact of aging time on snap-off events. As can be seen, a sharp increase in the droplet area is evident after around one hour, which again highlights the importance of the aging time of the interface on the snap-off of the oil clusters.

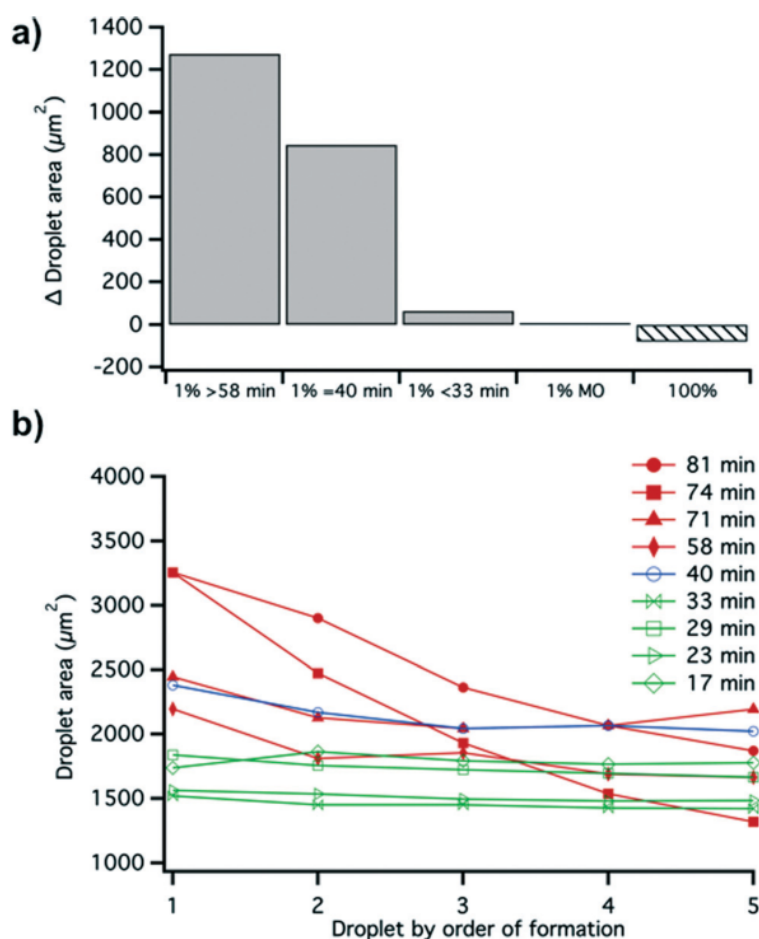


Figure 18 – a) The effect of aging time on snap-off behavior. b) droplet area of the first five sequential droplets formed for various aging times (Morin, Yafei, & Alvarado, 2016).

Chapter 4

Methodology

In order to investigate microdispersion data statistically, all available data from the literature were collected to examine the parameters which are essential for microdispersion and microdispersion ratio. The collected data and their references are given in Appendix A. In addition, a machine learning algorithm has been implemented to derive a relationship between the microdispersion ratio and crucial parameters of crude oil and brine. The software R is used to implement the machine learning algorithm, and the code can be found in Appendix B.

Furthermore, a set of laboratory measurements has been conducted to measure some crude oil and brine properties. These measurements are SARA (Saturate, Aromatic, Resin, and Asphaltene) components of crude oil, separation of asphaltene molecules from crude oil, brine and oil densities, crude oil viscosities, and dilatational viscoelasticity of crude oil and brine interface. In the end, data from microfluidic experiments have been used and analyzed to investigate the effect of interfacial viscoelasticity on fluid distribution inside porous media.

4.1 Statistical analysis of microdispersion data from the Literature

In this section, a statistical investigation of microdispersion data from the literature is conducted. First, all available data from the conducted tests are collected to investigate the crude oil and brine properties effect on microdispersion formation. Then, a logistic modeling approach is implemented to predict the significant degree of the microdispersion ratio based on the crude oil and brine properties. Finally, above the prediction value, the aim is to determine crucial parameters for this phenomenon based on the published experimental results from the literature.

4.1.1 Logistic regression of the microdispersion ratio

All available data of microdispersion ratio reported in the literature and the corresponding crude oil and brine properties are given in Appendix A. Among the published data of different

authors, the data with a similar measurement procedure was selected. Hence, the Sohrabi group of Herriot Watt University data was more consistent regarding microdispersion measurement.

In addition to the reported crude oil data (i.e., SARA components, TAN, TBN), CII, and As/R (Asphaltene over Resin ratio) been generated from the SARA components. The reason was to see whether asphaltene molecules have any role in forming microdispersions from the data.

The Colloidal Instability Index (CII) is used to characterize crude oils regarding the precipitation of asphaltene molecules (Sulaimon et al. 2020) and is defined as Equation 10:

$$CII = \frac{Asphaltene+Saturate}{Resin+Aromatics} \quad \text{Eq. 10}$$

Figure 19 shows the contribution of each paper to the collected data from the literature. The spontaneous formation of water in oil microdispersions is recently proposed as one of the LSWI mechanisms. Therefore, the first data was published in 2018, followed by some other works in the following years.

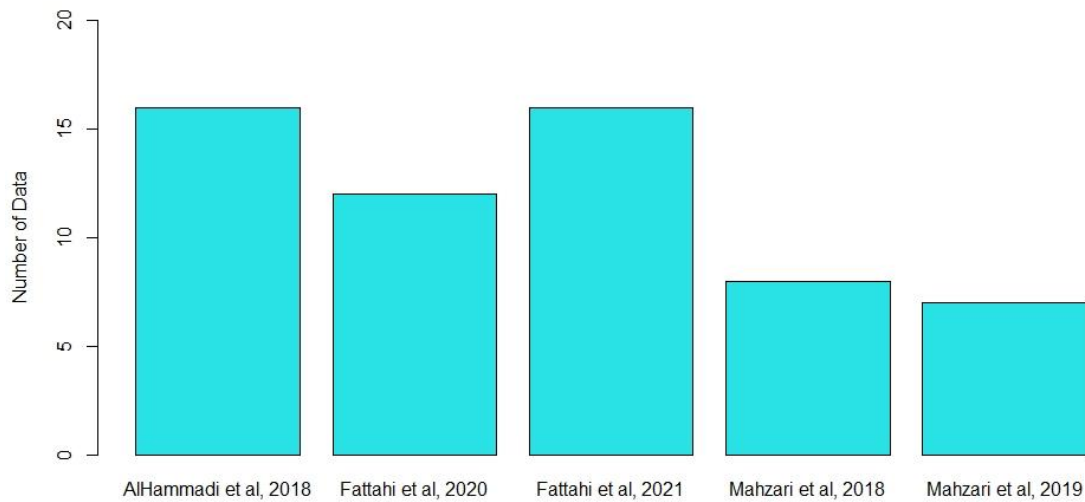


Figure 19 – The papers and their contributions used for the statistical analysis.

The majority of the reported microdispersion ratios are in the range of 1 to 30, as shown in Figure 20. In general, Fattahi et al. (2020) and Mahzari et al. (2019) reported significantly higher microdispersion ratio values than others with data exceeding the value of 20.

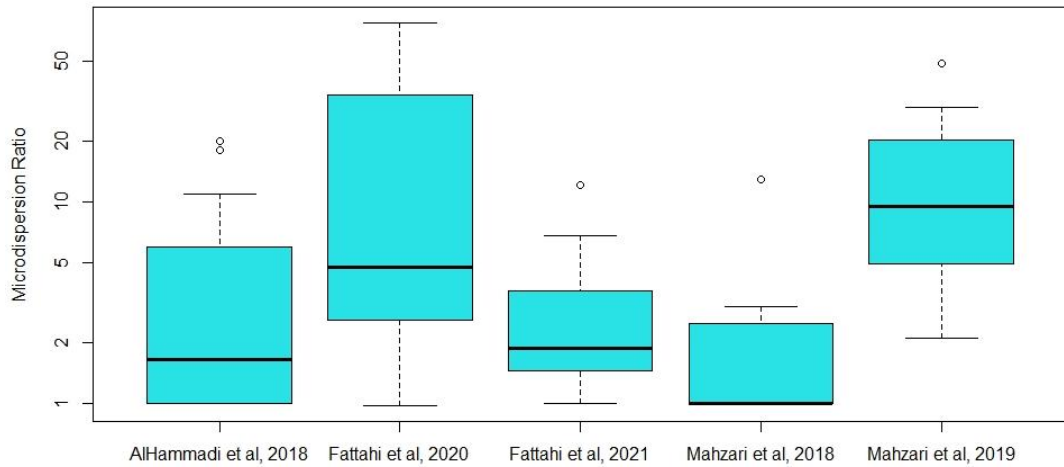


Figure 20 – The boxplot of the data from each published paper, showing statistical fingerprints of each data set.

In general, as depicted in Figure 21 (the violin plot), most data stands in the lower range, i.e., below 4; the rest are higher, with a few outliers exceeding the ratio of 30.

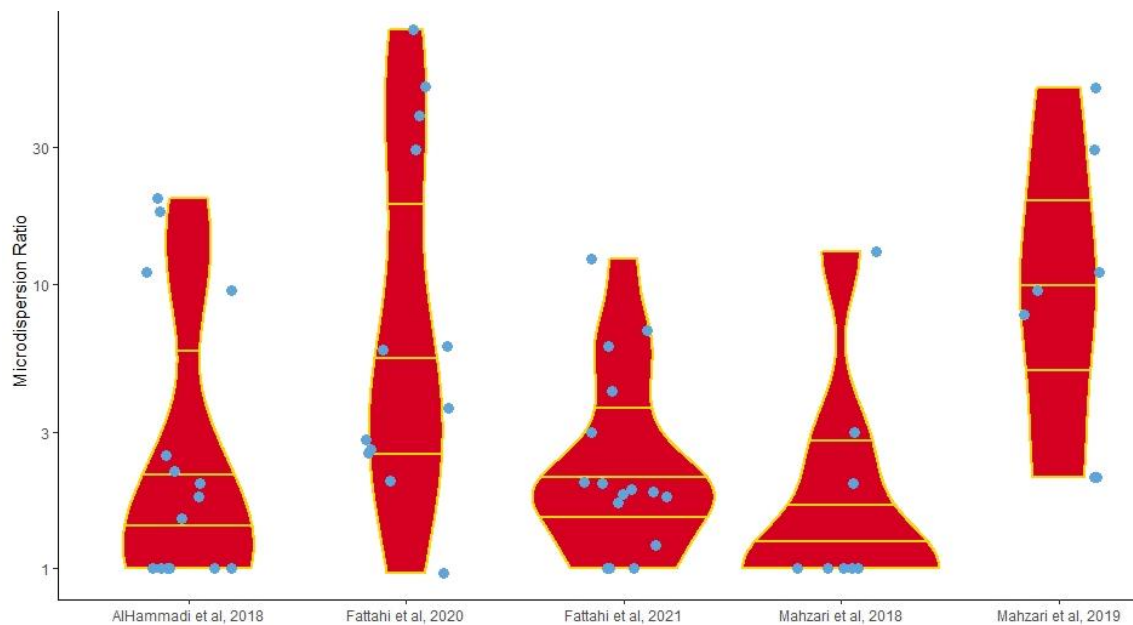


Figure 21 – The violin plot of the published data from each paper, including statistical characteristics of each data set.

The reported measurements were done at 20 and 60 degrees centigrade. As shown in figure 22, the temperature seems to have a minor impact on the formation of microdispersions as the red box in Figure 22 contains higher values, and the median (the black line inside the box) for this temperature interval is a little bit higher than the one for the lower temperature (20-degree centigrade). It should be mentioned that in Figure 22, the black dots belong to the box plot representation. Therefore, they are the outliers among the rest of the data. In addition, the blue points show the whole data points in each category with a randomly assigned degree of scattering.

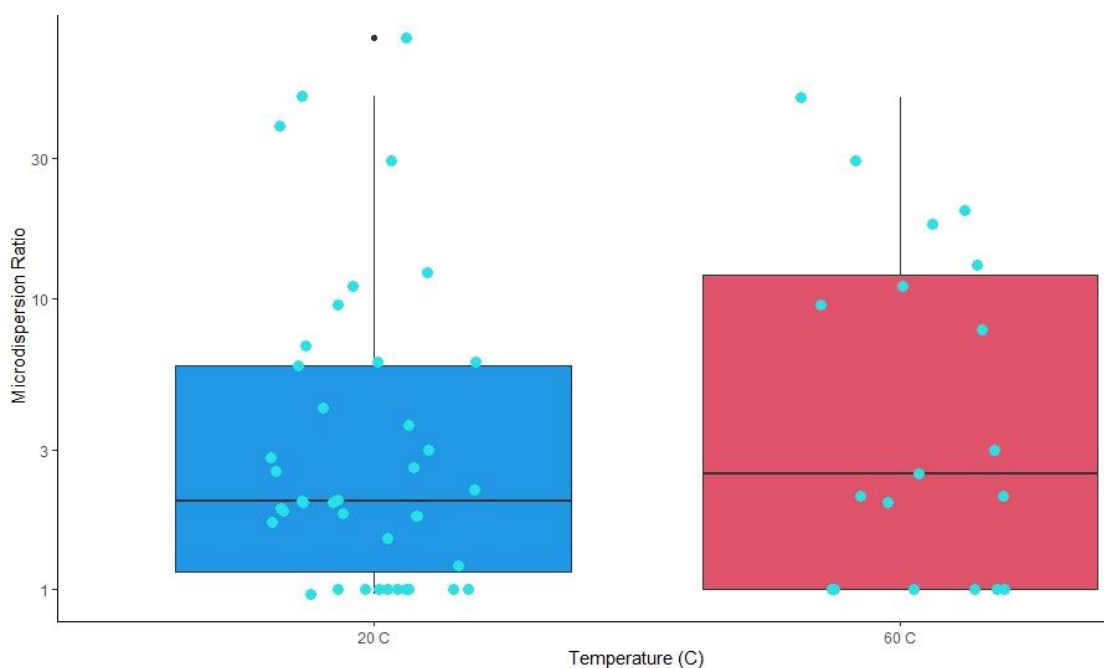


Figure 22 – The boxplot of the reported temperature intervals of the reported data.

Figure 23 shows the histogram and the boxplot of the microdispersion ratios, which shows a non-uniform distribution. Most data are in the low range, while only a few values are in the higher range. As the black line inside the boxplot represents, more than 50 percent of the microdispersion ratios are lower than 4, with only a few data points with substantially higher values. This high range of values can be because of a considerably high error bar. The same is true for the asphaltene fractions. The majority of asphaltene fractions are less than 1 percent, with only a few outliers with values exceeding 1 up to 18 percent (Figure 24).

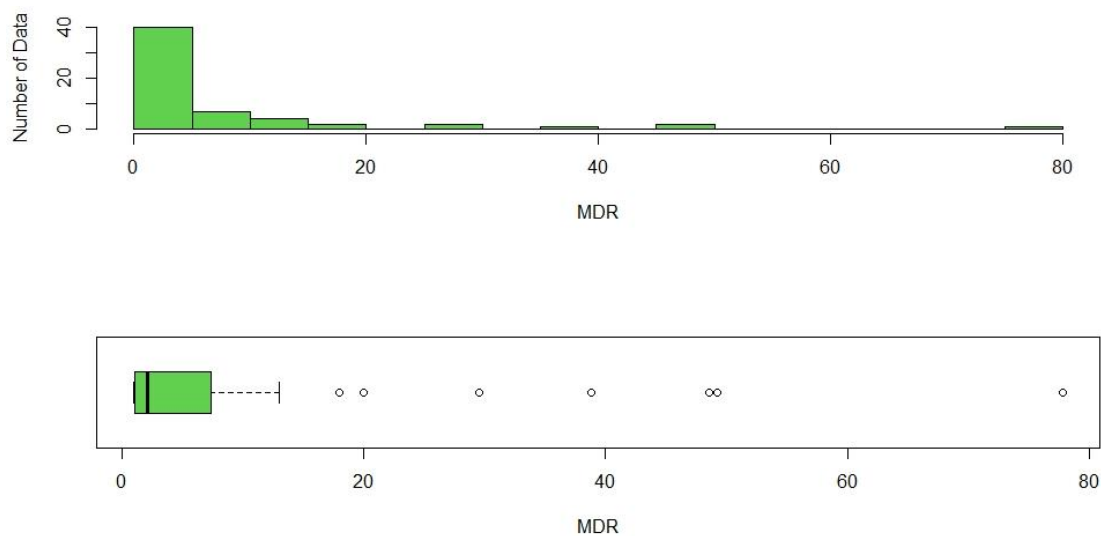


Figure 23 – The histogram and the boxplot of the microdispersion ratio data.

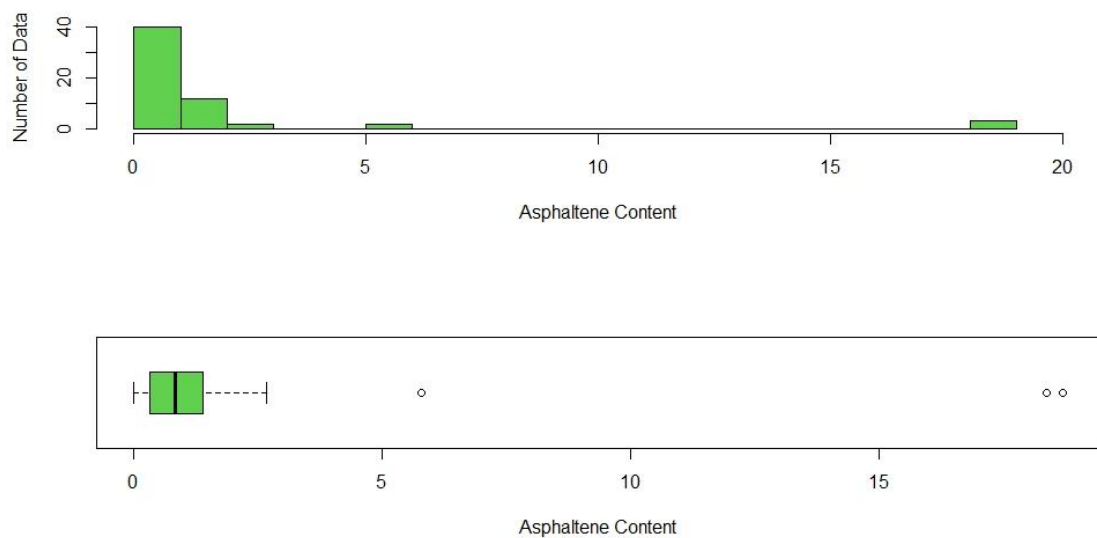


Figure 24 – The histogram and the boxplot of the asphaltene fractions.

The distribution of the saturates and aromatics show a more uniform state (Figures 25 and 26), and the data are reasonably close to a normal distribution.

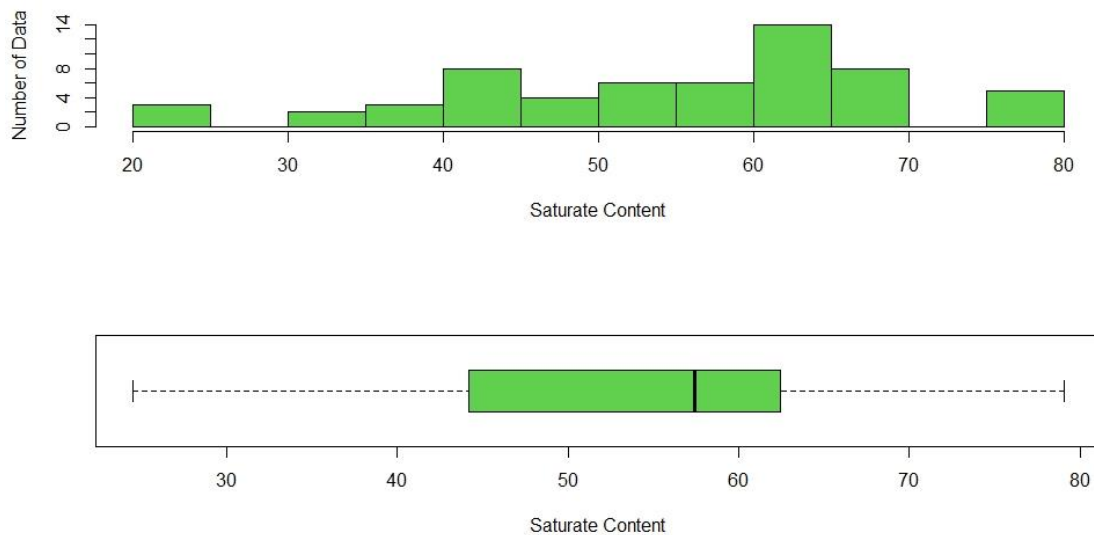


Figure 25 – The histogram and the boxplot of the saturate fractions.

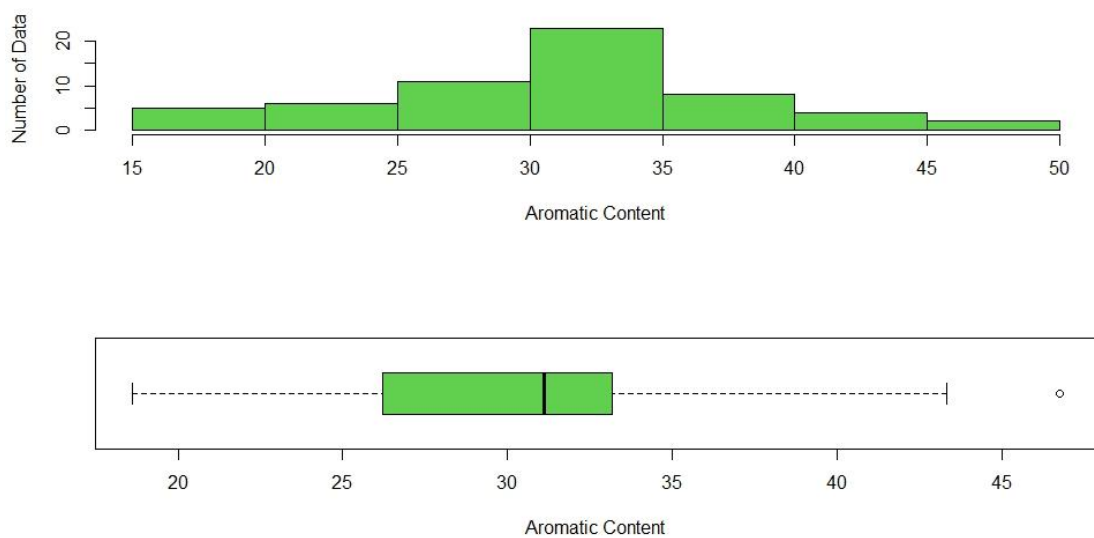


Figure 26 – The histogram and the boxplot of the aromatic fractions.

Resin fractions, which are the last component in the procedure of the SARA determination, also have a slightly non-uniform distribution but not as severe as the one for the asphaltene fractions (Figure 27).

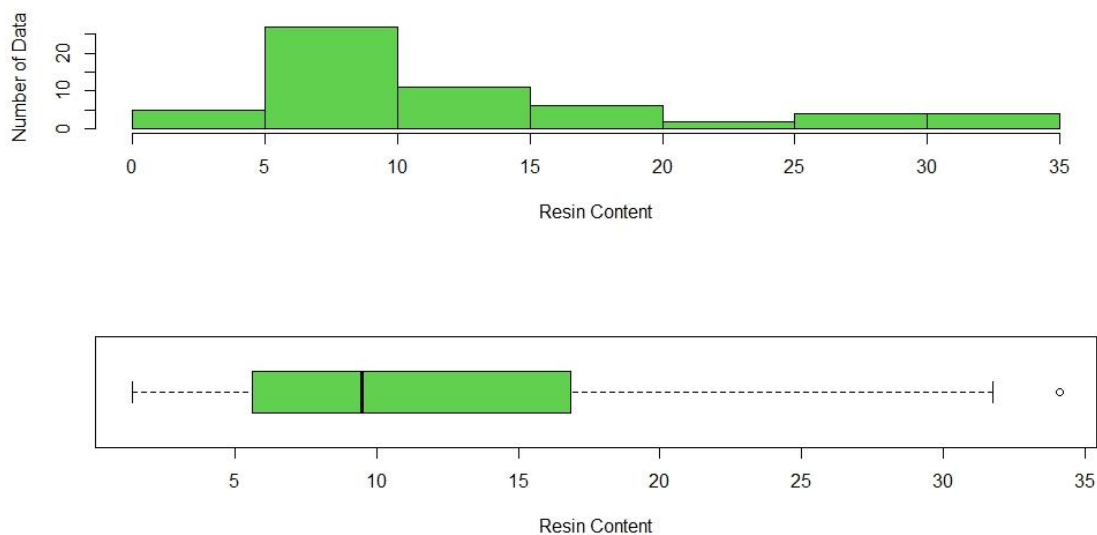


Figure 27 – The histogram and the boxplot of the resin fractions.

The data show a truncated distribution with the majority of values being in the low range and only a few outliers with extremely high values (Figures 28 and 29) about the acidic and basic components of crude oil.

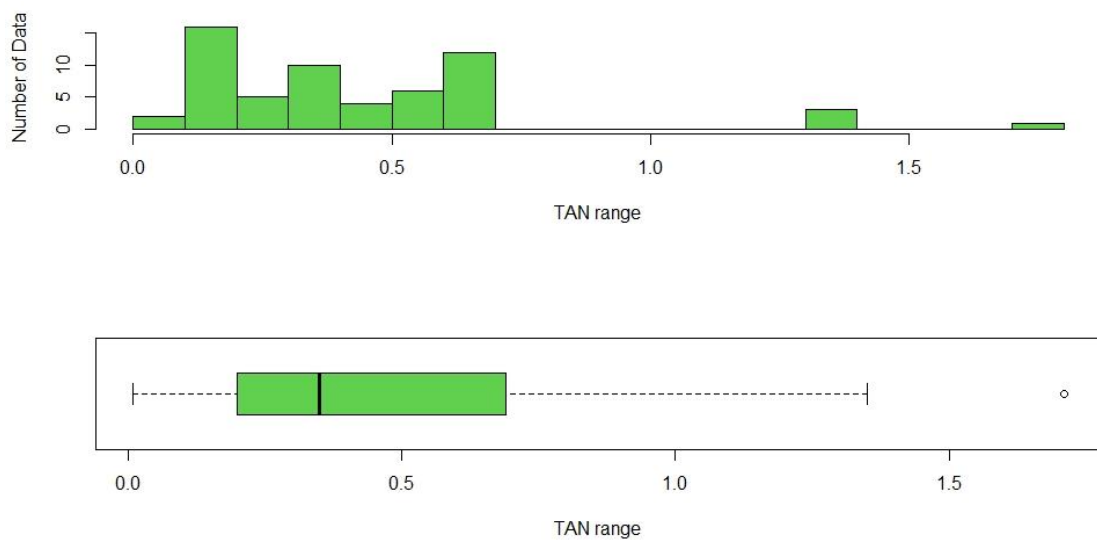


Figure 28 – The histogram and the boxplot of TAN.

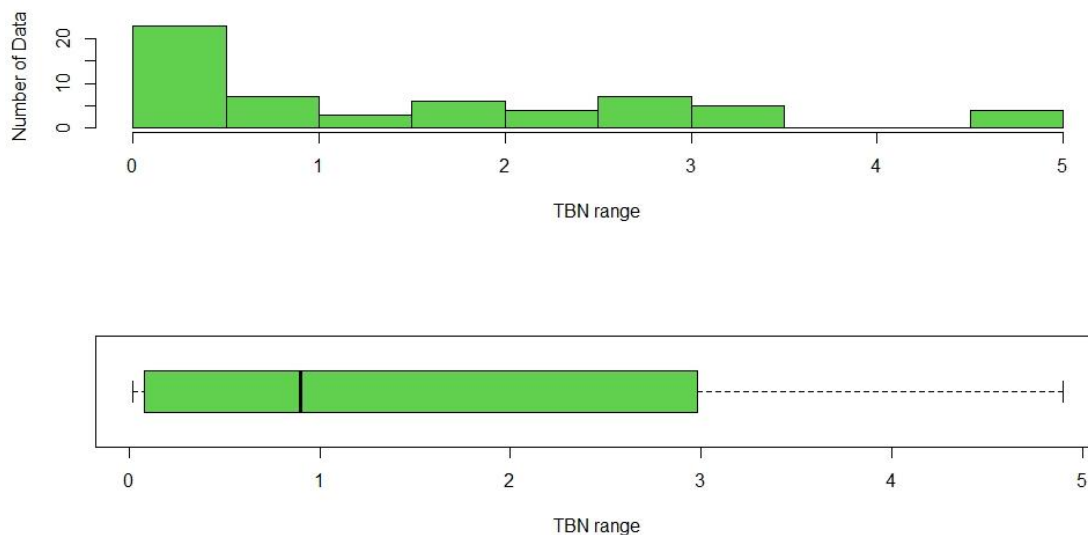


Figure 29 – The histogram and the boxplot of TBN.

From the SARA components of crude oil, CII (Colloidal instability index) and As/R (Asphaltene/Resin) ratio were calculated. As can be seen in Figure 30, the CII values for the data show a truncated distribution.

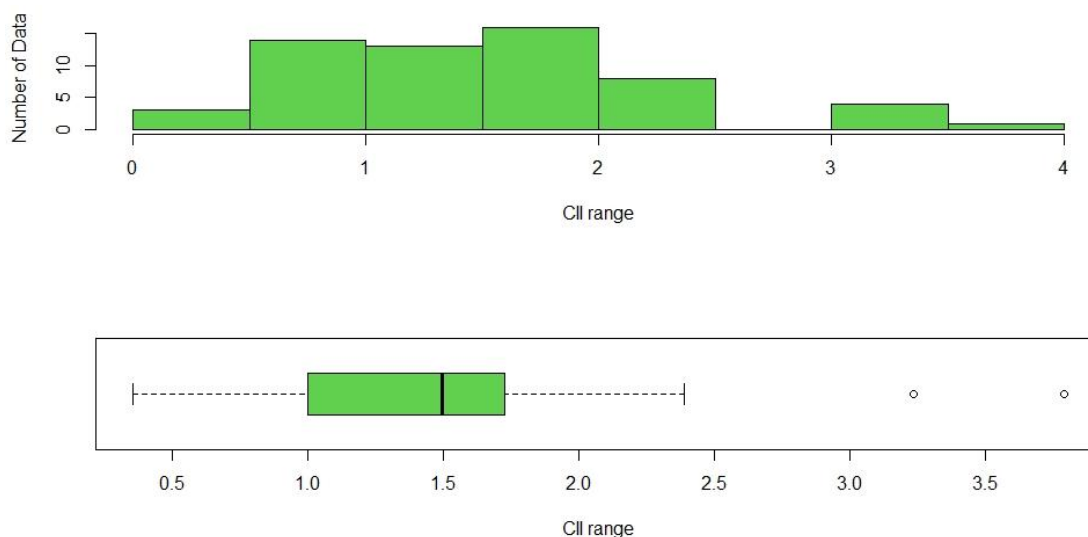


Figure 30 – The histogram and the boxplot of the CII index.

CII shows the degree of asphaltene instability, and the higher it is, the higher is the instability of asphaltene molecules. CII greater than or equal to 0.9 means that the asphaltene molecules tend to be precipitate, but when CII is less than or equal to 0.7, asphaltene stability is certain (Sulaimon et al. 2020). Table 1 shows the number of data in the stable and unstable range.

Among the 59 data sets from the literature, 46 data sets have CII values higher than 0.9, 8 data sets with CII values less than 0.7, and 5 data sets in between.

Table 1 – The range of CII values for the collected data from the literature.

	Greater than or equal to 0.9 (Unstable)	Between 0.9 and 0.7	Less than or equal to 0.7 (Stable)
Number of Data sets	46	5	8

On the other hand, the asphaltene over resin (As/R) ratio is another index reported for assessing the instability of asphaltene molecules within crude oils. As shown in Figure 31, the As/R ratio for the whole data set shows a truncated distribution.

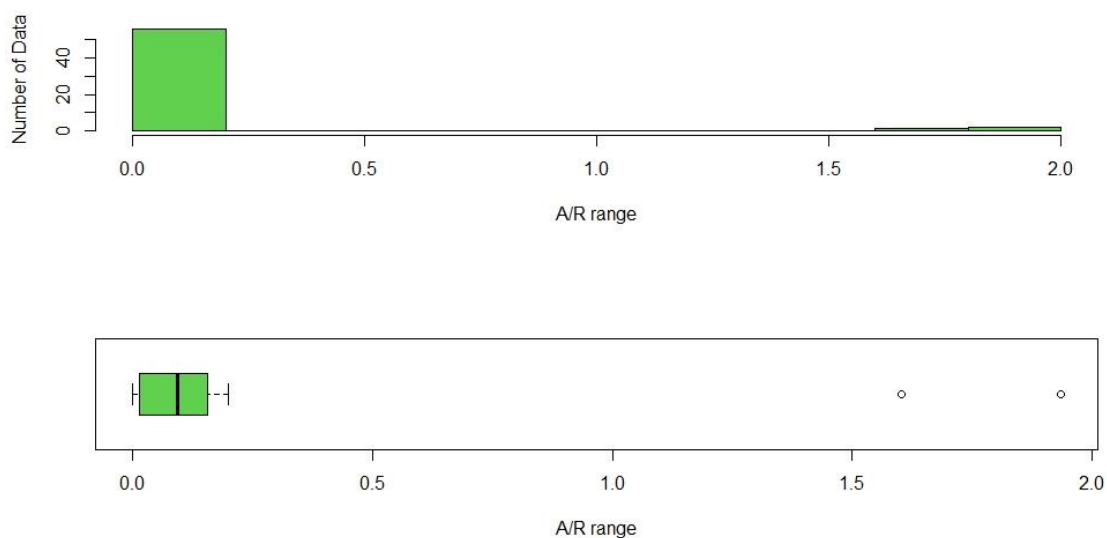


Figure 31 – The histogram and the boxplot of the Asphaltene/Resin ratio.

The higher the As/R ratio, the more likely will the asphaltene precipitation occur. Specifically, if the As/R ratio is less than 0.35, the crude oil is considered stable (Sulaimon et al., 2020). Table 2 shows the number of data with As/R ratio values greater and less than 0.35. Among the 59 data sets from the literature, 56 data sets have As/R values less than 0.35, while 3 data sets have As/R ratio values higher than 0.35.

Table 2 – The range of As/R ratio values for the collected data from the literature.

	Greater than 0.35	Less than 0.35
Number of Data sets	3	56

Regarding the brine properties, generally, the microdispersion ratio increases with decreasing the total brine’s salinity, as shown in Figure 32.

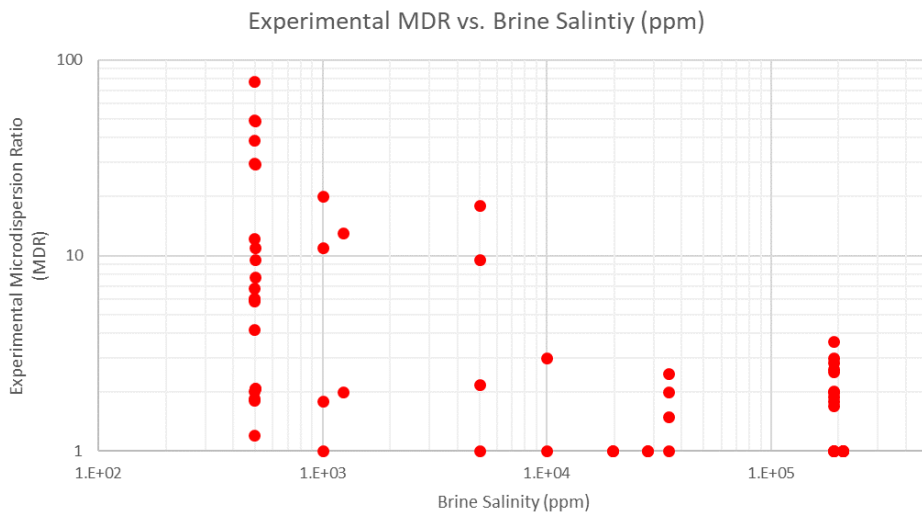


Figure 32 – The plot of the microdispersion ratio values Vs. Brine’s salinity in ppm.

After analysis of the distribution of each property, a machine learning algorithm is conducted to derive a relationship between the significance of microdispersion formation and the crucial crude oil and brine properties.

The machine learning algorithm does the following:

- Defining the simplest model (m0) contains none of the variables to find the best intercept.
- Defining the best model with the compulsory condition to contain all the variables (m.all).
- Eliminating or adding each variable at each step with different approaching methods (Backward, Forward)
- The backward algorithm starts with m.all, and at each step, eliminates one variable. Then, depending on the effects on the GOF (goodness of fit), the algorithm decides to keep or eliminate the variable.
- The Forward method does the same as the backward method but starting from m0.

The goodness of fit of the model is based on different statistical parameters such as:

- AIC (Akaike Information Criterion)
- BIC (Bayesian Information Criterion)

Both parameters are used to assess the model's fit while penalizing for the number of estimated parameters. Thus, the lower the BIC and AIC, the better is the model. A Logistic model is used to model the probability of a particular class or event existing, such as pass/fail, win/lose, alive/dead, or healthy/sick.

The formulation of the logistic model for a single variable system is given in Equation 11:

$$\frac{\pi(x)}{1 - \pi(x)} = \exp(\alpha + \beta x) = e^\alpha e^{\beta x} \quad \text{Eq. 11}$$

The general formulation of a logistic model is given in Equation 12.:

$$\log\left(\frac{p(X)}{1 - p(X)}\right) = \beta_0 + \beta_1 X_1 + \beta_2 X_2 + \dots + \beta_p X_p \quad \text{Eq. 12}$$

Where α and β are coefficients, X_i the independent variable, and $p(X)$ is the probability of the categorized variable X (MDR) to belong to either class. Figure 33 shows an example of a logistic model for the case of having diabetes vs. BMI (Body Mass Index):

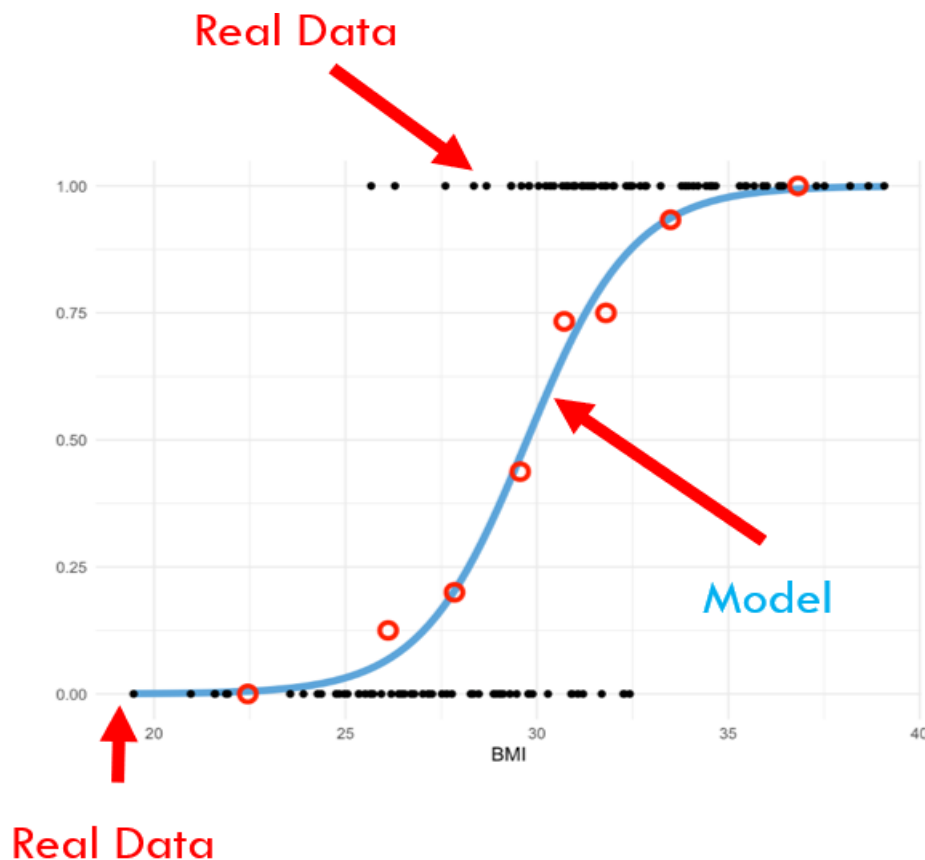


Figure 33 – The example of a logistic model.

By defining a specific cut value for the probability, we can divide the modeled results into two categories. The value of 0.5 is often used for the cut value. Therefore, if the model value, which is the probability of success, will be higher than 0.5, the prediction is class 1; otherwise, class 0 or failure. Figure 34 shows the same example of the probability of having the illness versus BMI with the cut value of 0.5.

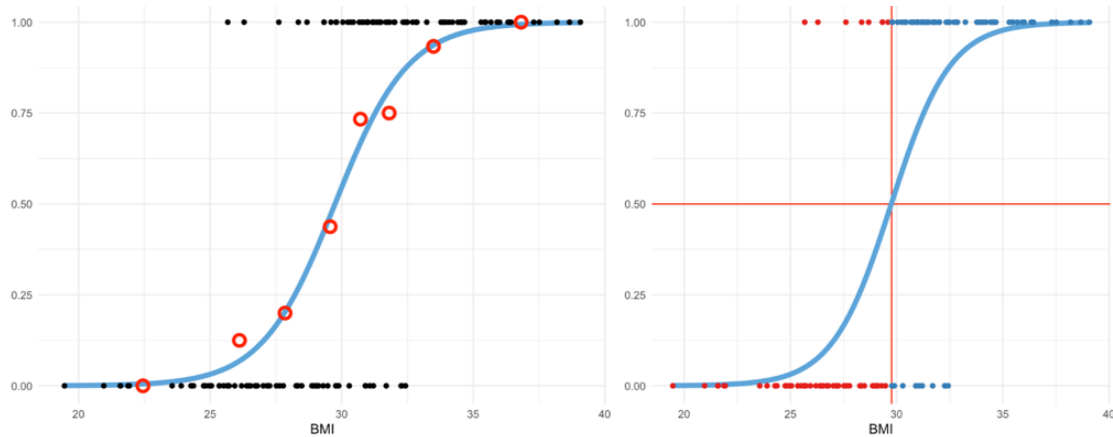


Figure 34 – The example of having the illness vs. BMI with the cut value of 0.5, the red dots in the right plot: the predicted healthy, the blue dots in the right plot: the predicted sick.

The logistic regression in the next step is applied by assuming that the system can form water in oil microdispersions if MDR is greater than 4, as Masalmeh et al. (2019) suggested.

By categorizing the MDR values into two categories:

- Less than 4: category 0, impotent to form significant water in oil microdispersions.
- Greater than 4: category 1, potent to form significant water in oil microdispersions.

4.2 Experimental methodology

In this section, the experimental methodology to investigate the interactions of crude oil and brine is described. In addition, some laboratory measurements have been conducted to characterize their physical properties.

4.2.1 SARA Measurements

Oil samples were directly diluted with the hexane: DCM (Dichloromethane) mixture in the ratio of 80:1, followed by a centrifuge to separate precipitated asphaltene molecules. The asphaltenes were then discarded, and the maltenes (hexane-soluble organic matter) were preserved. Next, the hexane-soluble fractions were separated into resin components, saturates, and aromatics

using medium pressure liquid chromatography (MPLC). A Köhnen-Willsch MPLC instrument was used to separate fractions of the maltenes (Radke, et al. 1980). Aliphatic and aromatic fractions were then returned to the Zymark TurboVap 500 closed cell concentrator and evaporated to a concentration of approximately 1 ml. These reduced fractions were then transferred into small bottles (for analysis with the gas chromatograph) and placed on the heating plate for about 12-24 hours.

The now dried aliphatic and aromatics extracts were weighed on a scale, and their weights were recorded.

4.2.2 De-asphalting Procedure

Asphaltene separation was done by adding n-pentane to crude oil at a volume ratio of 40 to 1. The mixture was then filtered using filter paper to separate deposited asphaltenes from oil.

4.2.3 Crude Oil Viscosity Measurement

Crude oil viscosities have been measured using Anton Paar Rheometer. The applied shear stress is measured by applying different shear rates (from 10 – 500 s⁻¹) at a constant temperature of 22 degrees Celsius. The fraction of shear stress over shear rate gives then the dynamic viscosities of the sample.

4.2.4 Fluid density measurement

Crude oil and synthetic brine densities are measured using Anton Paar density meter DMA 35. The DMA 35 density meter measures the density of liquids by the oscillating U-tube method.

4.2.5 Dilatational Interfacial Viscoelasticity Measurements via Spinning Drop Tensiometer

Dilatational interfacial rheology was evaluated by measuring the interfacial viscoelasticity (IFVE) using spinning drop tensiometer SVT20 from Data Physics instrumental company (Figure 35). It consists of a measuring cell where the capillary tube is located. The capillary tube can be spun up to a maximum rotational speed of 10000 rpm in steps of 100 rpm. Furthermore, the device is equipped with a camera with an optical zoom lens that allows magnifications between 0.7 to 4.0x, enabling measurements of droplets of different sizes.

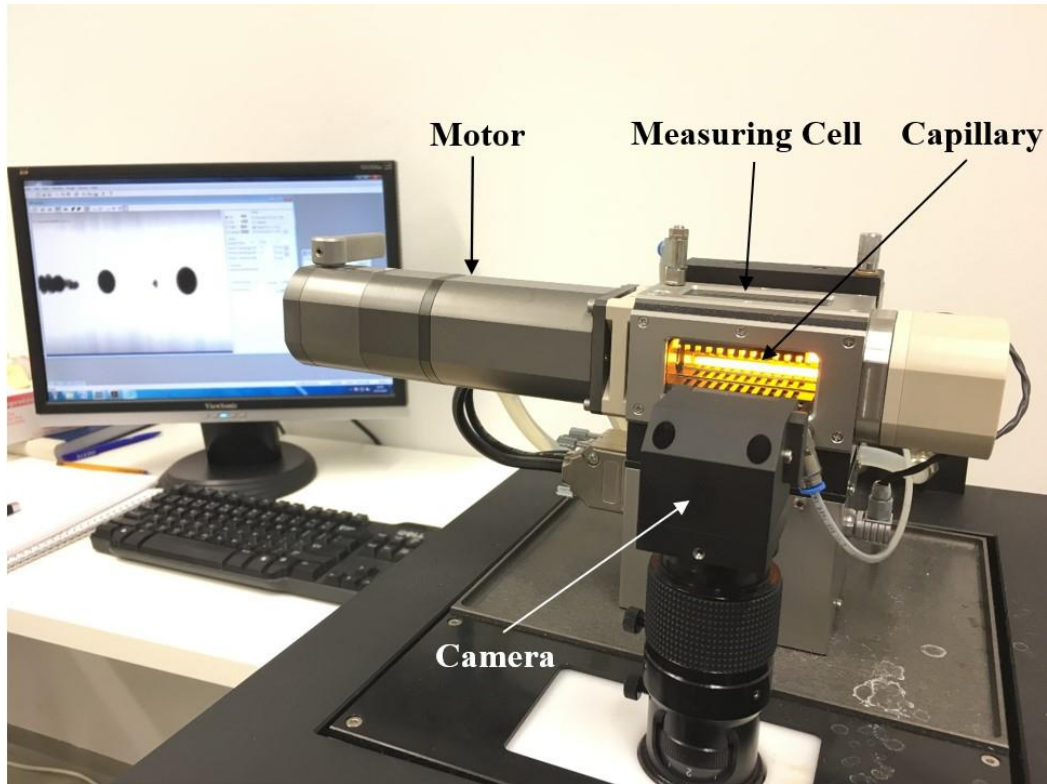


Figure 35 – The Spinning Drop Device for the measurements of interfacial viscoelasticity (Arnold, 2018).

During the experiments, the two immiscible fluids are contained within a fast exchange capillary tube (see Figure 36) located inside the measuring cell. The capillary tube can withstand the same temperature range as the measuring device. It has an inner diameter of 4.0 mm and a visible glass window length of 50 mm.

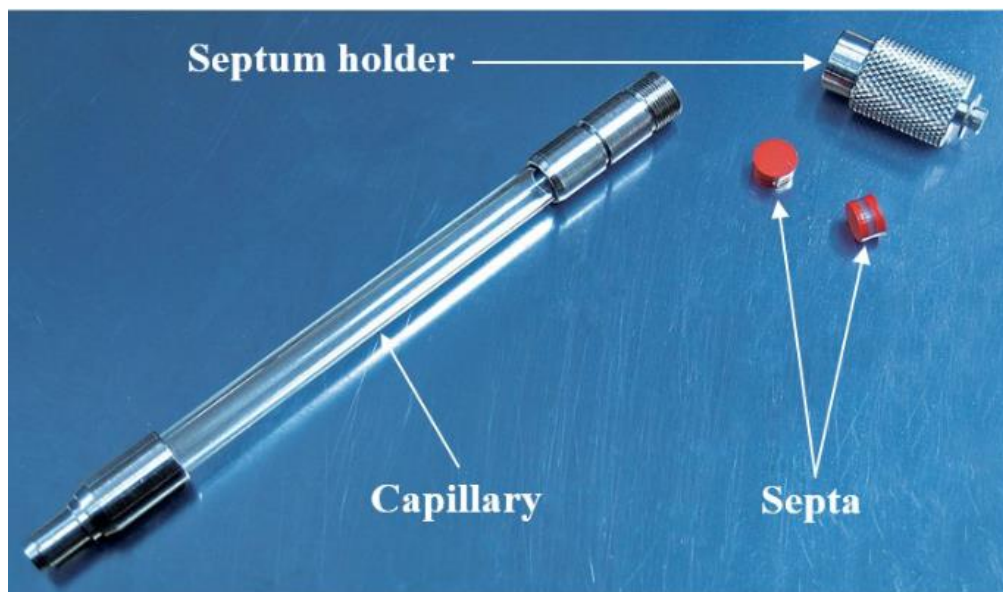


Figure 36 – The capillary tube filled with the two immiscible fluids for viscoelasticity measurements (Arnold, 2018).

The capillary tube was cleaned between each experiment based on the procedure below to ensure having reliable measurements.

- Wash with Decane (95%).
- Fill up with Decane (95%) -> ultrasonic bath: 50°C and 15 minutes.
- Wash with Decane (95%).
- Wash with Acetone.
- Fill up with Acetone -> ultrasonic bath: low temperature and 15 minutes.
- Wash with Acetone.
- Wash with DI-Water (2 times).
- Wash with Hellmanex 2%.
- Fill up with Hellmanex -> ultrasonic bath: 30-35°C and 20 minutes.
- Wash with Hellmanex 2%.
- Wash with DI-Water (2 times).
- Fill up with DI-Water -> ultrasonic bath: 60°C and 15 minutes.
- Wash with DI-Water (2 times).
- Wash with Acetone.
- Let it dry.

The device calculates the IFVE from the oscillating interfacial signals obtained from the sinusoidal oscillation of the rotational speed. Sinusoidal oscillations of the drop surface area result in periodic expansion and compression of the adsorption layer at the interface, and the device simultaneously measures the IFT. Thus, the dynamic rheological properties of the adsorbed layers resulting from the area variation can be observed.

It was noticed that IFT stabilizes after around 2 hours. After IFT reaches a plateau, sinusoidal oscillation of the rotational speed is then applied for 3 hours. All experiments were done with a frequency of 0.1 Hz, rotational speed of 9000 rpm, and an amplitude of 200 rpm.

Figure 37 depicts one of the measurements, precisely the experiment of crude oil 16th and distilled water, representing the sinusoidal oscillations of the interfacial tension and the droplet surface area for the interval of 30 seconds. Since the frequency of the oscillations has been set to 0.1 Hz, a minimum of the full period of the oscillations should be considered, i.e., 10 seconds. Therefore, as shown in Figure 37, the phase angle of 28.68 degrees will be derived from the device.

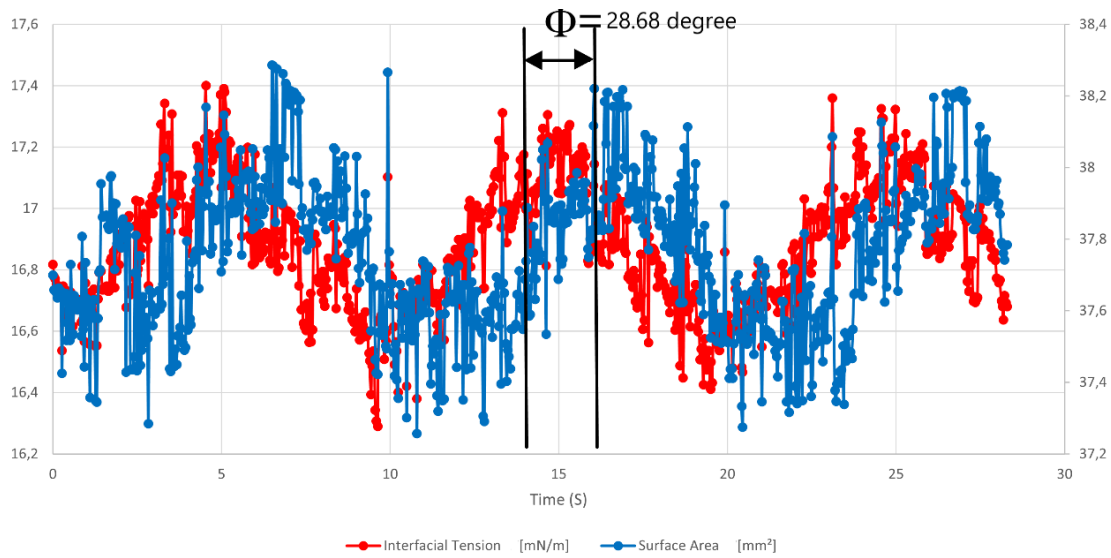


Figure 37 – The signal of the interfacial tension and the surface area with a phase angle of 28.68 degrees for the experiment of crude oil 16th and distilled water.

The viscoelastic modulus can then be calculated using Equation 7, which requires the amplitudes of the interfacial tension, i.e., $\tilde{\gamma} = 0.41$ mN/m (Figure 38) and surface area, i.e., $\tilde{A} = 0.65$ mm² (Figure 39) as well as the median of the surface area signal, i.e., $A_0 = 37.77$ mm² (Figure 39).

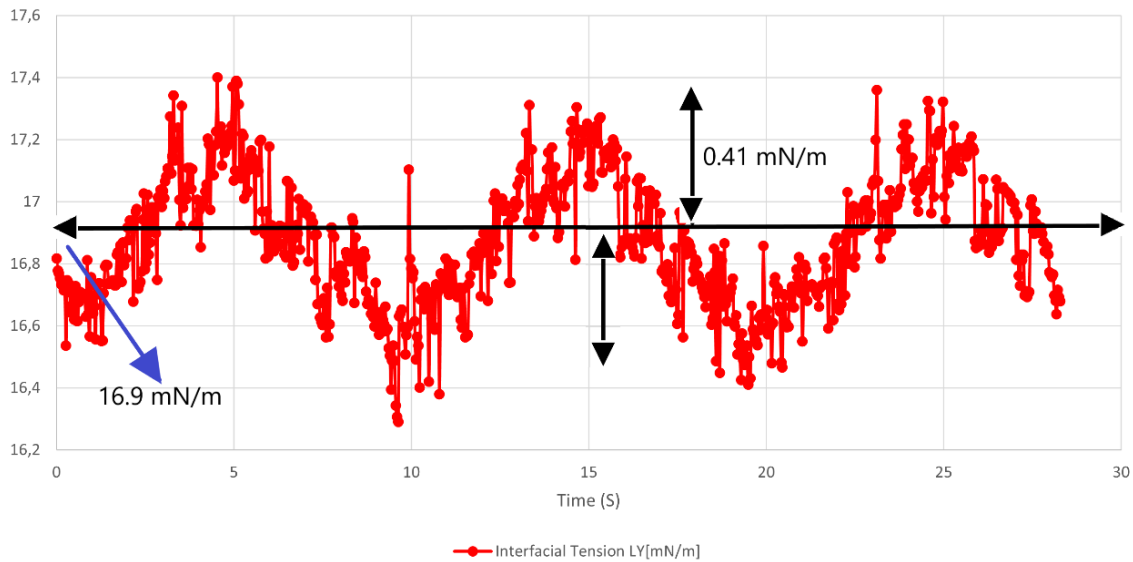


Figure 38 – The example of the signal of the interfacial tension with the required parameters for calculating complex modulus for the experiment of crude oil 16th and distilled water.

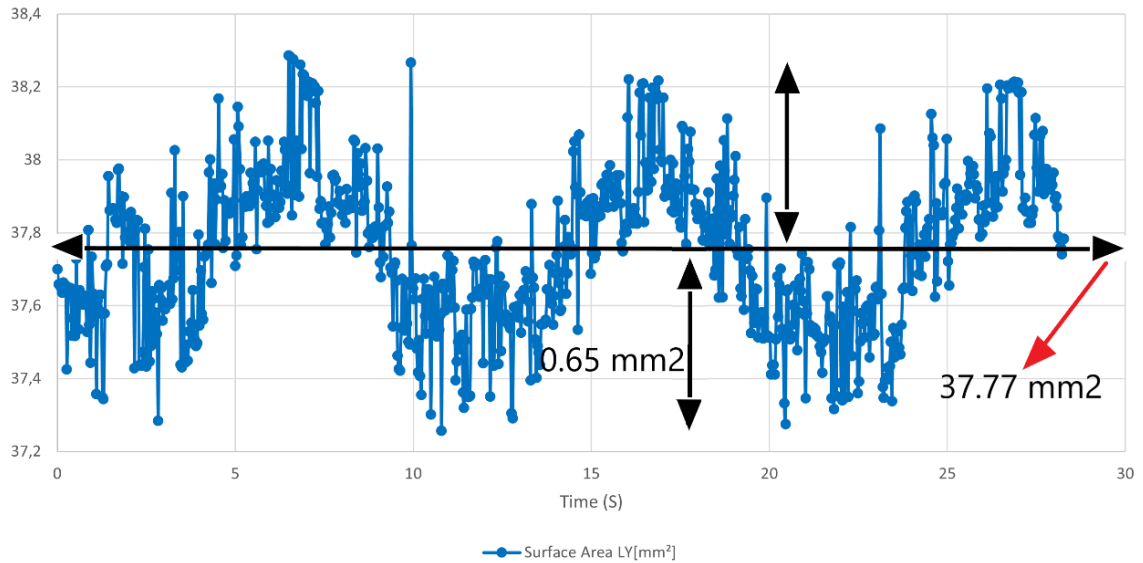


Figure 39 – The example of the signal of the surface area with the required parameters for calculating complex modulus for the experiment of crude oil 16th and distilled water.

By measurement of the required parameters (amplitudes of the interfacial tension and surface area signal, the median of the surface area signal, and the phase shift between interfacial tension and surface area signals), the complex modulus is then calculated with the help of Equation 7:

$$E = \frac{\tilde{\gamma}}{\bar{A}/A_0} \text{EXP}(i\phi) = 23.7 \text{ mN/m}$$

Next is the calculation of the viscous modulus by Equation 13 as:

$$\eta = \frac{E \sin(\phi)}{\omega} \quad \text{Eq. 13}$$

where E is the complex modulus, Φ is the phase shift, and ω is the angular rotational speed equal to $2\pi\nu$ with ν as the frequency of oscillations in Hz.

Therefore, for this example, the viscous or loss modulus will be equal to 11.37 mN/m. Finally, by having the complex and viscous moduli, the elastic modulus, E_0 can be calculated based on Equation 14:

$$E_0 = \sqrt{E^2 - (\omega\eta)^2} \quad \text{Eq. 14}$$

which will be equal to 20.79 mN/m.

Figures 40, 41, and 42 show the complex, elastic, and viscous moduli results, respectively, measured every 15 minutes for 3 hours.

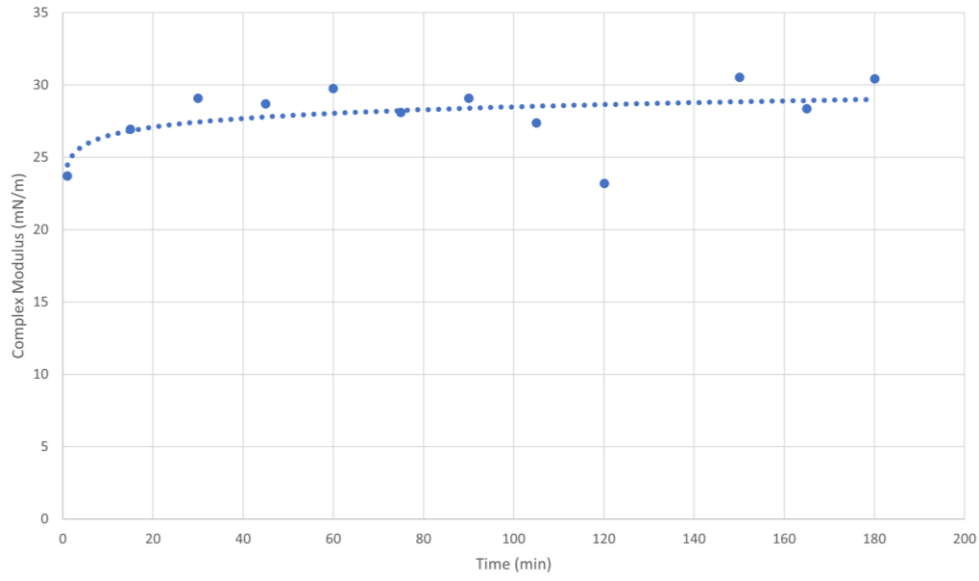


Figure 40 – Complex Modulus vs. Time measured every 15 minutes for 3 hours for the experiment of crude oil 16th and distilled water.

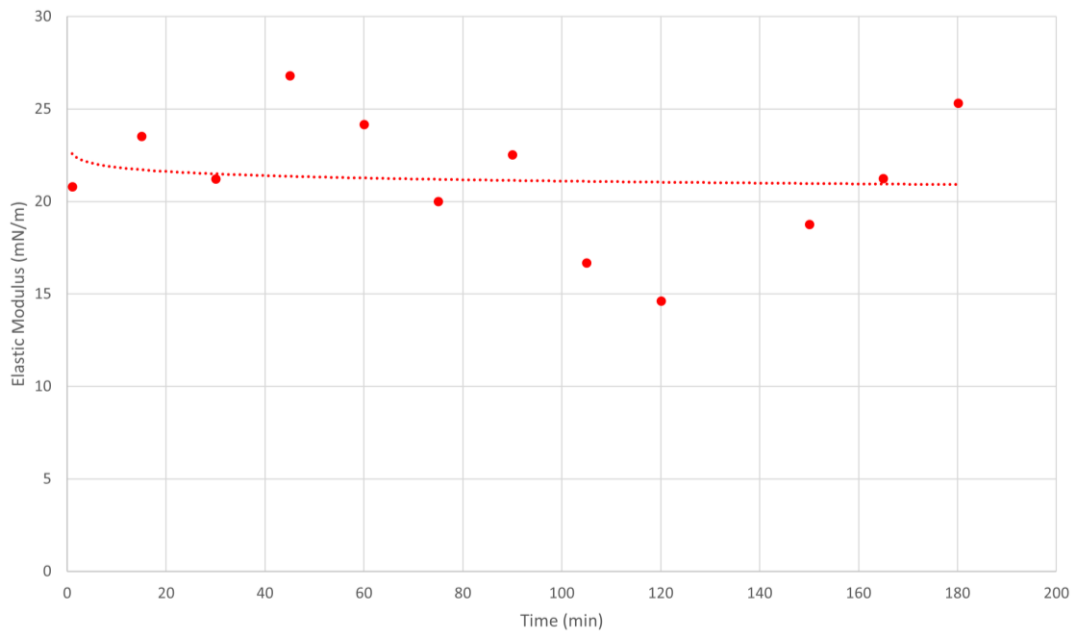


Figure 41 – Elastic Modulus vs. Time measured every 15 minutes for 3 hours for the experiment of crude oil 16th and distilled water.

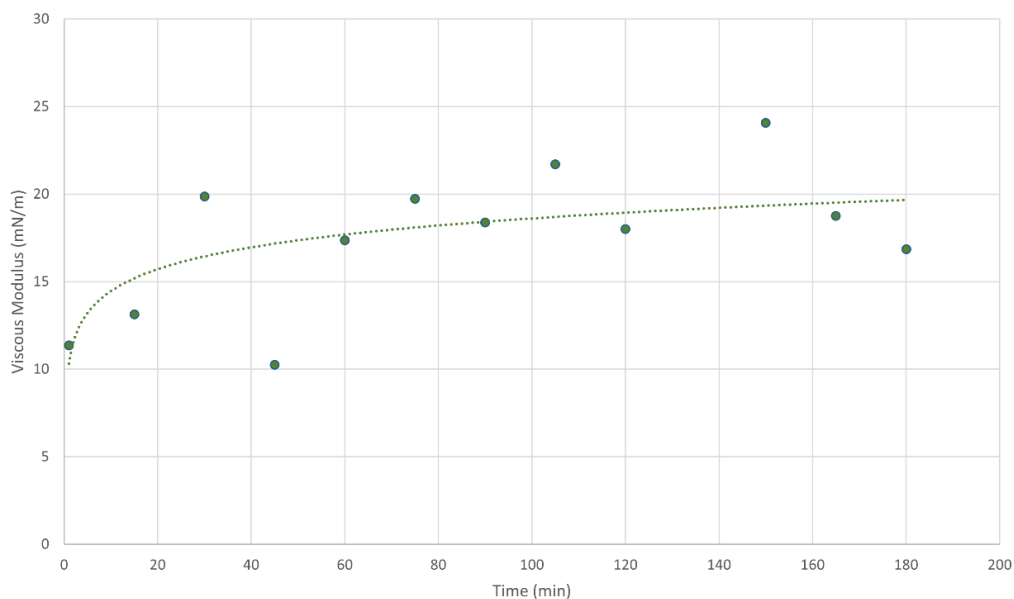


Figure 42 – Viscous Modulus vs. Time measured every 15 minutes for 3 hours for the experiment of crude oil 16th and distilled water.

A critical aspect of the viscoelasticity measurement by the spinning drop technique is that the error bar of the measurements is relatively high. The reason is that since the measurement of the droplet surface area is done through image analysis, depending on the quality of the images and their illumination, the surface area signal can be very noisy. As a result, all three moduli will be calculated with an error span of around 2 mN/m for upper and lower limits. As an example, Figures 43, 44, and 45 show the measured data for complex, elastic, and viscous moduli for the period of 3 hours, including the error bars of the measurements.

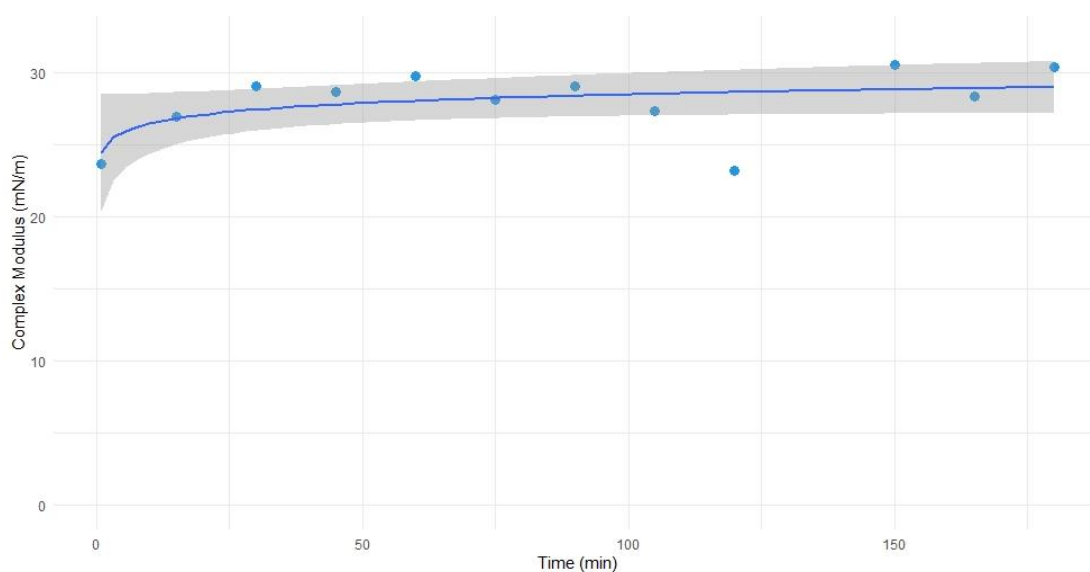


Figure 43 – Representation of the error bar of the measurements (Complex Modulus vs. Time measured every 15 minutes for 3 hours, for the experiment of crude oil 16th and distilled water).

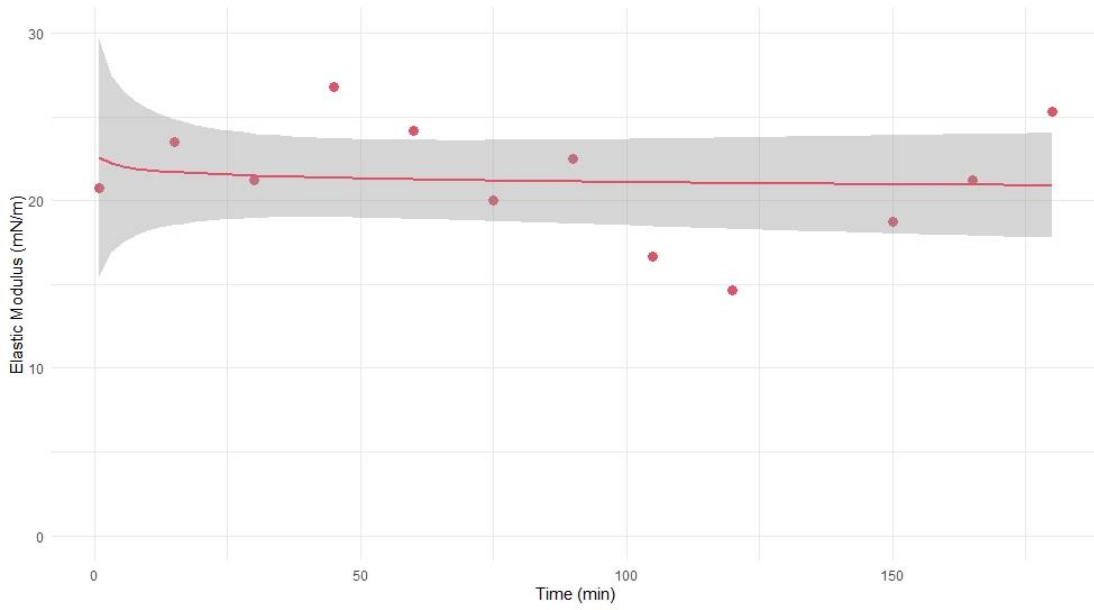


Figure 44 – Representation of the error bar of the measurements (Elastic Modulus vs. Time measured every 15 minutes for 3 hours, for the experiment of crude oil 16th and distilled water).

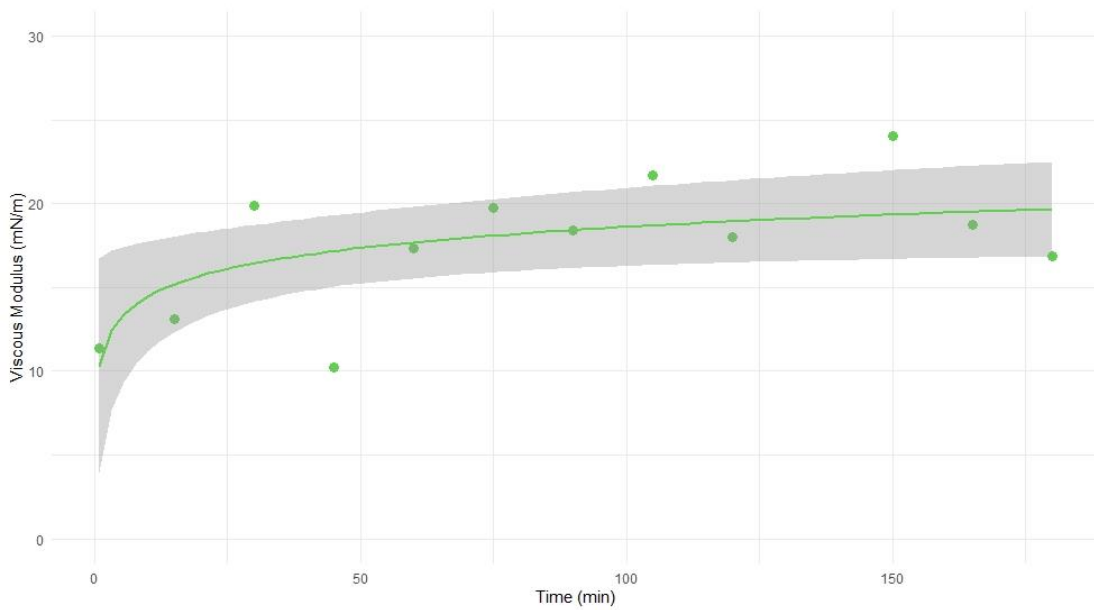


Figure 45 – Representation of the error bar of the measurements (Viscous Modulus vs. Time measured every 15 minutes for 3 hours, for the experiment of crude oil 16th and distilled water).

4.2.1 Microfluidic

The microfluidic experiments are used to study fluid phase distribution and elasticity effect at different flow rates. For our investigation, the results of the microfluid flooding by Kharrat A. (2018) and Schnöpf (2019) were used. The micromodel chip used comprises borosilicate glass with a high-pressure and high-temperature chip holder from stainless steel (Figure 46). The properties of the micromodel used are shown in Table 3.



Figure 46 – The representation of the micromodel chip and the chip holder (Schnöpf, 2019).

Table 3 – The specification of the micromodel and its properties (Schnöpf, 2019)

Porosity [%]	Permeability [D]	PV [μl]	Distance of channel to top surface [μl]	Distance of channel to bottom surface [μl]
57	2.5	2.3	1100	680

Chapter 5

Results and Discussion

5.1 Interfacial dilatational viscoelasticity

Three crude oil samples from Austrian basins (crude 16th, 8th, and Flysch) were used to investigate the interfacial viscoelasticity measurements. In addition, to see the effect of asphaltenes, crude 16th asphaltene was removed. Table 4 depicts their SARA components, their TAN numbers, densities, and viscosities.

Table 4 – Crude oil properties

Crude ID	Saturate	Aromatic	Resin	Asphaltene	TAN	Viscosity (cP) @ 22 °C	Density (g/ml) @ 22 °C
Flysch	67.53	14.64	17.58	0.24	0.34	21.98	0.875
16 th	53.25	18.64	27.8	0.31	1.56	56.35	0.9047
De-asphalted 16 th	57	21.82	21.19	0	1.56	83	0.9215
8 th	54.47	20.81	23.22	1.5	1.96	251.1	0.9306

The viscoelasticity of the oils was measured with distilled water and brines at different salinity levels and ionic concentrations for pure NaCl solutions and the addition of sulfate ions. Table 5 shows the specifications and densities of brines.

Table 5 – Brine properties

Brine specification	Density (g/ml) @ 22 °C
Distilled Water	0.9979
1000 ppm NaCl	0.9982
10000 ppm NaCl	1.0048
40000 ppm NaCl	1.0249
1000 ppm NaCl with 2.5% Na ₂ SO ₄	0.9984
10000 ppm NaCl with 2.5% Na ₂ SO ₄	1.005
40000 ppm NaCl with 2.5% Na ₂ SO ₄	1.025

Figures 47, 48, and 49 show the complex modulus, storage modulus, and viscous modulus for the three oil samples with pure NaCl solutions of different total salinities. Each point in Figures 47 through 52 is obtained by the experimental procedure explained in section 4.2.5. In addition, an example of one test (crude 16th and distilled water) procedure is depicted in Figures 37 through 45 to measure the values of the mechanical dilatational moduli after 3 hours of oscillation and their corresponding error bars.

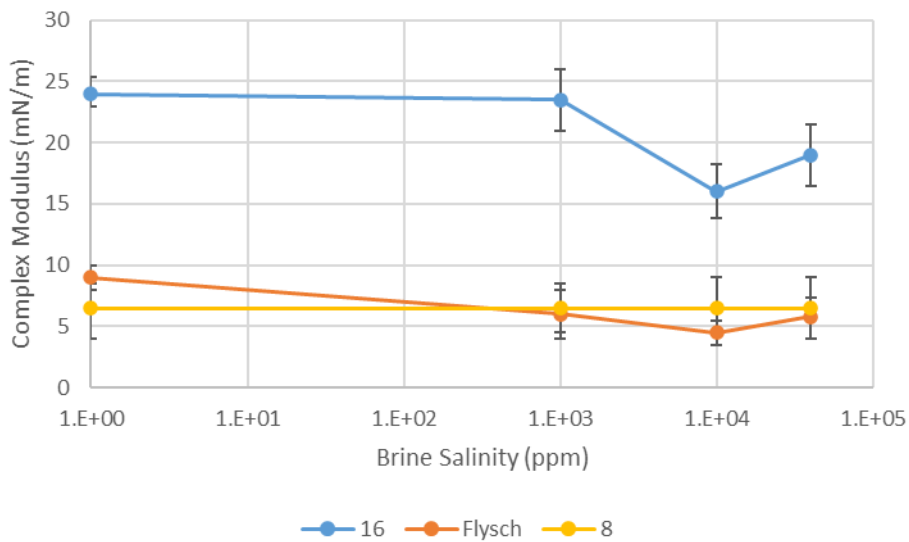


Figure 47 – Complex Modulus vs. Brine Salinity (ppm) for three crude oil samples and pure NaCl solutions.

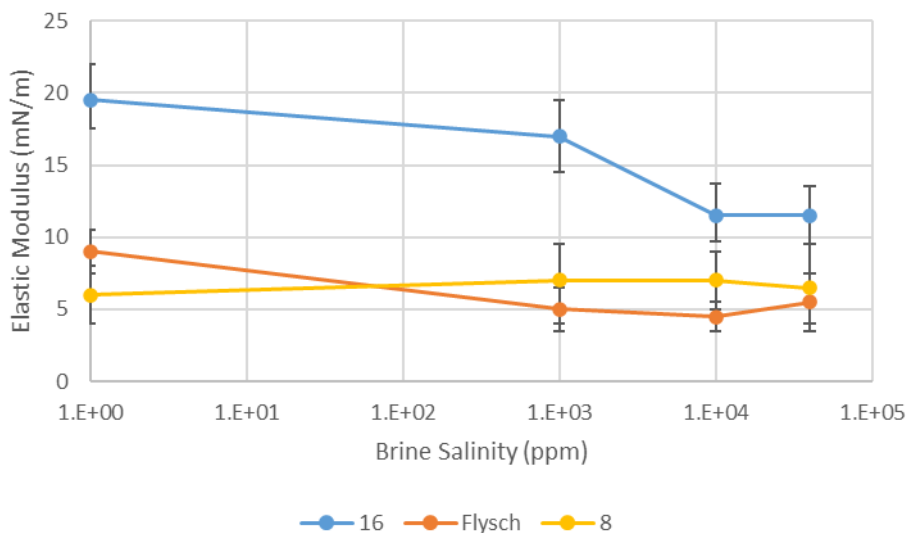


Figure 48 – Elastic Modulus vs. Brine Salinity (ppm) for three crude oil samples and pure NaCl solutions.

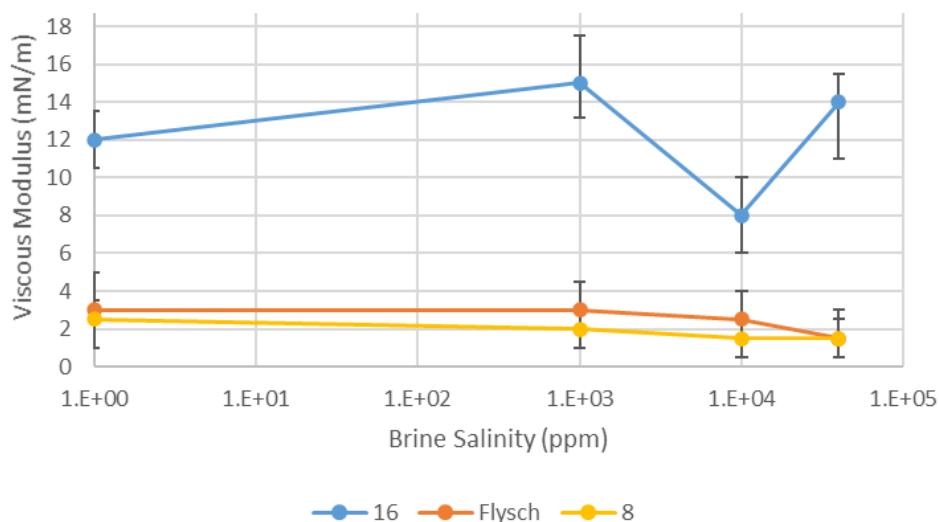


Figure 49 – Viscous Modulus vs. Brine Salinity (ppm) for three crude oil samples and pure NaCl solutions.

Among the three oil samples, crude 16th showed the highest viscoelasticity. Contrarily, crude 8th showed almost insensitivity regarding brine salinity, highlighting the effect of oil viscosity. Despite having a very high TAN number (1.96) due to the high viscosity, i.e., 251 cP, it had the lowest viscoelastic behavior. Crude Flysch with the middle range of viscosity and TAN (0.34 for TAN and 21.98 cP for viscosity) also had very low viscoelasticity but a slight sensitivity to brine salinity (lower than 1000 ppm). However, de-asphalted crude 16th showed the same behavior as the normal crude 16th with a little less viscoelasticity (Figures 50, 51, and 52). This is because, during the procedure of asphaltene separation, heating processes are involved, which leads to evaporation of light components within the crude oil and, as a result, an increase in the viscosity (83 cP compared to 56.35 cP for the normal crude 16th). Thus, this viscosity increase has a much stronger influence on the viscoelastic property of the system rather than the existence of asphaltene molecules.

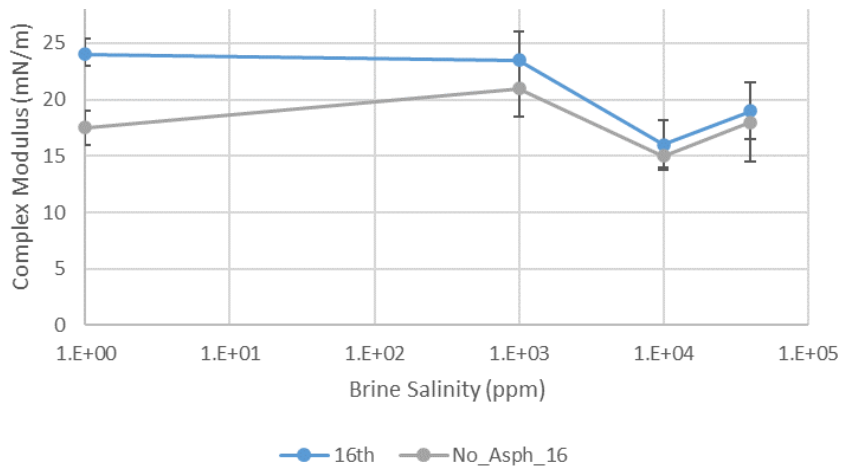


Figure 50 – Complex Modulus vs. Brine salinity (ppm) for normal crude 16th and de-asphalted crude 16th with pure NaCl solutions.

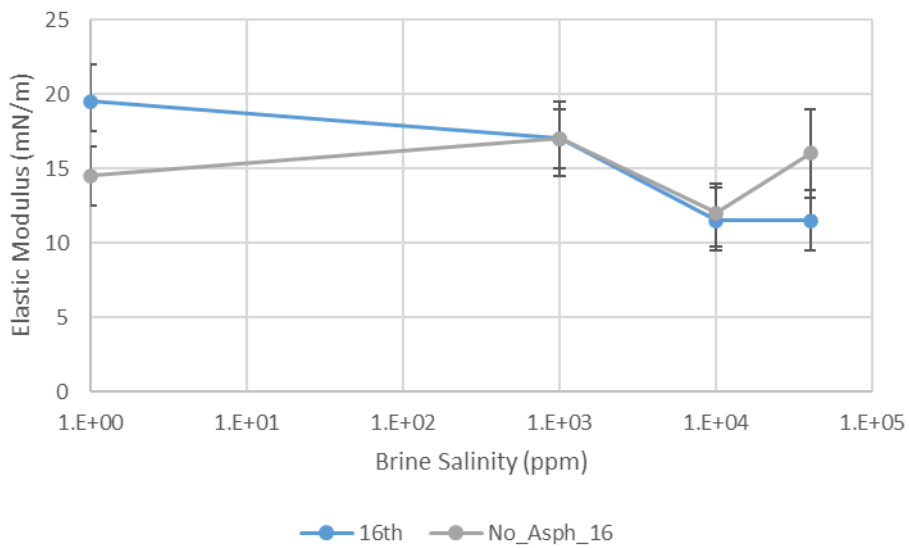


Figure 51 – Elastic Modulus vs. Brine salinity (ppm) for normal crude 16th and de-asphalted crude 16th with pure NaCl solutions.

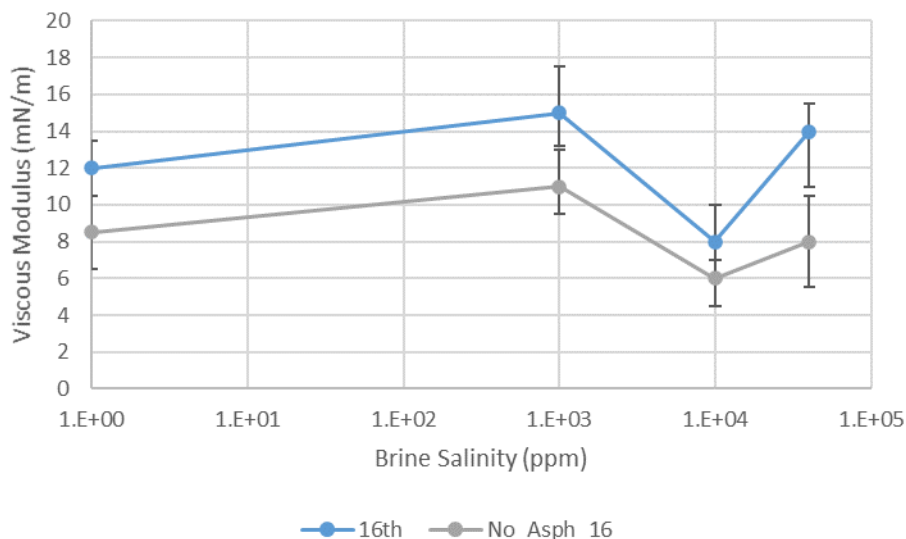


Figure 52 – Viscous Modulus vs. Brine salinity (ppm) for regular crude 16th and de-asphalted crude 16th with pure NaCl solutions.

One key finding of the viscoelasticity measurements is that they prove that the viscoelastic property of crude oil samples is a diffusion-controlled process. Thus, acidic components of crude oil are the conqueror of the competition with asphaltene molecules in the diffusional transport from the bulk of the oil phase to the oil/brine interface.

As can be seen in Figures 53, 54, and 55, there is a positive relationship between the viscoelastic moduli for crude oil and distilled water (to eliminate the effects of brine salinity) and the ratio of the acidic oil components over viscosity. In other words, the existence of acidic components within crude oil is crucial with the condition of low oil viscosity since they have to be transported to the interface and the only transport mechanism is diffusion.

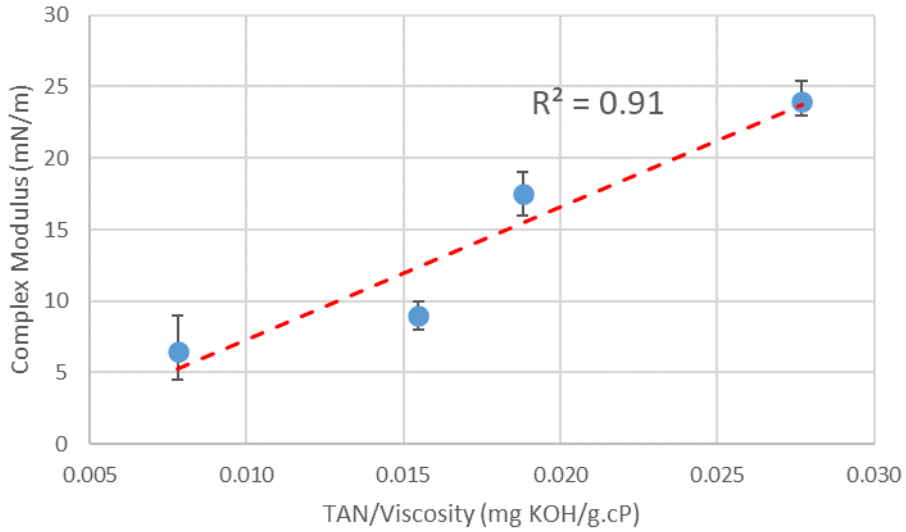


Figure 53 – Complex modulus vs. TAN/Viscosity for crude oil samples and distilled water

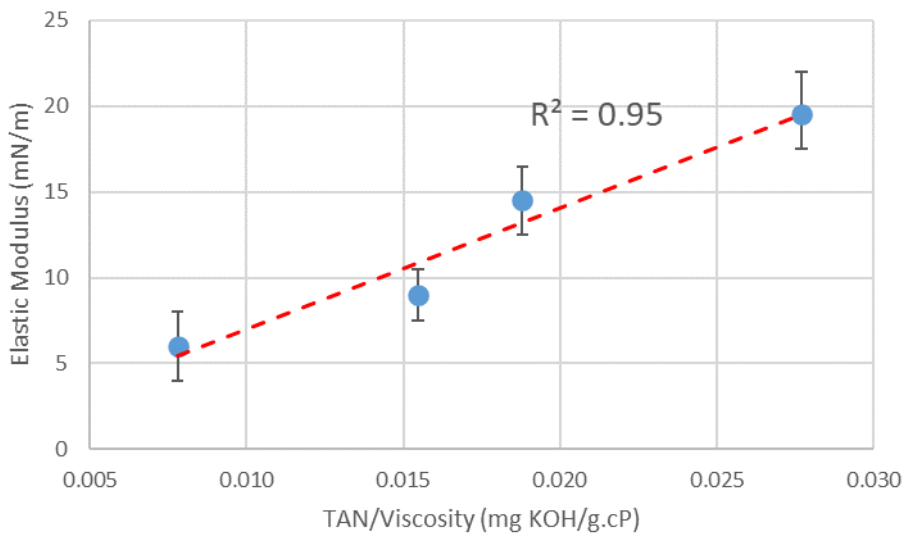


Figure 54 – Elastic modulus vs. TAN/Viscosity for crude oil samples and distilled water

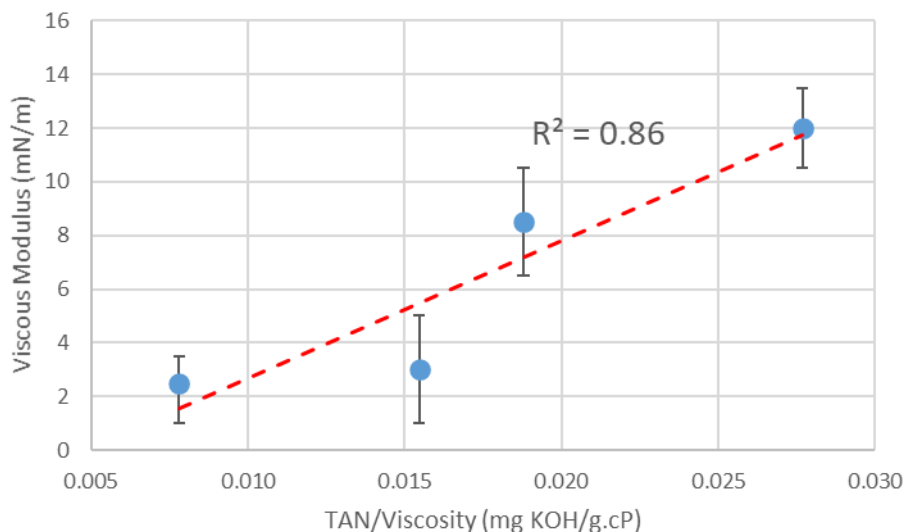


Figure 55 – Viscous modulus vs. TAN/Viscosity for crude oil samples and distilled water.

Furthermore, the ionic content of brine seems to be another parameter that can potentially affect the viscoelastic behavior of the system. As shown in Figures 56, 57, and 58, the addition of 2,5% Na_2SO_4 changed the mechanical viscoelastic moduli of the two crude oil samples (16th and Flysch) non-monotonically. As a result, the viscoelastic moduli experience an increase from high salinity of 40000 ppm up to 10000 ppm. However, an additional decrease in the ionic content of the brine led to the reduction of the viscoelastic moduli.

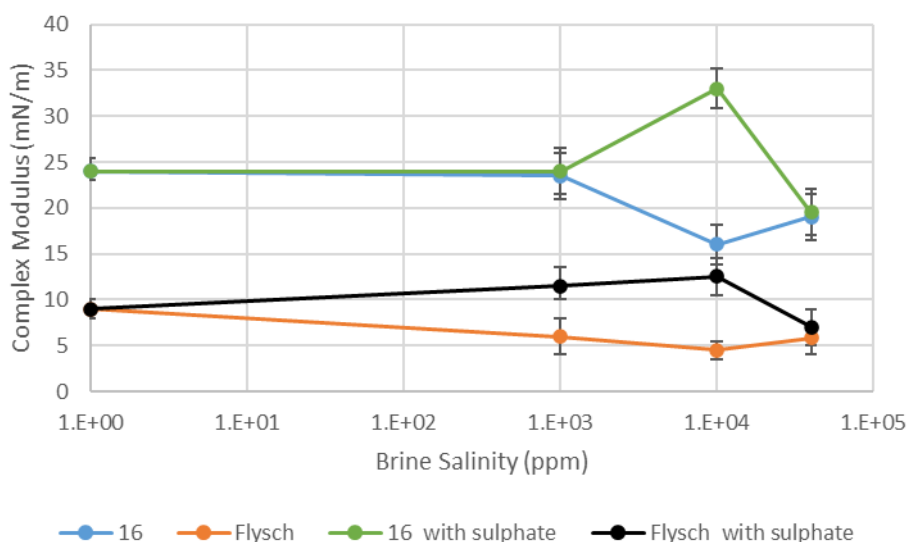


Figure 56 – Complex Modulus vs. Brine salinity (ppm) for crude 16th and Flysch with pure NaCl and pure NaCl solution with 2.5% sodium sulfate solutions.

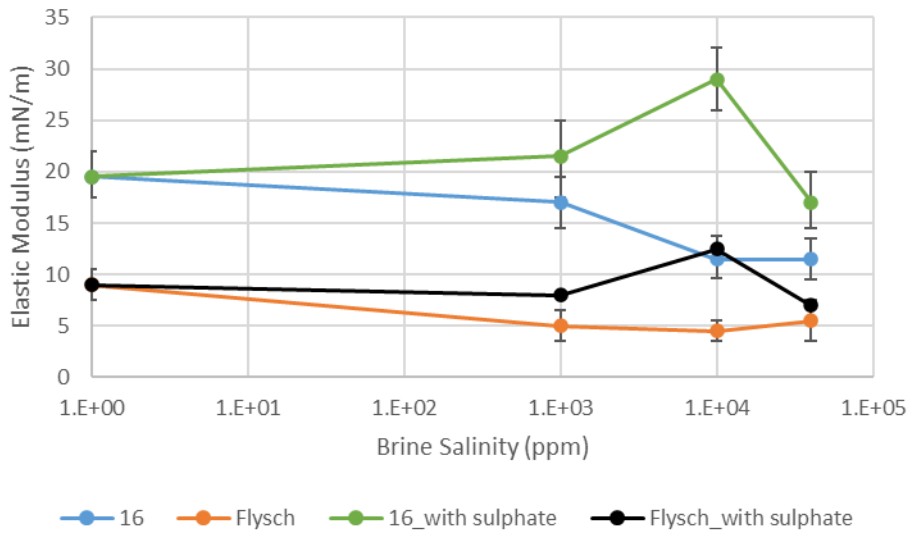


Figure 57 – Elastic Modulus vs. Brine salinity (ppm) for crude 16th and Flysch with pure NaCl and pure NaCl solution with 2.5% sodium sulfate solutions.

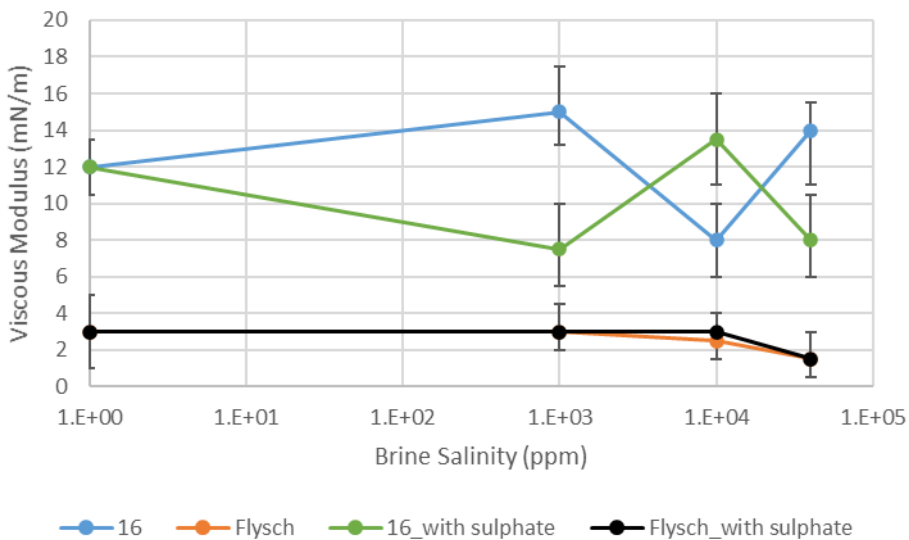


Figure 58 – Viscous Modulus vs. Brine salinity (ppm) for crude 16th and Flysch with pure NaCl and pure NaCl solution with 2.5% sodium sulfate solutions.

In order to detect the most contributing components of crude oil for the evolution of viscoelastic properties of crude oil/water (or in general crude oil/brine) interfaces, the three interfacial mechanical moduli for the measurements of different crude oils against distilled water (to exclude the effects of brine salinity) are plotted against SARA components, as well as the two asphaltene instability indexes, i.e., CII and As/R ratio in Figures 59 through 64.

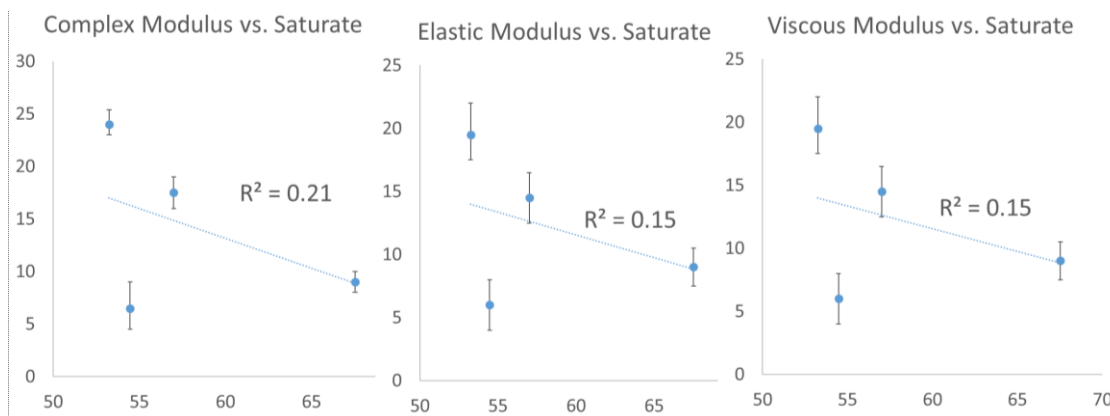


Figure 59 – Complex, Elastic and Viscous moduli vs. Saturate content for crude oil and distilled water.

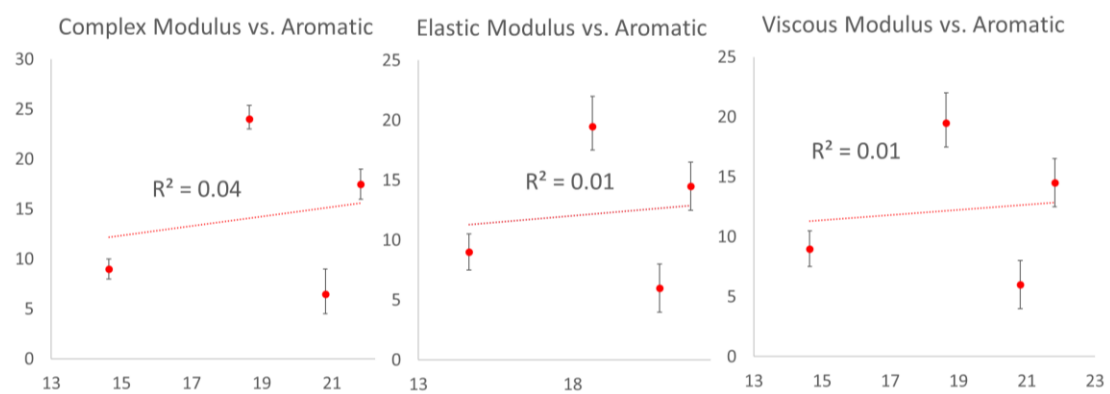


Figure 60 – Complex, Elastic and Viscous moduli vs. Aromatic content for crude oil and distilled water.

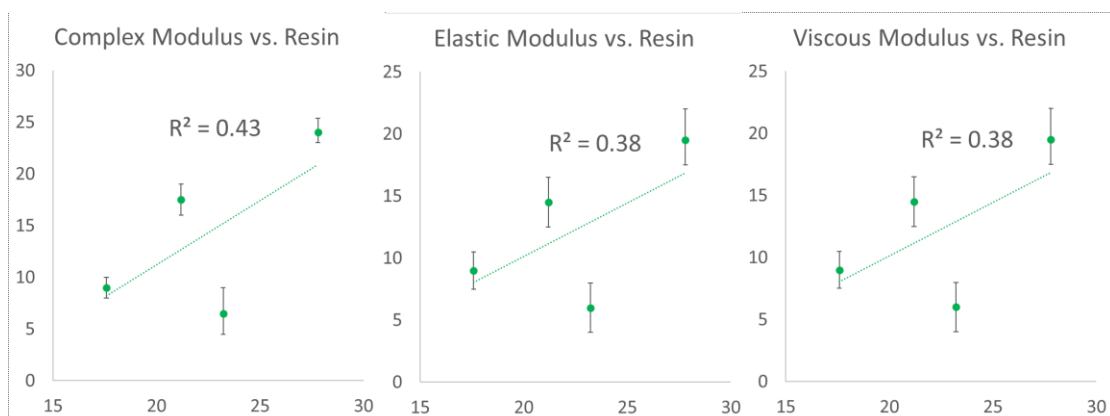


Figure 61 – Complex, Elastic and Viscous moduli vs. Resin content for crude oil and distilled water.

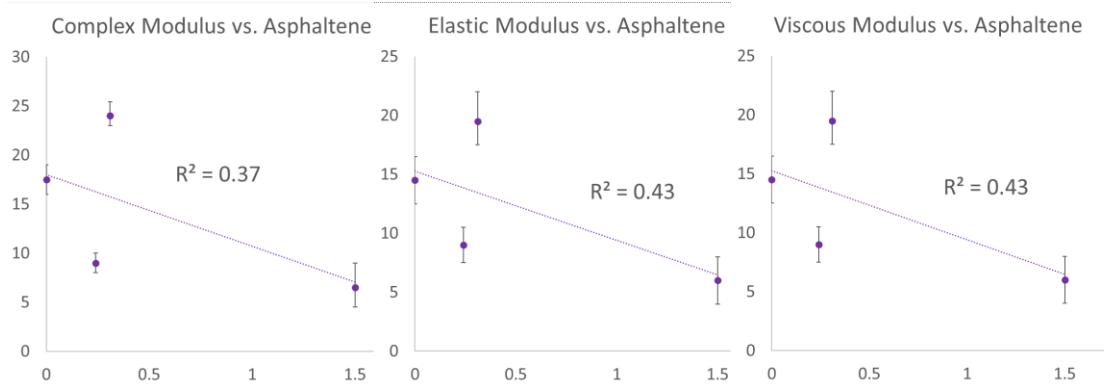


Figure 62 – Complex, Elastic and Viscous moduli vs. Asphaltene content for crude oil and distilled water.

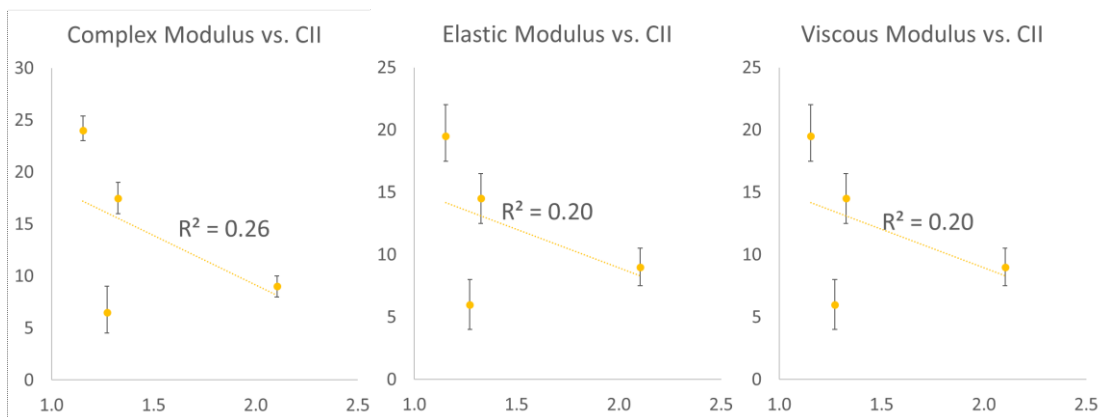


Figure 63 – Complex, Elastic and Viscous moduli vs. CII for crude oil and distilled water.

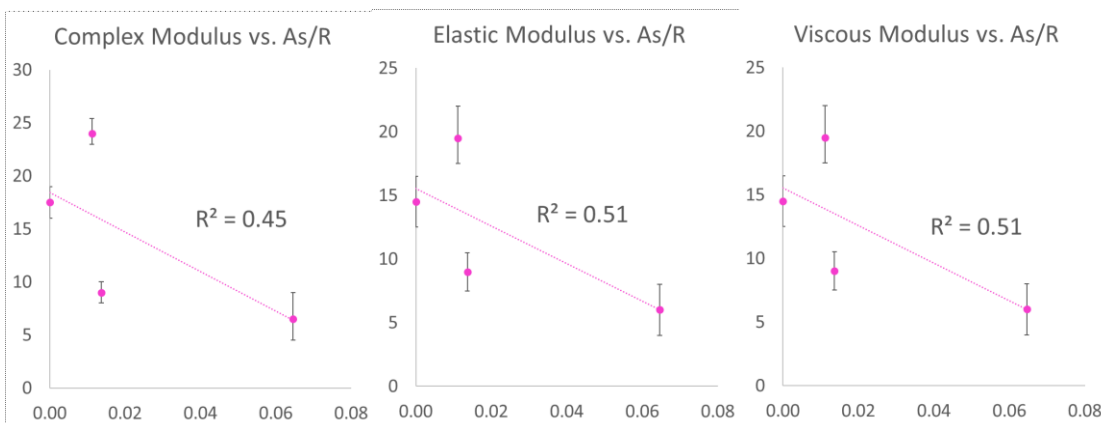


Figure 64 – Complex, Elastic, and Viscous moduli vs. As/R ratio for crude oil and distilled water.

As can be seen, the three mechanical moduli, i.e., complex, elastic, and viscous moduli, illustrated a reasonably fair direct relationship with the resin fractions of crude oil among the four SARA components. In addition, as can be seen in Figure 62, the asphaltene content of

crude oil shows a reverse relationship with the moduli. This can be due to the inability of the type of asphaltenes present in the specific crude oils, have been used. As a result, among the two asphaltene instability indexes, i.e., CII and As/R ratio, the As/R ratio shows a high negative correlation coefficient with the three moduli, as depicted in Figure 64. Thus, having a high positive correlation coefficient concerning resin components and the presence of resin fraction in the denominator of the As/R fraction and the high negative correlation coefficient of moduli with asphaltene content resulted in a high negative correlation coefficient moduli with the As/R ratio. Thus, the migration of oil acidic and the polar components of crude oil (from the bulk to the interface) is the most contributing factor for the viscoelastic property of the interface between the two fluids.

In the displacement of oil by water in initially water-wet porous media, imbibition occurs in two separate regimes. In “regime 1” the oil saturation reduces slightly. As a result, the oil phase stays connected, as shown in Figure 65A (red), which shows the imbibition experiments of a Gildehauser sandstone done by Rucker et al. (2015). Regime 1 is followed by regime 2, at which the oil phase divides into individual fragments (Figure 65B). The onset of the breakup of oil clusters is marked by a sharp increase in the snap-off events (Figure 65D).

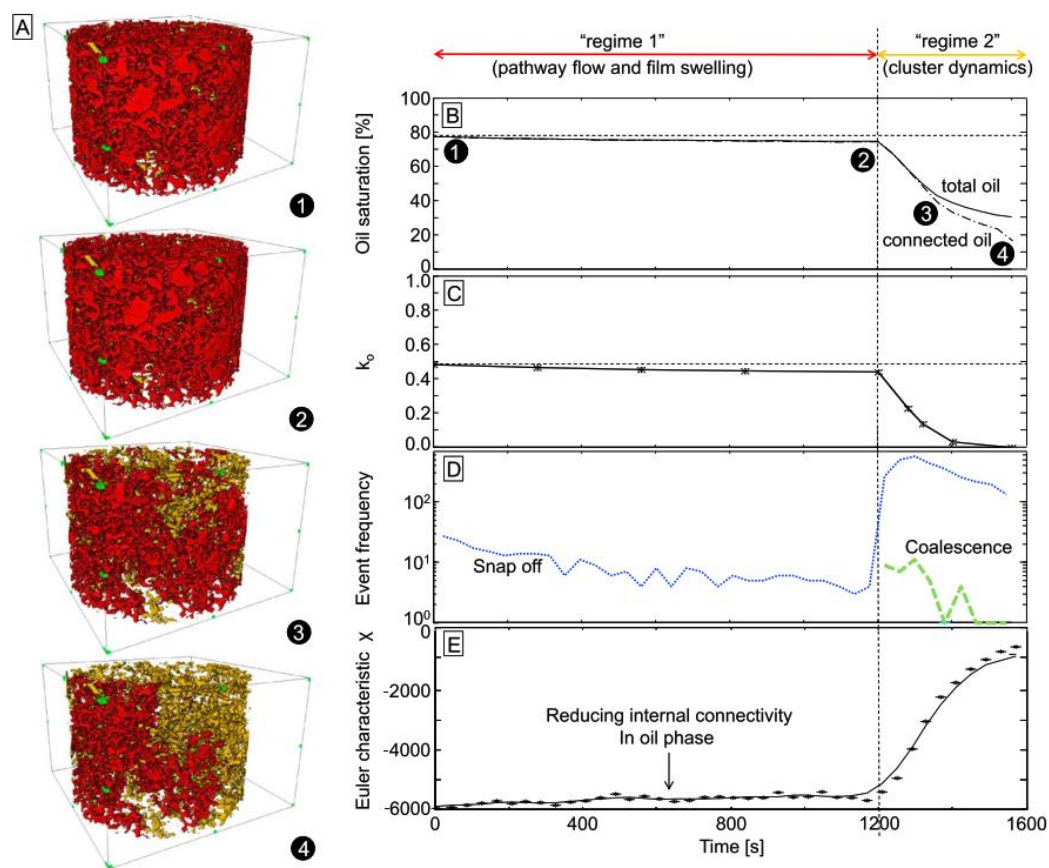


Figure 65 – The imbibition experiment of a Gildehauser sandstone (Rucker, et al., 2015).

In regime 1, one large cluster dominates all oil volume inside porous media. Therefore, it provides connected pathways for the flow of the oil phase. While in regime 1, the oil saturation experiences only minor changes, the phase connectivity decreases. The Euler characteristic is used to identify the phase connectivity and is defined as:

$$\chi = \beta_0 - \beta_1 \quad \text{Eq. 15}$$

where χ is the Euler characteristic, β_0 is the number of objects, i.e., clusters, and β_1 is the number of redundant connections or loops. The increase in the Euler characteristic indicates a decrease in connectivity within the connected oil phase, which finally leads to break up into isolated clusters. In regime 1, by having one dominant connected oil cluster, β_0 is equal to 1 and β_1 decreases. That is caused by movements of “redundant connections” or multiple pores and pore throats through snap-off events (Figure 65D) disconnecting oil in pore throats. As a result, χ increases, as illustrated in Figure 65E. This also causes a slight reduction in the relative permeability of the connected oil phase, as shown in Figure 65C. On the other hand, in regime 2, there is a transition from the connected oil phase flow (Figure 65a, red) to disconnected oil clusters (Figure 65A, yellow) which break off from the initially connected oil phase as fragments of increasing size. As a result, the fraction of the connected oil phase decreases, and the number of clusters, i.e., β_0 increases. As it continues, the connectivity decreases, leading to a substantial increase in the Euler characteristic, as depicted in Figure 65E. Consequently, the connected oil phase relative permeability reduces (Figure 65C). In regime 2, two flow regimes exist, i.e., connected pathway flow and the second being the ganglion dynamics. When the connected oil saturation fraction decreases, the associated (connected pathway) relative permeability decreases, and snap-off and coalescence events frequently occur. This indicates that the transport of the oil phase may occur through the flow of connected pathways and mobile clusters. While the overall oil saturation reduces, not only the biggest cluster gets smaller over time, but also the fragments become, in general, smaller. This clearly shows that clusters remain mobile even though if the flow regime is characterized as capillary dominated. Viscous forces need to overcome capillary forces for the mobilization of oil clusters. In general, the capillary number, C_a^{micro} is defined as:

$$C_a^{\text{micro}} = \frac{\mu_w v}{\sigma} \quad \text{Eq. 16}$$

where μ_w is the viscosity of the displacing fluid, i.e., water, v is the average velocity, and σ the interfacial tension. In the capillary-dominated regime, clusters can remain mobile through a coupled sequence of breakup and coalescence events. While breakup through snap-off is a common phenomenon in imbibition, it is much less clear what causes coalescence. Snap-off events can trigger the coalescence of two clusters that are in close proximity. As a result, isolated clusters can become reconnected, and the resulting displacement events larger than

single pores. During imbibition, the occurrence of interfacial jumps can cause high local velocities that extend over multiple pores. After such an event, the redistribution of oil clusters may cause coalescence between clusters separated by one pore throat or within the influence zone of the events. The associated meniscus oscillations in the connected water-oil interface can, in turn, trigger coalescence events. The resulting ganglion dynamics can potentially mobilize oil clusters even though viscous forces from the flow field are insufficient for their mobilization.

Microfluidic water flooding experiments were used crude oil 16th for two flow rates with distilled water. One is a low flooding rate of 1 ft/d and the other equal to 5 ft/d. The lower the rate, the longer the two fluids contact each other before a snap-off of the oil cluster occurs. As a result, the aging time will be longer for the lower flooding rate; hence more viscoelasticity impact fluid distribution inside porous media. Figure 66 shows the water flooding end state of the experiments, and the corresponding recovery factors are shown in Table 6.

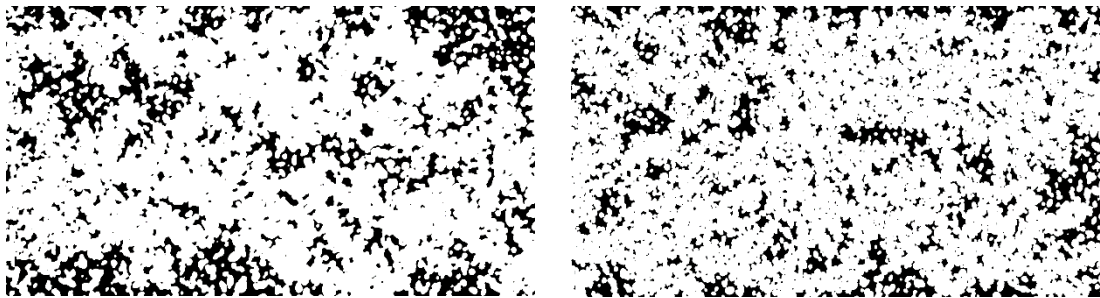


Figure 66 – The end state of the water flooding results: left: high injection rate, right: low injection rate.

Table 6 – The recovery results of the microfluidic experiments.

Crude Name	Recovery factor	
	High rate	Low rate
16 th	58.29%	64.04%

The higher recovery with the lower flooding rate and less applied viscous force can be explained through the effect of interface viscoelasticity.

The displacement regimes can be identified by the interplay of viscous and capillary forces based on mobility ratio and capillary number. The interplay of these two, i.e., viscous and capillary, is shown in Figure 67, a double log scale. The X-axis is the logarithm of mobility number (ratio of the viscosities of the displacing fluid to displaced fluid). Y-axis is the

logarithm of capillary number as defined by Equation 16. The red and blue dots in Figure 67 show the low and high rate experiments, respectively.

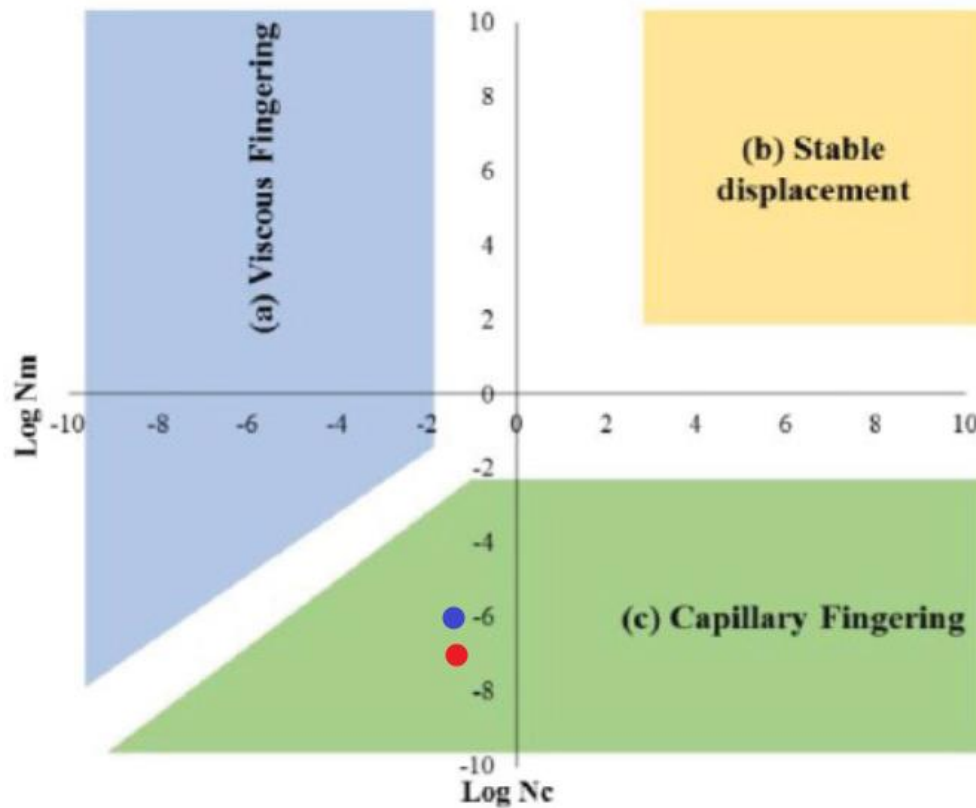


Figure 67 – The location of different displacement regimes. The red and blue dots show the low and high rate experiments, respectively (Alzahid et al., 2017).

As can be seen in Figure 67, changing the injection rate from 5 to 1 ft/d does not change the flow regime, and the difference between recoveries cannot be explained through the regime change.

Based on the results of viscoelasticity measurements, crude 16th had the highest viscoelasticity, both in terms of elastic and viscous modulus. Therefore, we expect that the effect of crude oil/water (or, in general, brine) brine interfaces viscoelasticity to be more evident at a high and low rate and, more importantly, the aging time. Figure 68 shows the cluster size distribution for the two mentioned water flooding experiments with distilled water at high and low rates.

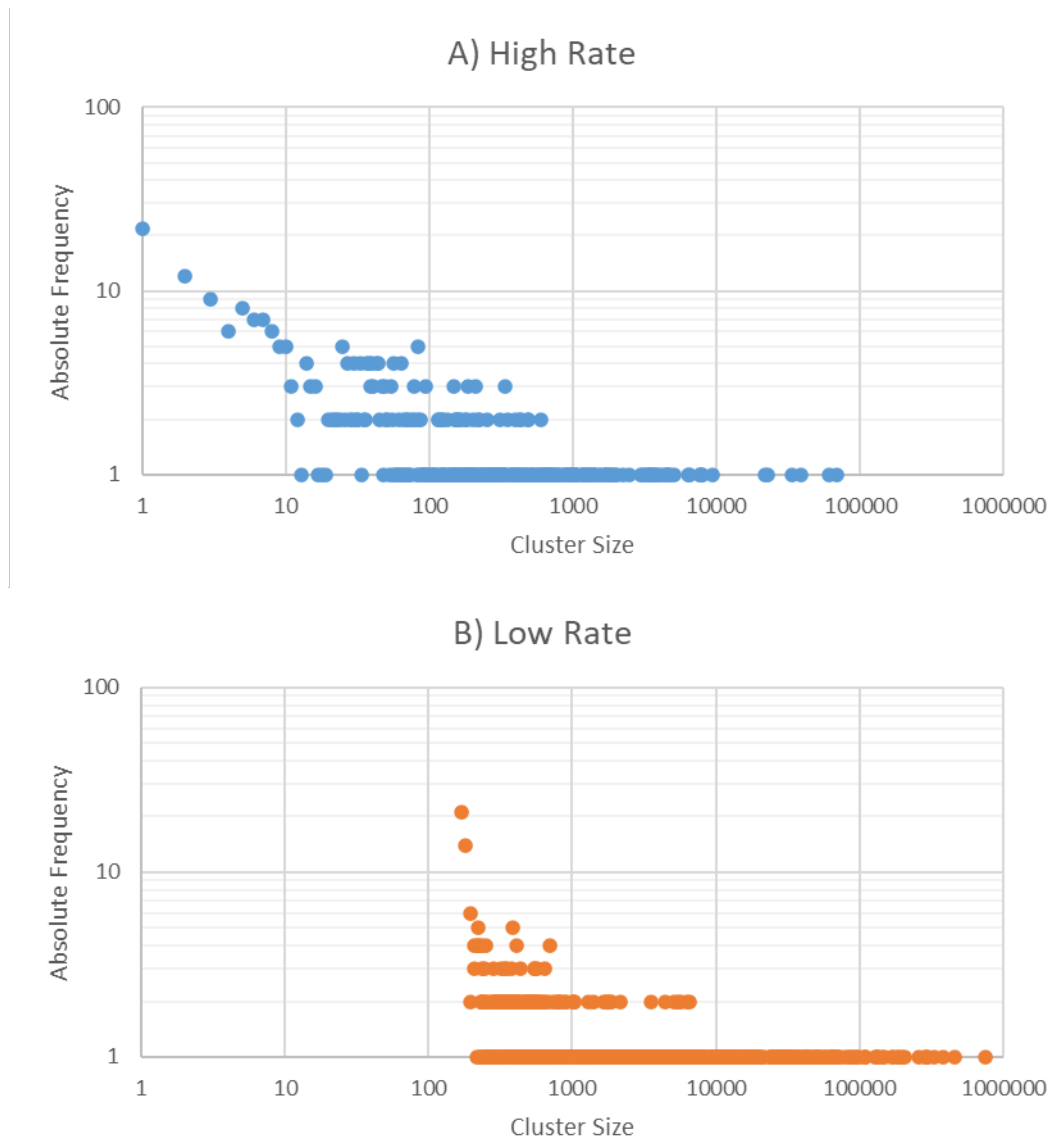


Figure 68 – Cluster size distribution for crude oil. A): high and B): low flooding rates.

The clusters are larger in the low rate experiment than the high rate experiments. This is because despite lowering the flow rate, i.e., less applied viscous force, the interface has more elasticity due to the more aging time of oil and water than the high flooding rate. This leads to larger oil clusters (100 times larger than high rate) at the end of the experiment and higher hydraulic conductivity of the oil phase. As a result, the recovery was higher in the low rate experiment than the one with a five times higher injection rate.

5.2 Microdispersion Ratio Modeling

Based on the methodology described in section 4.1.1, logistic regression is implemented to characterize the important crude oil and brine components for the formation of water in oil microdispersions. Equation 17 shows the final logistic model as the outcome of the statistical analysis with the exploitation of the machine learning algorithm to determine the crucial crude oil and brine properties. The resulting model for predicting the microdispersion ratio depends on two parameters, namely, TAN and brine salinity.

$$p(MDR) = \frac{e^{(a+b*Salinity+c*TAN)}}{1+e^{(a+b*Salinity+c*TAN)}} \quad \text{Eq. 17}$$

where the coefficients a, b, and c are shown in Table 7.

Table 7 – The coefficients of Equation 17.

a	b	c
-0.0311	-0.00046	3.02191

Among the different crude oil properties, the acidic components are significant for microdispersion formation. In addition, with the decrease in total salinity of brine, generally, more microdispersion could potentially form.

Based on the logistic modeling approach, the crude oil acidic components, with a positive coefficient, are the most important factor for the microdispersions to form significantly. On the other hand, with a negative coefficient, the brine salinity negatively correlates with the microdispersion ratio.

As a result, reducing brine salinity can potentially lead to an increase in microdispersion formation. Based on the logistic model results, as shown in Figure 69, 39 data sets with the microdispersion ratio of class 0 (less than 4) and 20 data of class 1 (greater than 4) among the gathered microdispersion ratio were obtained. The derived logistic model could predict 31 out of 39 class 0 correctly and 17 out of 20 which belong to class 1. Tables 8 and 9 show the data that the model failed to predict correctly.

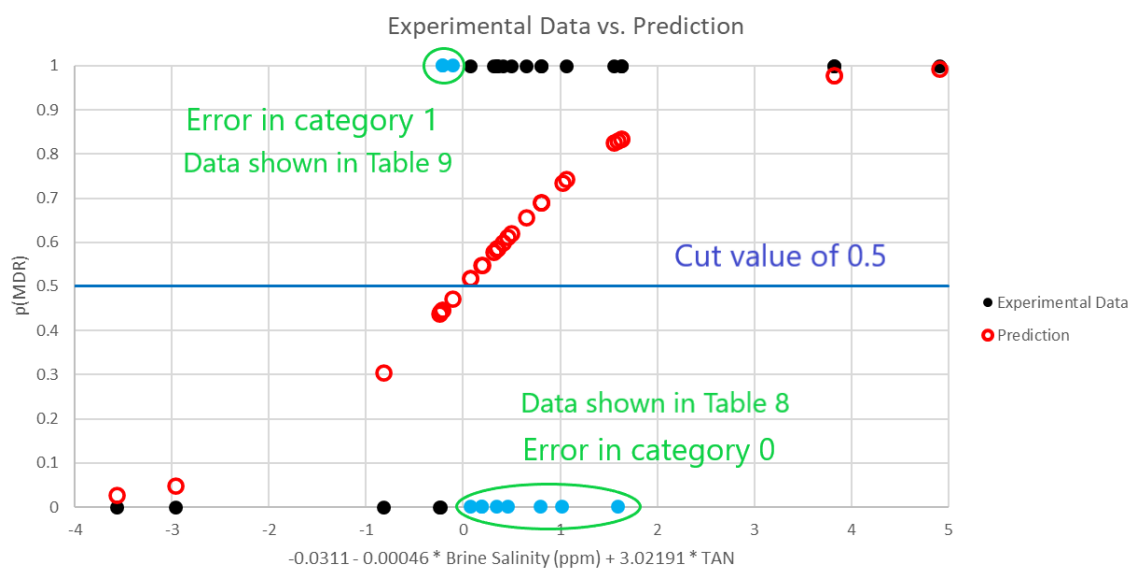


Figure 69 – The results of the prediction model Vs. Experimental data.

Table 8 – Data mismatch for low microdispersion ratio range (less than 4).

Crude Name	Saturate	Aromatic	Resin	Asphaltene	TAN	Brine Salinity (ppm)	MDR	MDR Class (Experimental)	MDR Class (Prediction)
A	63.66	24.9	11.29	0.15	0.15	500	2.10	0	1
F3	53.37	39.76	6.87	0.001	0.35	1238	2.00	0	1
M3	61.55	31.12	7.29	0.04	0.5	1000	1.80	0	1
M2t	67.28	26.59	5.61	0.52	0.69	1000	1.00	0	1
SF	76.06	21.13	2.49	0.32	0.11	493.53	1.86	0	1
DP	42.11	30.01	9.5	18.38	0.2	493.53	2.02	0	1
B	43.8	25.86	29.94	0.4	0.35	493.53	1.21	0	1
A	57.42	30.33	11.75	0.5	0.15	493.53	1.83	0	1

Table 9 – Data mismatch for high microdispersion ratio range (greater than 4).

Crude Name	Saturate	Aromatic	Resin	Asphaltene	TAN	Brine Salinity (ppm)	MDR	MDR Class (Experimental)	MDR Class (Prediction)
S	44.6	43.32	10.08	2	0.05	500	7.80	1	0
M2	62.45	31.21	5.49	0.85	0.7	5000	9.50	1	0
M2	62.45	31.21	5.49	0.85	0.7	5000	18.00	1	0

As can be seen from Table 8, all data mismatches for the low microdispersion ratio range (less than 4) have low salinity levels (less than 1500 ppm). The reason is that the model for data sets with a modest TAN value predicts MDR probability will be higher than 0.5 with salinity levels of less than around 2000 ppm. Thus, there should be a threshold for MDR, which can be the topic of research in the future. With the implementation of such threshold values, the data

mismatch for low salinity levels can be improved. Regarding the data mismatch for high microdispersion rate range, i.e., greater than 4, the system mispredicts low microdispersion ratio, if either when the crude oil has a very low TAN value (0.05) even with extremely low total salinity for brine, or the salinity is reasonably high (5000 ppm) despite having a high amount of crude oil acidic components.

Based on the results of microdispersion and viscoelasticity measurements, the hypothesis that the more viscoelastic the crude oil/brine interface is, the more water in oil microdispersion can form might be considered. The TAN value is the most contributing factor in microdispersion formation as a result of modeling. It might be crucial in the viscoelastic property of crude oil if crude oil viscosity is low enough to allow the migration of interracially active compounds. Both microdispersion modeling and viscoelasticity measurements show a general increasing trend with the reduction of total brine salinity. The remaining mismatch of the predictions and the experimentally measured microdispersion ratios could be justified by including the viscosity of crude in the developed correlation. This requires the viscosity of oil samples to be measured before experiments. Nevertheless, there might be a connection between the fluid/fluid mechanisms investigated in this work, i.e., microdispersion formation and crude oil/brine interface viscoelasticity, which is worth further investigating.

Elasticity has been suggested to hinder the snap-off of the oil clusters into small droplets, leading to a more continuous phase that can be swept more easily. At the fluid/fluid interface, Smart low salinity water has been reported in some cases to reduce the interfacial tension between two phases. However, they may also decrease or increase the viscoelastic property of the oil and brine interface. In other words, changing the thermodynamic property (interfacial tension) alone does not describe improved oil recovery from Smart low salinity injection; the rheological property (viscoelasticity) of the fluid/fluid interface might contribute to improved oil recovery also. Therefore, the snap-off phenomena and their relation to microdispersion and elasticity need to be further investigated.

Chapter 6

Conclusion

6.1 Summary

In this work, the viscoelastic property of crude oil was investigated by the spinning drop technique. Experiments were carried out at an ambient temperature of 22 °C.

Crude oil 16th showed the highest viscoelastic properties in all mechanical moduli among the studied crude oil, whereas crude 8th showed the least viscoelasticity. Thus, the crude oil acidic components are the most important factor among all crude oil properties. Both the normal crude oil 16th and the de-asphalted one reflected more or less the same behavior, highlighting little influence of asphaltene molecules on the viscoelasticity for the crude oils used.

The other important factor detected to be the crude oil viscosity. This indicates that the interface viscoelasticity is a diffusion-like process. A positive correlation was observed for the viscoelastic moduli of the crude oil and distilled water and the ratio of the TAN over viscosity. So, crude oil must have a reasonably high TAN value as well as low viscosity for the migration of the acidic components from the bulk phase to the interface.

The sensitivity of the viscoelasticity and the brine salinity was also investigated. The mechanical moduli increase by lowering brine total salinity. Generally, crude oil with high TAN and low viscosity has high viscoelasticity. In addition, the mechanical moduli can change non-monotonically by introducing sulfate ions to the solution. Both crude oil 16th and Flysch with 2.5 %Na₂SO₄ resulted in maximum elastic moduli at 10,000 ppm total NaCl salinity.

Based on the microfluidic waterflooding displacement results for crude oil 16th and distilled water, 1 ft/d resulted in around 6 % higher recovery than the 5 ft/d rates. More importantly, the clusters were substantially more significant for the low rate than the high rate flooding. This shows the importance of interface viscoelasticity on the fluid redistribution inside porous media. The more elastic modulus, the higher the coalescence rate will be, and as a result, the

bigger the clusters and hydraulic conductivity. The results of the viscoelasticity measurements could justify the recovery increase by lowering the water flooding injection rate. Due to the diffusion-like nature of viscoelasticity, the longer the aging time, i.e., the more contact time of the two immiscible phases, the more the interface can build up its viscoelasticity.

The analytical investigation of the microdispersion data revealed the importance of crude oil acidic components as the main contributing factor in the formation of water in oil microdispersions. Furthermore, the total brine salinity was determined as the main factor regarding the brine properties with a negative correlation factor. Thus, the microdispersion ratio modeling results agreed with the core flooding results reported in the literature. The oil acidic components were detected as the main crude oil fractions contributing to the microdispersion formation.

6.2 Future Work

Further study of the impact of interface viscoelasticity by changing brine salinity as well as its ionic concentrations on the fluid distribution and remaining oil saturation inside porous media.

Investigating the crude oils-brine ability to form microdispersions and its relation to snap off to shed light on the possible connection between interface viscoelasticity and the microdispersion theory.

Chapter 7

References

- AlHammadi, M., Mahzari, P., & Sohrabi, M. (2018). Fundamental investigation of underlying mechanisms behind improved oil recovery by low salinity water injection in carbonate rocks. *Fuels*, 345-357.
- Alvarado, V., Bidhendi, M., Garcia-Olvera, G., Morin, B., & Oakey, J. (2014). Interfacial Visco-Elasticity of Crude Oil - Brine: An Alternative EOR Mechanism in Smart Waterflooding. SPE Improved Oil Recovery Symposium. Tulsa, Oklahoma, USA: Society of Petroleum Engineers.
- Alvarado, V., Moradi, M., Garcia-Olvera, G., Morin, B., & Oakey, J. (2014). Interfacial Visco-Elasticity of Crude Oil - Brine: An Alternative EOR Mechanism in Smart Waterflooding. SPE Improved Oil Recovery Symposium. Tulsa, Oklahoma, USA: Society of Petroleum Engineers.
- Alzahid, Y., Mostaghimi, P., Ebrahimi, M., & Armstrong, R. (2017). Alkaline Surfactant Polymer Flooding: What Happens at the Pore Scale? 79th EAGE Conference and Exhibition. Paris, France: Society of Petroleum Engineers.
- Arnold, P. (2018). Experimental Investigation of Interfacial Tension for Alkaline Flooding. Montanuniversität, Leoben.
- Aske, N., Orr, R., & Sjöblom, J. (2002). Dilatational Elasticity Moduli of Water–Crude Oil Interfaces Using the Oscillating Pendant Drop. *Journal of Dispersion Science and Technology*, 809-825.
- Austad, T., RezaiDoust, A., & Puntervold, T. (2010). Chemical Mechanism of Low Salinity Water Flooding in Sandstone Reservoirs. SPE Improved Oil Recovery Symposium. Oklahoma, USA: Society of Petroleum Engineers.

- Austad, T., Shariatpanahi, S., Strand, S., Black, C., & Webb, K. (2011). Conditions for a Low-Salinity Enhanced Oil Recovery (EOR) Effect in Carbonate Oil Reservoirs. *Energy & Fuels*, 569–575.
- Austad, T., Shariatpanahi, S., Strand, S., Black, C., & Webb, K. (2012). Conditions for a Low-Salinity Enhanced Oil Recovery (EOR) Effect in Carbonate Oil Reservoirs. *Energy & Fuels*, 569–575.
- Barati, R., Tetteh, J., & Rankey, E. (2017). Low Salinity Waterflooding Effect: Crude Oil/Brine Interactions as a Recovery Mechanism in Carbonate Rocks. OTC. Rio de Janeiro, Brazil: Society of Petroleum Engineers.
- Bartels, W., Mahani, H., Berg, S., Menezes, S., van der Hoeven, J., & Fadili, A. (2016). Low Salinity Flooding (LSF) in Sandstones at Pore Scale: Micro-Model Development and Investigation. SPE Annual Technical Conference and Exhibition. Dubai, UAE: Society of Petroleum Engineers.
- Bartels, W., Rücker, M., Berg, S., Mahani, H., Georgiadis, A., Brussee, N., . . . Hassanizadeh, S. (2017). Micro-CT study of the Impact of Low Salinity Waterflooding on the pore-scale fluid distribution during flow. International Symposium of the Society of Core Analysts. Snow Mass, Colorado, USA.
- Berg, S., Ott, H., Klapp, S., Schwing, A., Neiteler, R., Brussee, N., . . . Stampanoni, M. (2013). Real-time 3D imaging of Haines jumps in porous media flow. *Proceedings of the National Academy of Sciences of the United States of America*, 3755-3759.
- Chávez-Miyauchi, T., Firoozabadi, A., & Fuller, G. (2016). Nonmonotonic Elasticity of the Crude Oil–Brine Interface in Relation to Improved Oil Recovery. *Langmuir*, 2192–2198.
- Cissokho, M., Bertin, H., Boussour, S., Cordiner, P., & Hamon, G. (2010). Low Salinity Oil Recovery On Clayey Sandstone: Experimental Study. *Petrophysics*, 05.
- Emadi, A., & Sohrabi, M. (2013). Visual Investigation of Oil Recovery by Low Salinity Water Injection: Formation of Water Micro-Dispersions and Wettability Alteration. SPE Annual Technical Conference and Exhibition. New Orleans, Louisiana, USA: Society of Petroleum Engineers.
- Facanha, J., Mahzari, P., & Sohrabi, M. (2017). Direct Observation of Low-Salinity Water Effect: Relationship Between Micro-Dispersion Formation and Wettability Alteration. SPE Middle East Oil & Gas Show and Conference. Manama, Kingdom of Bahrain: Society of Petroleum Engineers.

-
- Fainerman, V., Kovalchuk, V., Aksenenko, E., Michel, M., Leser, E., & Miller, R. (2004). Models of Two-Dimensional Solution Assuming the Internal Compressibility of Adsorbed Molecules: A Comparative Analysis. *The Journal of Physical Chemistry B*, 13700–13705.
- Fainerman, V., Miller, R., & Kovalchuk, V. (2002). Influence of the Compressibility of Adsorbed Layers on the Surface Dilational Elasticity. *Langmuir*, 7748–7752.
- Fan, Y., Simon, S., & Sjöblom, J. (2010). Interfacial shear rheology of asphaltenes at oil-water interface and its relation to emulsion stability: Influence of concentration, solvent aromaticity, and nonionic surfactant. *Colloids and Surfaces A: Physicochemical and Engineering Aspects*, 120-128.
- Fathi, S., Austad, T., & Strand, S. (2010). “Smart Water” as a Wettability Modifier in Chalk: The Effect of Salinity and Ionic Composition. *Energy & Fuels*, 2514–2519.
- Fattahi Mehraban, M., Farzaneh, S., Sohrabi, M., & Sisson, A. (2020). Novel Insights into the Pore-Scale Mechanism of Low Salinity Water Injection and the Improvements on Oil Recovery. *Energy & Fuels*, 12050–12064.
- Fredriksen, S., Rognmo, A., & Ferno, M. (2016). Pore-Scale Mechanisms During Low Salinity Waterflooding: Water Diffusion and Osmosis for Oil Mobilization. *SPE Bergen One Day Seminar*. Bergen, Norway: Society of Petroleum Engineers.
- Freer, E., Wong, H., & Radke, C. (2005). Oscillating drop/bubble tensiometry: effect of viscous forces on the measurement of interfacial tension. *Journal of Colloid and Interface Science*, 128-132.
- Garcia-Olvera, G., & Alvarado, V. (2017). Interfacial rheological insights of sulfate-enriched smart-water at low and high-salinity in carbonates. *Fuel*, 402-412.
- Hassenkam, T., Mitchell, A., Pedersen, C., Skovbjerg, L., Bovet, N., & Stipp, S. (2012). The low salinity effect observed on sandstone model surfaces. *Colloids and Surfaces A: Physicochemical and Engineering Aspects*, 79-86.
- Hassenkam, T., Pedersen, C., Dalby, K., Austad, T., & Stipp, S. (2011). Pore scale observation of low salinity effects on outcrop and oil reservoir sandstone. *Colloids and Surfaces A: Physicochemical and Engineering Aspects*, 179-188.
- Jackson, M., Vinogradov, J., Hamon, G., & Chamerois, M. (2016). Evidence, mechanisms, and improved understanding of controlled salinity waterflooding part 1: Sandstones. *Fuel*, 772-793.

- Kalogianni, E., Varkaa, E., Karapantsios, T., Kostoglou, M., Santini, E., Liggieri, L., & Ravera, F. (2010). A multi-probe non-intrusive electrical technique for monitoring emulsification of hexane-in-water with the emulsifier C10E5 soluble in both phases. *Colloids and Surfaces A: Physicochemical and Engineering Aspects*, 353-363.
- Kharrat, A. (2018). *Alkali-based Displacement Processes in Microfluidic Experiments: Advanced Statistical Analyses*. Montanuniversität, Leoben.
- Kilpatrick, P. (2012). Water-in-Crude Oil Emulsion Stabilization: Review and Unanswered Questions. *Energy & Fuels*, 4017–4026.
- Kovalchuk, V., Krägel, J., Pandolfini, P., Loglio, G., Liggieri, L., & Ravera, F. (2009). Dilatational rheology of thin liquid films. *MPI of Colloids and Interfaces*, .476-518.
- Kovalchuk, V., Loglio, G., Fainerman, V., & Miller, R. (2004). Interpretation of surface dilational elasticity data based on an intrinsic two-dimensional interfacial compressibility model. *Journal of Colloid and Interface Science*, 475-482.
- Kovalchuk, V., Miller, R., Fainerman, V., & Loglio, G. (2005). Dilational rheology of adsorbed surfactant layers—role of the intrinsic two-dimensional compressibility. *Advances in Colloid and Interface Science*, 303-312.
- Kumar, K., Nikolov, A., & Wasan, D. (2001). Mechanisms of Stabilization of Water-in-Crude Oil Emulsions. *Industrial & Engineering Chemistry Research*, 3009–3014.
- Lager, A., Webb, K. J., Collins, I., & Richmond, D. M. (2008). *LoSal Enhanced Oil Recovery: Evidence of Enhanced Oil Recovery at the Reservoir Scale*. SPE Symposium on Improved Oil Recovery. Oklahoma, USA: Society of Petroleum Engineers.
- Lalchev, Z., Todorov, R., & Exerowa, D. (2008). Thin liquid films as a model to study surfactant layers on the alveolar surface. *Current Opinion in Colloid & Interface Science*, 183-193.
- Lebedeva, E., & Fogden, A. (2011). Micro-CT and Wettability Analysis of Oil Recovery from Sand Packs and the Effect of Waterflood Salinity and Kaolinite. *Energy & Fuels*, 5683–5694.
- Lebedeva, E., Senden, T., Knackstedt, M., & Morrow, N. (2009). Improved Oil Recovery from Tensleep Sandstone – Studies of Brine-Rock Interactions by Micro-CT and AFM. IOR 2009 - 15th European Symposium on Improved Oil Recovery, European Association of Geoscientists & Engineers.

-
- Leser, M., Acquistapace, S., Cagna, A., Makievski, A., & Miller, R. (2005). Limits of oscillation frequencies in drop and bubble shape tensiometry. *Colloids and Surfaces A: Physicochemical and Engineering Aspects*, 25-28.
- Liao, Y., Basaran, O., & Franses, E. (2004). Hydrodynamic effects on the oscillations of supported bubbles: implications for accurate measurements of surface properties. *Colloids and Surfaces A: Physicochemical and Engineering Aspects*, 367-384.
- Ligthelm, D., Gronsveld, J., Hofman, J., Brussee, N., Marcelis, F., & van der Linde, H. (2009). Novel Waterflooding Strategy By Manipulation Of Injection Brine Composition. EUROPEC/EAGE Conference and Exhibition. Amsterdam, The Netherlands: Society of Petroleum Engineers.
- Liu, Y., Kaszuba, J., & Oakey, J. (2019). Microfluidic investigations of crude oil-brine interface elasticity modifications via brine chemistry to enhance oil recovery. *Fuel*, 338-346.
- Lucassen, J., & Van Den Tempel, M. (1972). Dynamic measurements of dilational properties of a liquid interface. *Chemical Engineering Science*, 1283-1291.
- Mahani, H., Keya, A., Berg, S., Batels, W., Nasralla, R., & Rossen, W. (2015). Insights into the Mechanism of Wettability Alteration by Low-Salinity Flooding (LSF) in Carbonates. *Energy & Fuels*, 1352–1367.
- Mahzari, P., & Sohrabi, M. (2014). Crude Oil/Brine Interactions and Spontaneous Formation of Micro-Dispersions in Low Salinity Water Injection. SPE Improved Oil Recovery Symposium. Tulsa, Oklahoma, USA: Society of Petroleum Engineers.
- Mahzari, P., Sohrabi, M., & Facanha, J. (2019). The Decisive Role of Microdispersion Formation in Improved Oil Recovery by Low-Salinity-Water Injection in Sandstone Formations. *SPE Journal*, 2859–2873.
- Mahzari, P., Sohrabi, M., Cooke, A., & Carnegie, A. (2018). Direct pore-scale visualization of interactions between different crude oils and low salinity brine. *Journal of Petroleum Science and Engineering*, 73-84.
- Masalmeh, S., Al-Hammadi, M., Farzaneh, A., & Sohrabi, M. (2019). Low Salinity Water Flooding in Carbonate: Screening, Laboratory Quantification and Field Implementation. International Petroleum Exhibition & Conference. Abu Dhabi, UAE: Society of Petroleum Engineers.
- McGuire, P. L., Chatham, J. R., Paskavan, F. K., Sommer, D. M., & Carini, F. H. (2005). Low Salinity Oil Recovery: An Exciting New EOR Opportunity for Alaska's North Slope. SPE Western Regional Meeting. California, USA: Society of Petroleum Engineers.

- Moradi, M., & Alvarado, V. (2016). Influence of Aqueous-Phase Ionic Strength and Composition on the Dynamics of Water–Crude Oil Interfacial Film Formation. *Energy & Fuels*, 9170–9180.
- Moran, K., & Czarnecki, J. (2007). Competitive adsorption of sodium naphthenates and naturally occurring species at water-in-crude oil emulsion droplet surfaces. *Colloids and Surfaces A: Physicochemical and Engineering Aspects*, 87-98.
- Moran, K., Yeung, A., & Masliyah, J. (2006). The viscoplastic properties of crude oil-water interfaces. *Chemical Engineering Science*, 6016-6028.
- Morin, B., Yafei, L., & Alvarado, V. (2016). A microfluidic flow focusing platform to screen the evolution of crude oil-brine interfacial elasticity. *Lab on a Chip*, 3074-3081.
- Morrow, N., & Buckley, J. (2011). Improved Oil Recovery by Low-Salinity Waterflooding. *Journal of Petroleum Technology*, 106-112.
- Nasralla, R. A., Bataweel, M. A., & Nasr-El-Din, H. A. (2011). Investigation of Wettability Alteration by Low Salinity Water in Sandstone Rock. SPE Offshore Europe Oil and Gas Conference and Exhibition. Aberdeen, UK: Society of Petroleum Engineers.
- Pu, H., Xie, X., Yin, P., & Morrow, N. (2008). Application of Coalbed Methane Water to Oil Recovery from Tensleep Sandstone by Low Salinity Waterflooding. SPE Symposium on Improved Oil Recovery. Oklahoma, USA: Society of Petroleum Engineers.
- Pu, H., Xie, X., Yin, P., & Morrow, N. (2010). Low Salinity Waterflooding and Mineral Dissolution. SPE Annual Technical Conference and Exhibition. Florence, Italy: Society of Petroleum Engineers.
- Quintero, C., Noik, C., Dalmazzone, C., & Grossiord, J. (2009). Formation Kinetics and Viscoelastic Properties of Water/Crude Oil Interfacial Films. *Oil & Gas Science and Technology*, 607 - 616.
- Radke, M., Willsch, H., & Welte, D. (1980). Preparative hydrocarbon group type determination by automated medium pressure liquid chromatography. *Analytical Chemistry*, 406–411.
- Ravera, F., Loglio, G., & Kovalchuk, V. (2010). Interfacial dilational rheology by oscillating bubble/drop methods. *Current Opinion in Colloid & Interface Science*, 217-228.
- Ravera, F., Loglio, G., Pandolfini, P., Santini, E., & Liggieri, L. (2010). Determination of the dilational viscoelasticity by the oscillating drop/bubble method in a capillary pressure tensiometer. *Colloids and Surfaces A: Physicochemical and Engineering Aspects*, 2-13.

-
- Rosenfeld, L., & Fuller, G. (2012). Consequences of Interfacial Viscoelasticity on Thin Film Stability. *Langmuir*, 14238–14244.
- Rücker, M., Berg, S., Armstrong, R., Georgiadis, A., Ott, H., Schwing, A., . . . Kersten, M. (2015). From connected pathway flow to ganglion dynamics. *Geophysical Research Letters*, 3888-3894.
- Santini, E., Liggieri, L., Sacca, L., Clause, D., & Ravera, F. (2007). Interfacial rheology of Span 80 adsorbed layers at paraffin oil-water interface and correlation with the corresponding emulsion properties. *Colloids and Surfaces A: Physicochemical and Engineering Aspects*, 270-279.
- Santini, E., Ravera, F., Ferrari, M., Stubenrauch, C., Makievski, A., & Krägel, J. (2007). A surface rheological study of non-ionic surfactants at the water–air interface and the stability of the corresponding thin foam films. *Colloids and Surfaces A: Physicochemical and Engineering Aspects*, 12-21.
- Sanyal, S., Bhui, U. K., Kumar, S., & Balaga, D. (2017). Designing Injection Water for Enhancing Oil Recovery from Kaolinite Laden Hydrocarbon Reservoirs: A Spectroscopic Approach for Understanding Molecular Level Interaction during Saline Water Flooding. *Energy & Fuels*, 11627–11639.
- Sanyal, S., Bhui, U., Balaga, D., & Kumar, S. (2019). Interaction study of montmorillonite-crude oil-brine: Molecular-level implications on enhanced oil recovery during low saline water flooding from hydrocarbon reservoirs. *Fuel*, 115725.
- Schnöpf, B. (2019). *Statistical Analysis of the Microscopic Fluid Phase Distribution in Microfluidics for EOR Screening*. Montanuniversität, Leoben.
- Sheu, E., De Tar, M., Storm, D., & De Canio, S. (1992). Aggregation and kinetics of asphaltenes in organic solvents. *Fuel*, 299-302.
- Sohrabi, M., Mahzari, P., Farzaneh, S., Mills, J., Tsolis, P., & Ireland, S. (2017). Novel Insights Into Mechanisms of Oil Recovery by Use of Low-Salinity-Water Injection. *SPE Journal*, 407–416.
- Song, J., Rezaee, S., Guo, W., Hernandez, B., Puerto, M., Vargas, F., . . . Biswal, S. (2020). Evaluating physicochemical properties of crude oil as indicators of low-salinity–induced wettability alteration in carbonate minerals. *Scientific Reports*.
- Spiecker, P., & Kilpatrick, P. (2004). Interfacial Rheology of Petroleum Asphaltenes at the Oil–Water Interface. *Langmuir*, 4022–4032.

- Strand, S., Hognesen, E., & Austad, T. (2006). Wettability alteration of carbonates—Effects of potential determining ions (Ca^{2+} and SO_4^{2-}) and temperature. *Colloids and Surfaces A: Physicochemical and Engineering Aspects*, 1-10.
- Sulaimon, A., De Castro, J., & Vatsa, S. (2020). New correlations and deposition envelopes for predicting asphaltene stability in crude oils. *Journal of Petroleum Science and Engineering*.
- Varadaraj, R., & Brons, C. (2007). Molecular Origins of Crude Oil Interfacial Activity Part 3: Characterization of the Complex Fluid Rag Layer Formed at Crude Oil–Water Interfaces. *Energy & Fuels*, 1617–1621.
- Varadaraj, R., & Brons, C. (2012). Molecular Origins of Crude Oil Interfacial Activity. Part 4: Oil–Water Interface Elasticity and Crude Oil Asphaltene Films. *Energy & Fuels*, 7164–7169.
- Yang, X., Verruto, V., & Kilpatrick, P. (2007). Dynamic Asphaltene–Resin Exchange at the Oil/Water Interface: Time-Dependent W/O Emulsion Stability for Asphaltene/Resin Model Oils. *Energy & Fuels*, 1343–1349.
- Yousef, A., Al-Saleh, S., Al-Kaabi, A., & Al-Jawfi, M. (2010). Laboratory Investigation of Novel Oil Recovery Method for Carbonate Reservoirs. *Canadian Unconventional Resources and International Petroleum Conference*. Calgary, Alberta, Canada: Society of Petroleum Engineers.
- Zahid, A., Shapiro, A., & Halfdan, E. (2012). Managing injected water composition to improve oil recovery: A case study of North Sea chalk reservoirs. *Energy & Fuels*, 3407 - 3415.
- Zahid, A., Shapiro, A., & Skauge, A. (2012). Experimental Studies of Low Salinity Water Flooding in Carbonate Reservoirs: A New Promising Approach. *SPE EOR Conference at Oil and Gas West Asia*. Muscat, Oman: Society of Petroleum Engineers.
- Zhang, P., Tveheyo, M., & Austad, T. (2007). Wettability alteration and improved oil recovery by spontaneous imbibition of seawater into chalk: Impact of the potential determining ions Ca^{2+} , Mg^{2+} , and SO_4^{2-} . *Colloids and Surfaces A: Physicochemical and Engineering Aspects*, 199-208.

Appendix A

Microdispersion ratio data from the literature

Table 10 shows all the available microdispersion ratio data from the measurement procedure reported by Fattahi et al. 2020 and the corresponding crude oil and brine properties.

Table 10 – Microdispersion ratio data from the literature

MDR	Brine Salinity (ppm)	Temperature (K)	TBN	TAN	Asphaltene	Resin	Aromatic	Saturate	Crude Name	Paper	Number
2.1	500	333.15	0.9	0.15	0.15	11.29	24.9	63.66	A	Mahzari et al., 2019	1
9.5	500	333.15	3.4	1.35	1.71	31.75	42.01	24.53	W	Mahzari et al., 2019	2
48.6	500	333.15	1.3	1.71	0.2	7.6	29.97	62.23	DTH	Mahzari et al., 2019	3
11	500	333.15	3	0.2	18.71	11.67	30.38	39.24	DP	Mahzari et al., 2019	4
2.1	500	333.15	0.2	0.01	0.05	1.4	19.48	79.07	K	Mahzari et al., 2019	5
7.8	500	333.15	1.1	0.05	2	10.08	43.32	44.6	S	Mahzari et al., 2019	6
29.5	500	333.15	1.1	0.25	0.05	34.1	24.9	40.95	SL	Mahzari et al., 2019	7
1	28000	333.15	2.1	0.55	0.82	16.85	33.19	49.14	F2	Mahzari et al., 2018	8
1	19671	333.15	2.1	0.55	0.82	16.85	33.19	49.14	F2	Mahzari et al., 2018	9

MDR	Brine Salinity (ppm)	Temperature (K)	TBN	TAN	Asphaltene	Resin	Aromatic	Saturate	Crude Name	Paper	Number
3	10000	333.15	2.1	0.55	0.82	16.85	33.19	49.14	F2	Mahzari et al., 2018	10
13	1238	333.15	2.1	0.55	0.82	16.85	33.19	49.14	F2	Mahzari et al., 2018	11
1	28000	333.15	1.9	0.35	0	6.87	39.76	53.37	F3	Mahzari et al., 2018	12
1	19671	333.15	1.9	0.35	0	6.87	39.76	53.37	F3	Mahzari et al., 2018	13
1	10000	333.15	1.9	0.35	0	6.87	39.76	53.37	F3	Mahzari et al., 2018	14
2	1238	333.15	1.9	0.35	0	6.87	39.76	53.37	F3	Mahzari et al., 2018	15
1	208600	293.15	0.05	0.7	0.85	5.49	31.21	62.45	M2	AlHammedi et al., 2018	16
1.5	35000	293.15	0.05	0.7	0.85	5.49	31.21	62.45	M2	AlHammedi et al., 2018	17
9.5	5000	293.15	0.05	0.7	0.85	5.49	31.21	62.45	M2	AlHammedi et al., 2018	18

MDR	Brine Salinity (ppm)	Temperature (K)	TBN	TAN	Asphaltene	Resin	Aromatic	Saturate	Crude Name	Paper	Number
11	1000	293.15	0.05	0.7	0.85	5.49	31.21	62.45	M2	AlHammedi et al., 2018	19
1	208600	333.15	0.05	0.7	0.85	5.49	31.21	62.45	M2	AlHammedi et al., 2018	20
2.5	35000	333.15	0.05	0.7	0.85	5.49	31.21	62.45	M2	AlHammedi et al., 2018	21
18	5000	333.15	0.05	0.7	0.85	5.49	31.21	62.45	M2	AlHammedi et al., 2018	22
20	1000	333.15	0.05	0.7	0.85	5.49	31.21	62.45	M2	AlHammedi et al., 2018	23
1	208600	293.15	0.02	0.5	0.04	7.29	31.12	61.55	M3	AlHammedi et al., 2018	24
2	35000	293.15	0.02	0.5	0.04	7.29	31.12	61.55	M3	AlHammedi et al., 2018	25
2.2	5000	293.15	0.02	0.5	0.04	7.29	31.12	61.55	M3	AlHammedi et al., 2018	26
1.8	1000	293.15	0.02	0.5	0.04	7.29	31.12	61.55	M3	AlHammedi et al., 2018	27

MDR	Brine Salinity (ppm)	Temperature (K)	TBN	TAN	Asphaltene	Resin	Aromatic	Saturate	Crude Name	Paper	Number
1	208600	293.15	0.08	0.69	0.52	5.61	26.59	67.28	M2t	AlHammadi et al., 2018	28
1	35000	293.15	0.08	0.69	0.52	5.61	26.59	67.28	M2t	AlHammadi et al., 2018	29
1	5000	293.15	0.08	0.69	0.52	5.61	26.59	67.28	M2t	AlHammadi et al., 2018	30
1	1000	293.15	0.08	0.69	0.52	5.61	26.59	67.28	M2t	AlHammadi et al., 2018	31
5.9	493.5	293.15	2.98	0.11	0.32	2.49	21.13	76.06	F	Fattahi et al., 2020	32
2	189689	293.15	2.98	0.11	0.32	2.49	21.13	76.06	F	Fattahi et al., 2020	33
77.8	493.5	293.15	0.55	0.3	2.67	16.93	46.76	33.64	U9	Fattahi et al., 2020	34
1	189689	293.15	0.55	0.3	2.67	16.93	46.76	33.64	U9	Fattahi et al., 2020	35
38.8	493.5	293.15	0.11	0.19	1.2	9.87	30.18	58.75	C	Fattahi et al., 2020	36

MDR	Brine Salinity (ppm)	Temperature (K)	TBN	TAN	Asphaltene	Resin	Aromatic	Saturate	Crude Name	Paper	Number
3.7	189689	293.15	0.11	0.19	1.2	9.87	30.18	58.75	C	Fattahi et al., 2020	37
29.6	493.5	293.15	0.68	0.22	1.83	20.45	41	36.72	U1	Fattahi et al., 2020	38
2.6	189689	293.15	0.68	0.22	1.83	20.45	41	36.72	U1	Fattahi et al., 2020	39
49.3	493.5	293.15	0.2	0.2	1.56	10.87	18.63	68.94	U5	Fattahi et al., 2020	40
2.5	189689	293.15	0.2	0.2	1.56	10.87	18.63	68.94	U5	Fattahi et al., 2020	41
6	493.5	293.15	4.9	0.35	0.4	29.94	25.86	43.8	B	Fattahi et al., 2020	42
2.9	189689	293.15	4.9	0.35	0.4	29.94	25.86	43.8	B	Fattahi et al., 2020	43
1.9	493.5	293.15	2.98	0.11	0.32	2.49	21.13	76.06	SF	Fattahi et al., 2021	44
1	189689	293.15	2.98	0.11	0.32	2.49	21.13	76.06	SF	Fattahi et al., 2021	45

MDR	Brine Salinity (ppm)	Temperature (K)	TBN	TAN	Asphaltene	Resin	Aromatic	Saturate	Crude Name	Paper	Number
12.2	493.5	293.15	3.4	1.35	5.8	31.75	37.9	24.53	J	Fattahi et al., 2021	46
1.8	189689	293.15	3.4	1.35	5.8	31.75	37.9	24.53	J	Fattahi et al., 2021	47
4.2	493.5	293.15	3.2	0.6	1.13	14.86	27.66	56.35	G	Fattahi et al., 2021	48
3	189689	293.15	3.2	0.6	1.13	14.86	27.66	56.35	G	Fattahi et al., 2021	49
6	493.5	293.15	0.22	0.2	1.56	10.87	18.63	68.94	L	Fattahi et al., 2021	50
1	189689	293.15	0.22	0.2	1.56	10.87	18.63	68.94	L	Fattahi et al., 2021	51
2	493.5	293.15	3	0.2	18.38	9.5	30.01	42.11	DP	Fattahi et al., 2021	52
1	189689	293.15	3	0.2	18.38	9.5	30.01	42.11	DP	Fattahi et al., 2021	53
6.8	493.5	293.15	1.9	0.35	0.01	6.87	39.76	53.37	F	Fattahi et al., 2021	54

MDR	Brine Salinity (ppm)	Temperature (K)	TBN	TAN	Asphaltene	Resin	Aromatic	Saturate	Crude Name	Paper	Number
2	189689	293.15	1.9	0.35	0.01	6.87	39.76	53.37	F	Fattahi et al., 2021	55
1.2	493.5	293.15	4.9	0.35	0.4	29.94	25.86	43.8	B	Fattahi et al., 2021	56
1.9	189689	293.15	4.9	0.35	0.4	29.94	25.86	43.8	B	Fattahi et al., 2021	57
1.8	493.5	293.15	0.9	0.15	0.5	11.75	30.33	57.42	A	Fattahi et al., 2021	58
1.7	189689	293.15	0.9	0.15	0.5	11.75	30.33	57.42	A	Fattahi et al., 2021	59

Appendix B

The R code, written for the logistic modeling of the microdispersion ratio data.

The R code used for the logistic modeling of the microdispersion ratio data can be found here.

```
library(tidyverse)

library(ggplot2)

library(ROCR)

library(MASS)

library("writexl")

par(mfcol = c(1, 1))

barplot(table(data$Paper), ylab = "Number of Data", xlab = "", ylim = c(0, 20), col = 5)

data %>%

  ggplot(aes(x = factor(Paper), y = MDR)) +

  geom_boxplot(fill = 5) +

  labs(x = "", y = "Microdispersion Ratio")

data %>%

  ggplot(aes(x = factor(Paper), y = MDR)) +

  geom_violin(fill = "#d50022", color = "#ffd709",

    draw_quantiles = c(0.25, 0.5, 0.75),
```

```
size = 1) +  
geom_jitter(width = 0.2, col = "#5DA5DA", height = 0) +  
labs(x = "", y = "Microdispersion Ratio")  
  
data %>%  
  ggplot(aes(x = factor(data$`Temperature (K)`), y = MDR)) +  
  geom_boxplot(fill = c(4, 2)) +  
  labs(x = "Temperature (C)", y = "Microdispersion Ratio") +  
  scale_x_discrete(breaks=c("293.15", "333.15"),  
    labels=c("20 C", "60 C")) +  
  geom_jitter(width = 0.2, col = 5, height = 0)  
  
par(mfcol = c(2, 1))  
hist(data$MDR, breaks = 20, col = 3, xlab = "MDR", main = "",  
  ylab = "Number of Data")  
boxplot(data$MDR, col = 3, horizontal = TRUE, xlab = "MDR")  
  
par(mfcol = c(2, 1))  
hist(data$Asphaltene, breaks = 20, col = 3, xlab = "Asphaltene Content"  
  , main = "", ylab = "Number of Data", xlim = c(0, 20))  
boxplot(data$Asphaltene, col = 3, horizontal = TRUE,  
  xlab = "Asphaltene Content")  
  
par(mfcol = c(2, 1))  
hist(data$Saturate, breaks = 10, col = 3, xlab = "Saturate Content", main = ""  
  , ylab = "Number of Data")  
boxplot(data$Saturate, col = 3, horizontal = TRUE, xlab = "Saturate Content")
```

```
par(mfcol = c(2, 1))  
hist(data$Aromatic, breaks = 10, col = 3, xlab = "Aromatic Content", main = ""  
      , ylab = "Number of Data")  
boxplot(data$Aromatic, col = 3, horizontal = TRUE, xlab = "Aromatic Content")
```

```
par(mfcol = c(2, 1))  
hist(data$Resin, breaks = 10, col = 3, xlab = "Resin Content", main = ""  
      , ylab = "Number of Data")  
boxplot(data$Resin, col = 3, horizontal = TRUE, xlab = "Resin Content")
```

```
par(mfcol = c(2, 1))  
hist(data$TAN, breaks = 20, col = 3, xlab = "TAN range", main = ""  
      , ylab = "Number of Data")  
boxplot(data$TAN, col = 3, horizontal = TRUE, xlab = "TAN range")
```

```
par(mfcol = c(2, 1))  
hist(data$TBN, breaks = 10, col = 3, xlab = "TBN range", main = ""  
      , ylab = "Number of Data")  
boxplot(data$TBN, col = 3, horizontal = TRUE, xlab = "TBN range")
```

```
par(mfcol = c(2, 1))  
hist(data$CII, breaks = 10, col = 3, xlab = "CII range", main = ""  
      , ylab = "Number of Data")  
boxplot(data$CII, col = 3, horizontal = TRUE, xlab = "CII range")
```

```
par(mfcol = c(2, 1))  
hist(data$`A/R`, breaks = 10, col = 3, xlab = "A/R range", main = ""  
      , ylab = "Number of Data")
```

```
boxplot(data$`A/R`, col = 3, horizontal = TRUE, xlab = "A/R range")
```

```
par(mfcol = c(1, 1))
```

```
data %>%
```

```
  ggplot(aes(x = log10(`Salinity (ppm)`), y = MDR)) +
```

```
  geom_point(col = 4) +
```

```
  labs(x = "Log(Salinity in ppm)", y = "Microdispersion Ratio")
```

```
# Logistic Regression -----
```

```
colnames(data)
```

```
data$class <- ifelse(data$MDR > 4, 1, 0)
```

```
table(data$class)
```

```
gm0 <- glm(class ~ 1, data = data[, c(3:12, 14)], family = binomial)
```

```
gm.all <- glm(class ~ ., data = data[, c(3:12, 14)], family = binomial)
```

```
gm.back <- stepAIC(gm0, direction = "backward", trace = FALSE,  
                 scope = list(lower = gm0, upper = gm.all))
```

```
summary(gm.back)
```

```
gm.forward <- stepAIC(gm0, direction = "forward", trace = FALSE,  
                    scope = list(lower = gm0, upper = gm.all))
```

```
summary(gm.forward)
```

```
calc_perf <- function(object){
```

```
  p <- predict(object, type = "response")
```

```
  a <- prediction(p, object$model$class)
```

```
  auc <- performance(a, "auc")@y.values[[1]]
```

```
  perf <- performance(a, "tpr", "fpr")
```

```
  out <- list(performance = perf, auc = auc)
```

```
}
```

```
p.b.g <- calc_perf(gm.back)
p.f.g <- calc_perf(gm.forward)
par(mfcol = c(1,1))
plot(p.f.g$performance, colorize = TRUE, lwd = 3, main = "p.f.g")
text(0.6, 0.4, labels = paste("AUC = ", round(p.f.g$auc, 2)))
BIC(gm.back)
BIC(gm.forward)
AIC(gm.back)
AIC(gm.forward)
summary(gm.back)
summary(gm.forward)
#gm.forward is the best model*****
pf.g.f <- predict(gm.forward, type = "response")
data$pred.f <- pf.g.f
p.05.f <- ifelse(pf.g.f > 0.5, 1, 0)
p.05.f <- factor(p.05.f, levels = c(1, 0))
data$class <- factor(data$class, levels = c(1, 0))
caret::confusionMatrix(p.05.f, data$class)
write_xlsx(data, "D:\\Master Thesis\\Neuer Ordner\\data_Logistic.xlsx")
```